



POLARIMETER BLIND DECONVOLUTION
USING IMAGE DIVERSITY

DISSERTATION

David M. Strong, Major, USAF

AFIT/DS/ENG/07-20

DEPARTMENT OF THE AIR FORCE
AIR UNIVERSITY

AIR FORCE INSTITUTE OF TECHNOLOGY

Wright-Patterson Air Force Base, Ohio

APPROVED FOR PUBLIC RELEASE; DISTRIBUTION UNLIMITED.

The views expressed in this dissertation are those of the author and do not reflect the official policy of the United States Air Force, Department of Defense, or the United States Government.

AFIT/DS/ENG/07-20

POLARIMETER BLIND DECONVOLUTION
USING IMAGE DIVERSITY

DISSERTATION

Presented to the Faculty
Graduate School of Engineering and Management
Air Force Institute of Technology
Air University
Air Education and Training Command
In Partial Fulfillment of the Requirements for the
Degree of Doctor of Philosophy

David M. Strong, B.S.E.E., M.S.C.E.
Major, USAF

September 2007

APPROVED FOR PUBLIC RELEASE; DISTRIBUTION UNLIMITED.

POLARIMETER BLIND DECONVOLUTION
USING IMAGE DIVERSITY

David M. Strong, B.S.E.E., M.S.C.E.
Major, USAF

Approved:

Stephen C. Cain
Stephen C. Cain (Chairman)

31 Aug 2007
Date

Gary B. Lamont
Gary B. Lamont (Member)

31 Aug 2007
Date

Mark E. Oxley
Mark E. Oxley (Member)

31 Aug 2007
Date

Victor L. Gamiz
Victor L. Gamiz (Member)

30 August, 2007
Date

Richard G. Cobb
Richard G. Cobb (Dean's Representative)

31 Aug 2007
Date

Accepted:

M.U. Thomas
M.U. Thomas
Dean, Graduate School of
Engineering and Management

11 Sep 07
Date

Abstract

This research presents an algorithm that improves the ability to view objects using an electro-optical imaging system with at least one polarization sensitive channel in addition to the primary channel.

Following the review of historical methodologies applicable to this research area, the statistical Cramer-R  o lower bound (CRLB) is developed for a two-channel polarimeter. The CRLB is developed using the system's ability to resolve two point sources in the presence of atmospheric turbulence. The bounds show that such a polarimeter has an advantage over previous imaging methods at smaller separations.

A small optical laboratory is set up to generate a set of calibrated images for verification of the simulation results and validation of algorithm development. Defocus is the aberration chosen for algorithm development and testing due to its significant presence when imaging through turbulence and its ease of production in the laboratory. An innovative algorithm for detection and estimation of the defocus aberration present in an image is also developed.

Using a known defocus aberration, an iterative polarimeter deconvolution algorithm is developed using a generalized expectation-maximization (GEM) model that produces results as predicted by the CRLB results. Using an example bar target set with a degree of polarization of one, the polarimeter deconvolution algorithm can resolve the two bars down to half the bar separation as the Richardson-Lucy (RL) algorithm can do. In addition, a fidelity metric is used that shows the polarimeter deconvolution algorithm deconvolves simulated targets with approximately half of the error present in objects deconvolved using the RL algorithm.

The polarimeter deconvolution algorithm is extended to an iterative polarimeter multiframe blind deconvolution (PMFBD) algorithm with an unknown aberration. Using both simulated and laboratory images, the results of the new PMFBD algo-

rithm clearly outperforms an RL-based MFBD algorithm. The convergence rate is significantly faster with better fidelity of reproduction of the targets.

This research successfully developed an algorithm that uses polarization data in conjunction with standard imaging to improve the spatial resolution of deconvolved objects with faster convergence rates. Clearly, leveraging polarization data in electro-optical imaging systems has the potential to significantly improve the ability to resolve objects and, thus, improve Space Situation Awareness.

For my Lord,

“The fear of the Lord is the beginning of wisdom,...”

and my loving and supportive family!

Acknowledgements

I would like to thank Dr Stephen Cain for his guidance and support that were invaluable throughout this research. Thank you also to Ms Laura Ulibarri and Dr Victor Gamiz for research ideas and financial support.

David M. Strong

Table of Contents

| | Page |
|---|------|
| Abstract | iii |
| Acknowledgements | vi |
| List of Figures | x |
| List of Abbreviations | xiii |
| I. Introduction | 1 |
| 1.1 Space Situational Awareness | 1 |
| 1.2 Problem and Definitions | 2 |
| 1.2.1 Geometry of Scenario | 2 |
| 1.2.2 Imaging | 3 |
| 1.2.3 Convolution | 5 |
| 1.2.4 Deconvolution | 6 |
| 1.2.5 Polarimeter Imaging | 7 |
| 1.3 Layout of the Dissertation document | 8 |
| 1.3.1 Polarimeter Spatial Resolution Bounds | 8 |
| 1.3.2 Laboratory and Simulation Data | 8 |
| 1.3.3 Polarimeter Deconvolution Algorithms | 9 |
| 1.3.4 Results | 9 |
| 1.3.5 Conclusions and Recommendations | 9 |
| II. Historical Background | 10 |
| 2.1 Polarimeters | 10 |
| 2.1.1 Material Reflectance Models | 10 |
| 2.2 Blind Deconvolution | 14 |
| 2.2.1 Single Channel | 14 |
| 2.2.2 Wave-front sensing | 24 |
| 2.2.3 Multi-frame | 25 |
| 2.2.4 Multi-channel | 26 |
| 2.3 Acceleration Techniques | 26 |
| 2.3.1 Parallel Implementation | 27 |
| 2.3.2 Genetic Algorithms | 27 |
| 2.4 Cramer-R o Lower Bounds | 28 |

| | Page |
|---|------|
| III. Polarimeter Cramer-R  o Lower Bounds on Spatial Resolution | 30 |
| 3.1 Bound for Unpolarized Primary Channel | 30 |
| 3.1.1 Image model | 30 |
| 3.1.2 Fisher Information Matrix and CRLB | 32 |
| 3.1.3 Derivatives of the Image | 33 |
| 3.1.4 Cramer-R  o Lower Bound | 35 |
| 3.2 Polarimeter Bounds without Atmospheric Distortion | 36 |
| 3.2.1 Image Model | 36 |
| 3.2.2 Polarimeter Fisher Information Matrix and CRLB | 37 |
| 3.2.3 Polarimeter Image Derivatives | 38 |
| 3.2.4 Individual FI Elements for Polarimeter | 38 |
| 3.2.5 FI Matrix and Degree of Polarization | 42 |
| 3.2.6 Cramer-R  o Lower Bound of Polarimeter | 43 |
| 3.2.7 Analysis | 43 |
| 3.2.8 Transmission and Reflection Efficiency | 44 |
| 3.3 Spatial Resolution Bound with Atmospheric Turbulence | 46 |
| 3.3.1 Image Model | 46 |
| 3.3.2 The Point Spread Function | 47 |
| 3.3.3 Log-likelihood Function | 48 |
| 3.3.4 Polarimeter Fisher Information Matrix and CRLB | 48 |
| 3.3.5 Polarimeter Image Derivatives | 51 |
| 3.3.6 Individual FI Elements for Polarimeter | 53 |
| 3.3.7 Partial Derivatives of the psf | 58 |
| 3.3.8 CRLB | 60 |
| 3.3.9 Effect of Atmospheric Turbulence on CRLB | 61 |
| 3.3.10 Normal Imaging System | 62 |
| 3.3.11 Polarimeter Imaging System | 63 |
| 3.3.12 Other System Parameters | 64 |
| IV. Laboratory Data Calibration | 70 |
| 4.1 Focus Aberration | 70 |
| 4.2 Focus Aberration Detection Algorithm | 72 |
| 4.2.1 Generate phase screens | 72 |
| 4.2.2 Input image | 72 |
| 4.2.3 Generate log-likelihood plot | 72 |
| 4.2.4 Estimate focus aberration | 74 |
| 4.2.5 Repeat for remaining images | 76 |
| 4.3 Testing with Laboratory Data | 77 |
| 4.3.1 Target | 77 |

| | Page |
|--|---------|
| 4.3.2 Camera | 77 |
| 4.3.3 Lens | 78 |
| 4.3.4 Images | 79 |
| 4.4 Additional Considerations | 79 |
| 4.4.1 Sampling effects | 79 |
| 4.4.2 Autofocus Algorithm | 83 |
| 4.4.3 Speedup | 83 |
| V. Polarimeter Image Diversity Blind Deconvolution Algorithm Development | 85 |
| 5.1 Historical Basis | 85 |
| 5.2 Algorithm Development | 88 |
| 5.2.1 Single polarimeter channel with known psf | 88 |
| 5.2.2 PMFBD GEM algorithm | 92 |
| VI. Results and Analysis of Polarimeter Algorithms | 96 |
| 6.1 Known psf with simulation data | 96 |
| 6.1.1 Comparison of results with CRLB predictions | 100 |
| 6.1.2 Known psf with laboratory data | 102 |
| 6.2 Polarimeter Multiframe Blind Deconvolution | 105 |
| 6.2.1 Convergence Rates | 109 |
| 6.2.2 Laboratory Results | 109 |
| VII. Conclusions | 112 |
| Bibliography | 115 |

List of Figures

| Figure | Page |
|---|------|
| 1.1. Fields and Relationships. | 3 |
| 1.2. OTF and Image with Cross Sections. | 4 |
| 1.3. OTF and Detector Image with 10 Zernikes. | 5 |
| 1.4. Hubble Space Telescope Images. | 6 |
| 1.5. Image, Object, Fourier Domain Relationships. | 6 |
| 1.6. Deconvolution Process. | 7 |
| 2.1. Basic Polarimeter. | 10 |
| 2.2. Real and Imaginary Components of \tilde{n} | 12 |
| 2.3. Reflectance versus Wavelength. | 13 |
| 2.4. Predicted n_R , n_I , and Reflectance of Silver. | 14 |
| 2.5. Gerchberg-Saxton Algorithm [13]. | 15 |
| 2.6. Input-Output Algorithm [8]. | 18 |
| 2.7. Ayers and Dainty Algorithm [1]. | 20 |
| 3.1. Visualization of Running Simulation. | 44 |
| 3.2. CRLB on estimation of pixel separation versus actual pixel separation. | 45 |
| 3.3. Average bound relative to pixel separation. | 62 |
| 3.4. Average polarimeter bounds relative to pixel separation. | 63 |
| 3.5. Average bound relative to number of Zernike coefficients estimated. | 65 |
| 3.6. Intensity estimates vs. number of coefficients estimated. | 66 |
| 3.7. Average bound vs. point source intensity. | 67 |
| 3.8. Effect of removing lower order aberrations. | 68 |
| 4.1. OTFs for three different focus aberrations. | 71 |
| 4.2. Focus Aberration Detection Algorithm. | 73 |
| 4.3. Log-likelihood plots at various lens positions. | 75 |

| Figure | | Page |
|--------|---|------|
| 4.4. | Focus Aberration Estimates versus Aperture Size, Focus Cov = $26\mu m^2$ | 77 |
| 4.5. | Focus Aberration Estimates versus Aperture Size, Focus Cov = $212\mu m^2$ | 78 |
| 4.6. | Laboratory Components. | 79 |
| 4.7. | Signal-to-noise ratio versus lens position. | 80 |
| 4.8. | Camera images at various positions (distance to CCD.) | 81 |
| 4.9. | Objects using 70 pixel wide aperture. | 82 |
| 4.10. | Objects using 128 pixel wide aperture. | 82 |
| 4.11. | Objects using 70 pixel estimates with 128 pixel wide aperture. | 83 |
| 6.1. | Fidelity metric for diffraction limited images for various digital aperture sizes, using target with bar width of 3 pixels, target irradiance of 1000 photons per pixel, and image size of 128. | 97 |
| 6.2. | Map of fidelity metric for both the RL algorithm, the polarimeter algorithm, and their difference at an SNR of approximately 10. | 98 |
| 6.3. | Map of fidelity metric for both the RL algorithm, the polarimeter algorithm, and their difference at an SNR of approximately 1. | 98 |
| 6.4. | Map of fidelity metric for both algorithms without beamsplitter assumption at an SNR of approximately 1. | 99 |
| 6.5. | Cross-sectional views of deconvolved object with a barwidth of 3 pixels and a target irradiance of 10 photons per pixel. | 100 |
| 6.6. | Cross-sectional views of deconvolved objects at an SNR of 0.71. | 101 |
| 6.7. | Cross-sectional views of deconvolved objects at an SNR of 0.65. | 102 |
| 6.8. | Cross-sectional views of deconvolved objects at an SNR of 6. | 103 |
| 6.9. | Deconvolution - Position 1. | 103 |
| 6.10. | Deconvolution - Position 5. | 104 |
| 6.11. | Deconvolution - Position 7. | 105 |
| 6.12. | Images used for MFBD algorithm testing. | 105 |
| 6.13. | Images used for PMFBD algorithm testing. | 106 |
| 6.14. | MFBD estimated object. | 107 |

| Figure | Page |
|---|------|
| 6.15. MFBD estimated OTFs. | 107 |
| 6.16. PMFBD estimated object. | 108 |
| 6.17. PMFBD estimated OTFs. | 108 |
| 6.18. Algorithm fidelity versus iterations. | 109 |
| 6.19. Laboratory multiframe estimated objects and cross-sections. . . | 110 |
| 6.20. Laboratory multiframe estimated OTFs. | 111 |

List of Abbreviations

| Abbreviation | | Page |
|--------------|---|------|
| SSA | Space Situational Awareness | 1 |
| QDR | Quadrennial Defense Review | 2 |
| <i>psf</i> | Point Spread Function | 3 |
| OTF | Optical Transfer Function | 3 |
| AO | Adaptive Optics | 4 |
| HST | Hubble Space Telescope | 4 |
| AEOS | Advanced Electro-Optical System | 4 |
| AMOS | Air Force Maui Optical and Supercomputing Site | 5 |
| PBS | Polarizing Beam Splitter | 7 |
| CRLB | Cramer-Rào Lower Bound | 8 |
| MAP | Maximum- <i>a-priori</i> | 8 |
| RL | Richardson-Lucy | 16 |
| GS | Gerchberg-Saxton | 17 |
| IO | Input-Output | 18 |
| AD | Ayers and Dainty | 22 |
| EM | Expectation-Maximization | 22 |
| ML | Maximum-Likelihood | 22 |
| EO | Electro-Optical | 24 |
| CCD | Charge-Coupled Device | 25 |
| MFBD | Multiframe Blind Deconvolution | 25 |
| GOES | Geostationary Operational Environmental Satellite | 26 |
| EA | Evolutionary Algorithm | 27 |
| FI | Fisher Information | 30 |
| PMF | Probability Mass Function | 30 |
| FAD | Focus Aberration Detection | 70 |

| Abbreviation | | Page |
|--------------|-----------------------------|------|
| CD | Complete Data | 85 |
| MSE | Mean Square Error | 107 |

POLARIMETER BLIND DECONVOLUTION USING IMAGE DIVERSITY

I. Introduction

As telescopes have grown larger and larger the effect of atmospheric turbulence on the astronomical images has increased. If the distortion introduced by the atmosphere on the incoming light can be determined, it can be removed from the image. This research addresses an approach for improving image resolution through the use of a polarimeter and the diversity in the images it produces. A polarimeter produces multiple simultaneous observations of the target that are related. The difference between the images is due to the polarized light present in the different channels. The polarized light is created through the interaction of light and materials. Additionally these observations are distorted by the same atmospheric turbulence.

The traditional blind deconvolution problem is ill-posed in that both the system response and the input image are to be determined from a single composite observation. Historical deconvolution methods use iterative approaches to arrive at a solution to the problem. The ability to improve the solution is the main motivation for this research

1.1 *Space Situational Awareness*

Any improvement in the ability to resolve objects viewed through atmospheric turbulence improves Space Situational Awareness (SSA). Its importance is represented in the following two quotes. The first is an excerpt from a speech by Lt Gen Klotz, Vice Commander, AFSC in 2006.

In the face of potentially emerging threats, our fundamental U.S. position is straightforward and our new National Space Policy lays it out very well, and I commend it to your reading. Let me try to summarize it in this way: We must ensure access to space, as it is critical to our Nation's

full range of capabilities ... capabilities that transform the battlefield and empower the global economy. Indeed, the United States is committed to the free use and access to space by all nations for peaceful purposes. The reality is, however, we cannot assume all nations will pursue only peaceful purposes ... just the same way we can not assume all nations will respect the domains of land, air or sea. In light of this reality, we must protect our key capabilities. They are a vital National interest and one of our top priorities.

The first critical component of that protection is space situational awareness. Currently, we in Air Force Space Command catalog approximately 14,000 objects in space ... but it's just that: a catalog. While we can detect objects as small as a baseball in low Earth orbit ... or as small as a basketball in geosynchronous orbit, we need more than just the location and general direction of an object. Our aim is to move beyond cataloging to understanding what is "up there." [23]

The second is an excerpt from the June 2006 Air Force Magazine [44]:

...The new Quadrennial Defense Review (QDR), released in February, simply noted that Washington must have "unfettered, reliable, and secure" access to its space assets, assured, for now, by "improving space situational awareness and protection, and through other space control measures." The Air Force is taking its cue from the QDR, focusing most of its nonclassified efforts at space superiority on systems that will broadly enhance its knowledge of what's in orbit, as well as its ability to know if American space systems are under attack. ... "We have to know what's up there," said Gen. T. Michael Moseley, Air Force Chief of Staff. "We have to continually modernize the early warning systems to know what is up there, what has been added, what are the orbital paths, and what are the opportunities to see." This is what the United States must do to avoid "a Pearl Harbor in space," Moseley observed. The emphasis remains on space situational awareness...

The main motivation for this research is in improving that SSA capability.

1.2 Problem and Definitions

1.2.1 *Geometry of Scenario.* The scenario of interest involves the incoherent illumination of satellites by sunlight which is then reflected by the satellite surfaces and viewed by a telescope. The light reflected can be partially polarized. The amount

of polarization is determined by the incident angle of the light and the material that reflects the light as described in more detail in Section 2.1.

1.2.2 Imaging . Imaging systems, such as telescopes, are used to form images of objects. The incoming light from an object is transformed by a lens to form an image of the object.

$$Object \rightarrow Imaging\ System \rightarrow Image$$

The intensity distribution of the object is convolved with the point spread function (*psf*) to form the image. Using Fourier transforms to move from the spatial domain into the spectral domain changes the convolution into a multiplication. The Fourier transform of the psf is the optical transfer function (OTF). These relationships can be seen in Figure 1.1.

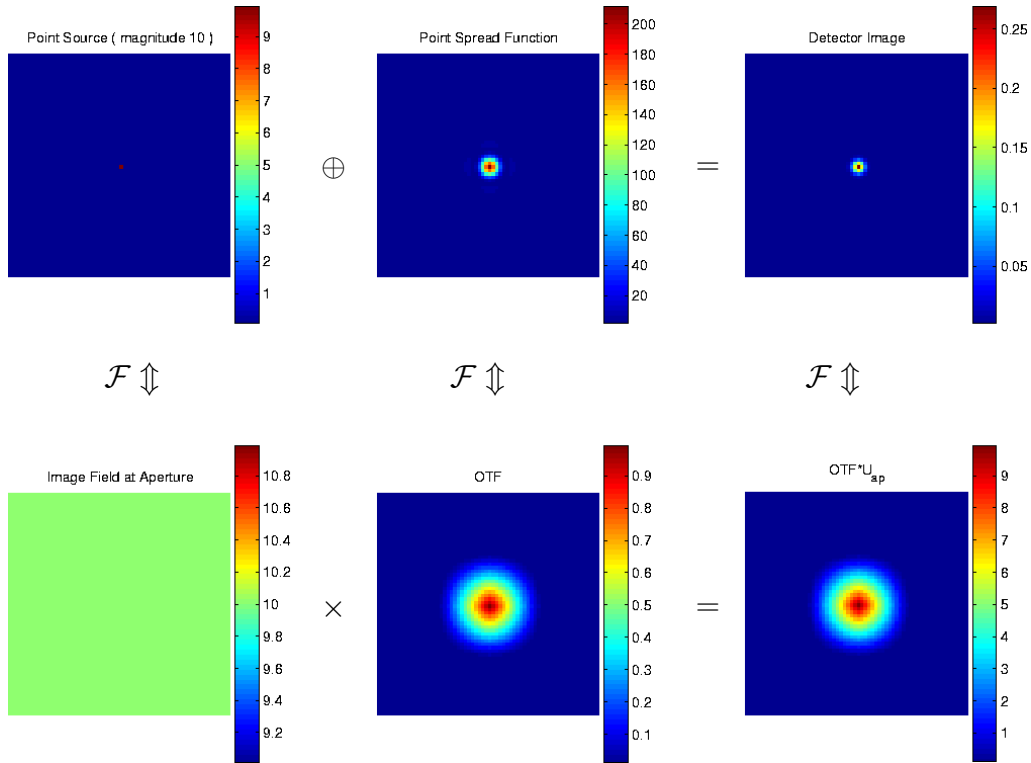


Figure 1.1: Fields and Relationships.

1.2.2.1 Diffraction-limited Image. In a vacuum, the image formed is limited only by diffraction of the light as it passes through an ideal imaging system. Figure 1.2(a) shows the OTF of a circular aperture and Figure 1.2(b) shows the resulting image of a point source.

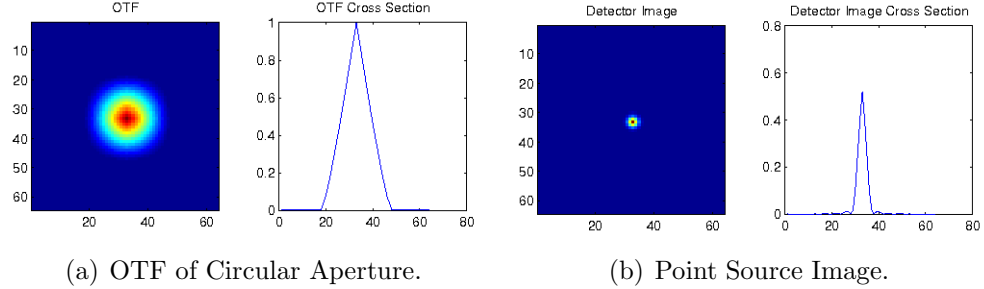


Figure 1.2: OTF and Image with Cross Sections.

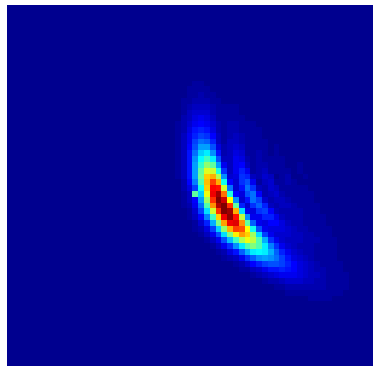
1.2.2.2 Atmospheric Turbulence. Atmospheric turbulence spatially distorts the wavefront as light passes through it and causes blurring of images in an imaging system. Figure 1.3 shows an example of distortion caused by a randomly generated phase screen using 10 Zernike coefficients. The upper left image is the resulting phase screen. The upper right image is the OTF created using the phase screen. The lower set of images are of a point source using the OTF and its cross section.

1.2.2.3 Adaptive Optics. Adaptive optics (AO) systems are used to reduce the effects of atmospheric turbulence. Using deformable mirrors, an AO system can detect and significantly reduce lower order terms of the spatial distortion. Two of the lowest order terms, *tip* and *tilt*, account for approximately 80 percent of the magnitude of the distortion and can be significantly reduced by a movable mirror. The next several terms are typically reduced by a separate deformable mirror. The remaining terms require post-processing to reduce their impact on the image. Figure 1.4 shows an example of the problem. The left image is a computer generated image of the Hubble Space Telescope (HST). The right image is from a 3.7m Advanced Electro-Optical System (AEOS) telescope at the Air Force Maui Optical and Supercomputing

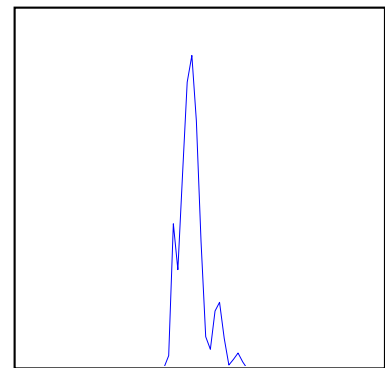


(a) Phase Screen

(b) OTF with phase distortion



(c) Det. Image with Distortion



(d) Det. Image with Dist. Cross-section

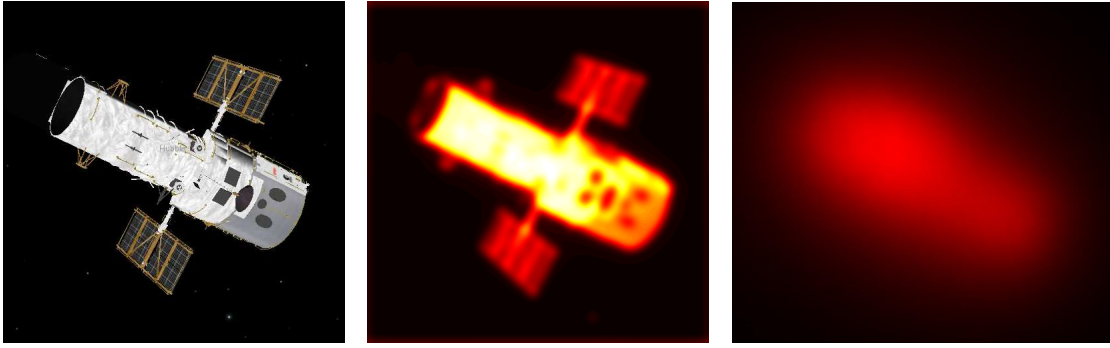
Figure 1.3: OTF and Detector Image with 10 Zernikes.

Site (AMOS) with adaptive optics on and tracking properly. As can clearly be seen, or not as the case may be, there is a significant amount of atmospheric distortion remaining in the image.

1.2.3 Convolution. The relationships between the observed image and the actual object can be defined mathematically. In imaging, the observed image $i(x, y)$ is the two-dimensional convolution of the true image of the object $o(z, w)$ with a linear shift-invariant blur, the psf, $h(x, y)$:

$$i(x, y) = h(x, y) \oplus o(x, y), \quad (1.1)$$

$$= \sum_z \sum_w h(x - z, y - w) o(z, w), \quad (1.2)$$



(a) Computer Model of the Hubble Space Telescope. (b) Example Diffraction Limited Image. (c) Real Image of the Hubble Space Telescope from 3.7m AEOS Telescope.

Figure 1.4: Hubble Space Telescope Images.

where \oplus is the two-dimensional convolution operator.

The transfer function between the Fourier transform of the object viewed and the Fourier transform of the image captured by an imaging system is the OTF [15]. The relationships between the object, its image, and the Fourier domain are shown in Figure 1.5. Using these relationships, it can be seen that the image is the inverse Fourier transform of the Fourier transform of the object multiplied by the OTF.

$$\begin{array}{ccc} I_{object} & \oplus & PSF \\ \downarrow \mathcal{F} & & \downarrow \mathcal{F} \\ S_{object} & \times & OTF \end{array} = \begin{array}{c} I_{image} \\ \uparrow \mathcal{F}^{-1} \\ S_{image} \end{array}$$

Figure 1.5: Image, Object, Fourier Domain Relationships.

I_{object} and I_{image} are the intensity distributions of the object and image, respectively. S_{object} and S_{image} are their corresponding Fourier transforms in the spectral domain.

1.2.4 Deconvolution. Deconvolution is removing the distortion from the image by dividing the Fourier transform of the image by the Fourier transform of the distortion which is the optical transfer function. This ideal process is shown in Figure 1.6. If the OTF is known and there is no noise then the deconvolution is nearly perfect. Only the error from the Fourier transforms attributable to finite machine

precision remains. The problem is that in many cases the OTF that created an image can never be known but only estimated from the intensity data. The reason that iterative approaches are desireable is the presence of zeros in the OTF make division by a real OTF impossible.

$$\begin{array}{ccc} I_{image} & & I_{object} \\ \downarrow \mathcal{F} & & \uparrow \mathcal{F}^{-1} \\ S_{image}/OTF & = & S_{object} \end{array}$$

Figure 1.6: Deconvolution Process.

Several blind deconvolution methods have been developed to estimate the OTF from images that were created by unknown psfs and are discussed in Section 2.2.

1.2.5 Polarimeter Imaging. A very basic polarimeter is constructed using a polarizing beam splitter (PBS). If incident light with a vertical polarization is transmitted by the PBS then incident light with a horizontal component is reflected. This results in two simultaneous images differing only by the polarization components. The light from the object, $o(z, w)$, is a composite of the orthogonal components, $o_h(z, w)$ and $o_v(z, w)$. Therefore $o(z, w) = o_h(z, w) + o_v(z, w)$. Using this equation and applying Equation 1.1 to a polarimeter results in the corresponding intensity images, $i_h(z, w)$ and $i_v(z, w)$, such that

$$i_h(x, y) = \sum_z \sum_w h(x - z, y - w) o_h(z, w), \quad (1.3)$$

and

$$i_v(x, y) = \sum_z \sum_w h(x - z, y - w) o_v(z, w). \quad (1.4)$$

The diversity between the two images is created by the polarizing effects of the object observed. The wavefront for both images is assumed to be identically distorted by the atmospheric turbulence and, thus, the same psf $h(x, y)$ is used. This reduces the number of unknowns between the two equations and is, thus, an advantage over traditional blind deconvolution. Developing a useful relationship between $o_h(z, w)$

and $o_v(z, w)$ would further reduce the number of unknowns to be estimated from the measured data.

1.3 Layout of the Dissertation document

The goal of this research is to understand the issues involved with viewing objects with a polarimeter and develop a method to improve spatial resolution with the additional polarity data that it provides. Three objectives are defined to achieve this goal followed by the results of the algorithm development.

1.3.1 Polarimeter Spatial Resolution Bounds. The first objective is an investigation of the Cramer-Rào Lower Bound (CRLB) for spatial resolution of a two-channel polarimeter. The CRLB is used to determine if the additional polarization information provides any grounds for improvement in spatial resolution over standard imaging techniques. The bounds are built in several steps. Starting with development of the CRLB of a standard imaging system without atmospheric effects [43] and building to the CRLB of a two-channel polarimeter incorporating atmospheric effects [42]. The CRLB development is presented in Chapter III along with a comparison of the polarimeter CRLB to standard imaging systems. Understanding the conditions in which the polarimeter can outperform standard imaging systems is the desired outcome for the objective.

1.3.2 Laboratory and Simulation Data. The second objective is to produce calibrated data for testing any developed algorithms. The laboratory setup used allows the controlled introduction of focus aberrations in the optical path. An innovative maximum-*a-priori* (MAP) estimation approach is developed in Section 4.2 that estimates the focus aberration present from a single image. The resulting images are then used to set the statistical properties of the Matlab® simulation and validate the performance of the deconvolution algorithms. The images used in development and testing of the polarimeter deconvolution algorithms are discussed in Chapter IV.

1.3.3 Polarimeter Deconvolution Algorithms. The third objective is to develop a method that uses the polarization data to improve spatial resolution. Initial development is under the assumption of a known psf with the results compared to a traditional deconvolution algorithm using a metric based on the fidelity of the deconvolved object. The algorithm is then extended to a polarimeter multiframe blind deconvolution approach similar to Schulz [36] but incorporating polarization information. The polarimeter deconvolution algorithm development is discussed in detail in Chapter V.

1.3.4 Results. Using both Matlab® simulation and calibrated laboratory images, the results of the algorithm development are detailed in Chapter VI. The significant improvements in fidelity of object deconvolution and convergence rates when compared to traditional methodologies are presented. Results for polarimeter deconvolution are presented for both known and unknown aberrations.

1.3.5 Conclusions and Recommendations. The conclusions drawn from the results of the algorithm development are presented in Chapter VII along with recommendations for follow-on research.

II. Historical Background

This chapter describes key concepts involved in developing a method to improve imaging using polarimeters. Starting with a brief description of a polarimeter and the properties of materials that produce polarized light. Section 2.2 follows the development of historical methods that led to blind deconvolution of imaging through turbulence. The final section briefly describes some acceleration techniques and bounds on imaging.

2.1 Polarimeters

A basic polarimeter is formed by splitting the incoming light with a PBS shown in Figure 2.1. The PBS splits the light into two orthogonally polarized beams. In this example, the reflected beam is arbitrarily designated to be vertically polarized, V_{pol} , while the transmitted beam is designated to be horizontally polarized, H_{pol} .

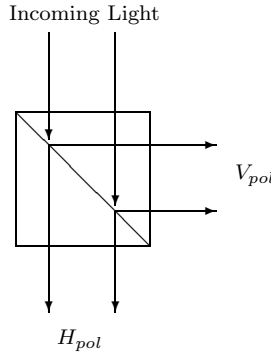


Figure 2.1: Basic Polarimeter.

2.1.1 Material Reflectance Models. An ideal PBS splits unpolarized light equally. However, when unpolarized light is reflected from certain materials it becomes partially polarized. A considerable amount of data is available on the polarization properties of materials due to reflectance. Active imaging polarization studies characterize properties of materials by varying the polarization states of the illumination and analyzing the reflected image. Some of the basic principles of reflectance from a metal are discussed in the following section.

From *Hecht* [16] the amplitude coefficient for reflection perpendicular to the surface is

$$r_{\perp} = \frac{n_i \cos \Theta_i - n_t \cos \Theta_t}{n_i \cos \Theta_i + n_t \cos \Theta_t} \quad (2.1)$$

and the amplitude coefficient for reflection parallel to the surface is

$$r_{\parallel} = \frac{n_t \cos \Theta_i - n_i \cos \Theta_t}{n_i \cos \Theta_t + n_t \cos \Theta_i} \quad (2.2)$$

where n is the index of refraction and Θ_i is the angle of incidence and Θ_t is the angle of transmission. The subscripts i and t indicate the incident or transmissive media at the reflective interface.

At normal incidence $\Theta_i = 0$, and r_{\parallel} and r_{\perp} simplify to

$$r_{\perp} = \frac{n_i - n_t}{n_i + n_t} \quad \text{and} \quad r_{\parallel} = \frac{n_t - n_i}{n_i + n_t}. \quad (2.3)$$

For reflectance $R_{\perp} = r_{\perp}^2$ and $R_{\parallel} = r_{\parallel}^2$. Squaring Equation 2.3 results in $R_{\perp} = R_{\parallel}$ for normally incident light. This is due to the homogeneous surface of the metal.

2.1.1.1 Plasma Frequency. From *Hecht* [16] “Free electrons and positive ions within a metal may be thought of as a plasma whose density oscillates at a natural frequency ω_p , the plasma frequency” The plasma frequency is related to the plasma wavelength through the equation $\omega_p = 2\pi c/\lambda_p$ where λ_p is the plasma frequency and c is the speed of light in a vacuum. The dispersion equation using ω_p becomes

$$n^2(\omega) = 1 - (\omega_p/\omega)^2. \quad (2.4)$$

The following can be observed from Equation 2.4:

- When $\omega = \omega_p$ then $n(\omega) = 0$.
- When $\omega > \omega_p$ then $n(\omega)$ is real and the metal is transparent. (See left image in Figure 2.2.)

- When $\omega < \omega_p$ then $n(\omega)$ is complex. (See right image in Figure 2.2.)

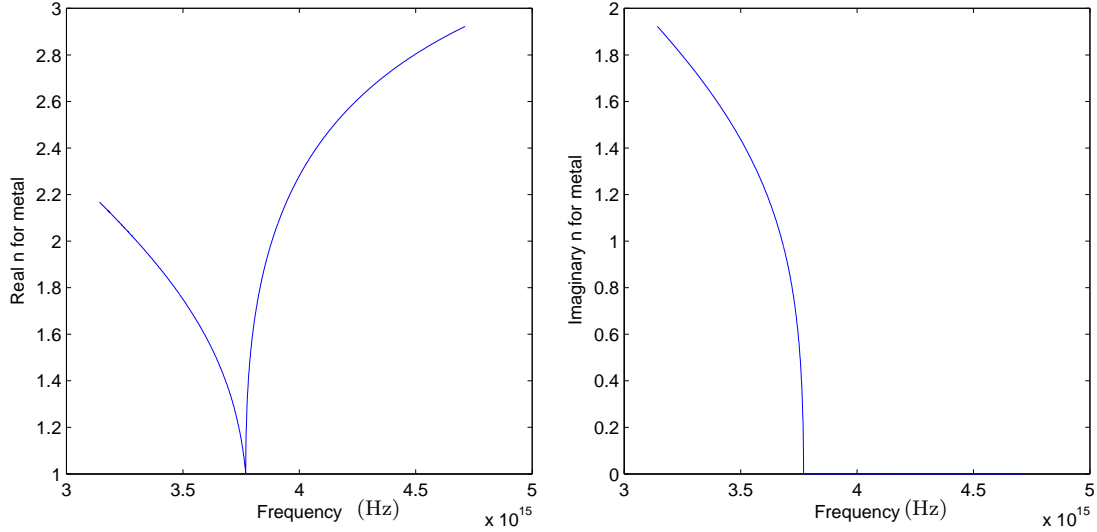


Figure 2.2: Real and Imaginary Components of \tilde{n} .

Mandel and Wolf [26] state that the relationship between the refractive index of the medium, $n(\omega)$, and the dielectric susceptibility, $\tilde{n}(\omega)$ in “a medium whose macroscopic properties do not change in time” is

$$n^2(\omega) = 1 + 4\pi\tilde{n}(\omega) \quad (2.5)$$

where ω is the frequency of interest. (Note the different notation of where the \tilde{n} is located.)

The equation from *Hecht* [16] for reflectance is

$$R = \frac{(n_R - 1)^2 + n_I^2}{(n_R + 1)^2 + n_I^2}. \quad (2.6)$$

Using Equations 2.4 and 2.5 yields the following:

$$\begin{aligned} n^2(\omega) &= 1 + 4\pi\tilde{n}(\omega) \\ &= 1 + 4\pi(1 - (\omega_p/\omega)^2)^{\frac{1}{2}} \end{aligned} \quad (2.7)$$

$$n(\omega) = (1 + 4\pi(1 - (\omega_p/\omega)^2)^{\frac{1}{2}})^{\frac{1}{2}} \quad (2.8)$$

$$n_R = \Re e(n(\omega)) \quad (2.9)$$

$$n_I = \Im m(n(\omega)) \quad (2.10)$$

Plugging these results into Equation 2.6 yields the reflectance shown in Figure 2.3.

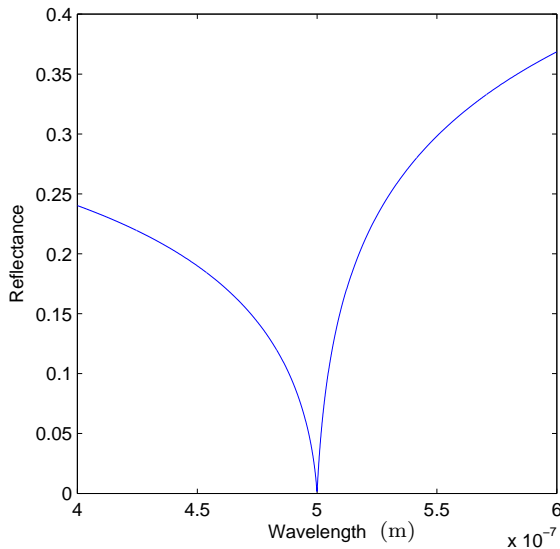


Figure 2.3: Reflectance versus Wavelength.

If one were to adjust the plasma frequency to approximately $0.31\mu\text{m}$ and add an offset of $n = 0.35$ (the refractive index of silver [41]) to the refractive index given by *Mandel* and *Wolf* then the resultant graph (see Figure 2.4) resembles the plot of the reflectance of silver as reproduced from Figure 4.59 in *Hecht* [16].

These models relate the reflectance of different materials with the polarization states produced by reflection from that material. This supports the notion that

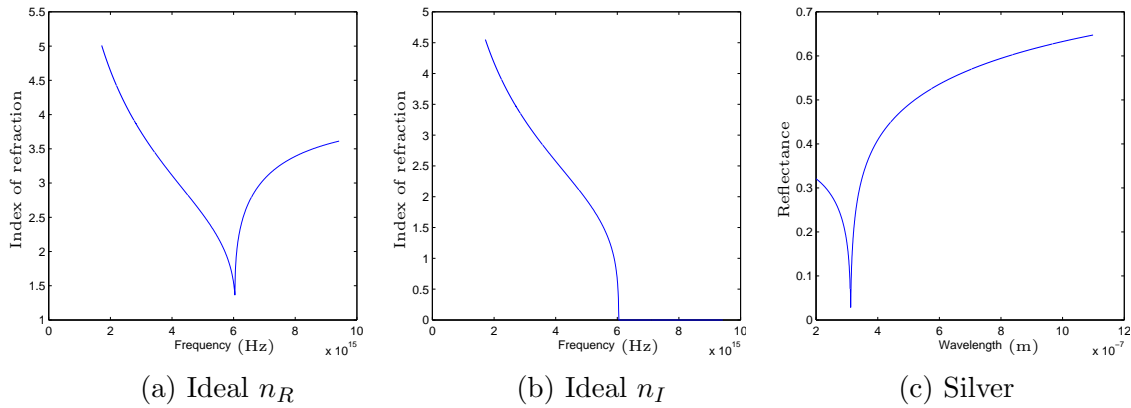


Figure 2.4: Predicted n_R , n_I , and Reflectance of Silver.

polarization data might be usable in identifying materials and/or the orientation of the surface from which the light is reflected.

2.2 *Blind Deconvolution*

This section discusses the development of approaches to the ill-posed problem of blind deconvolution. First general deconvolution techniques assuming a known psf are presented. Then approaches for blind deconvolution with standard imaging systems are presented, along with a few means of accelerating their typically lengthy execution times. Finally, a couple of papers relatating to lower bounds of resolution on imaging systems are presented.

2.2.1 Single Channel. In 1972, *Gerchberg and Saxton* [13] presented an algorithm “for the rapid solution of the phase of the complete wave function whose intensity in the diffraction and imaging planes of an imaging system are known.” The algorithm iterates back and forth between the two planes via Fourier transforms. The problem is constrained by the “degree of temporal and/or spatial coherency of the wave.” Additionally, the constraint of the magnitudes between the two planes results in a non-convex set in the image space according to *Combettes* [6]. The algorithm is outlined in Figure 2.5.

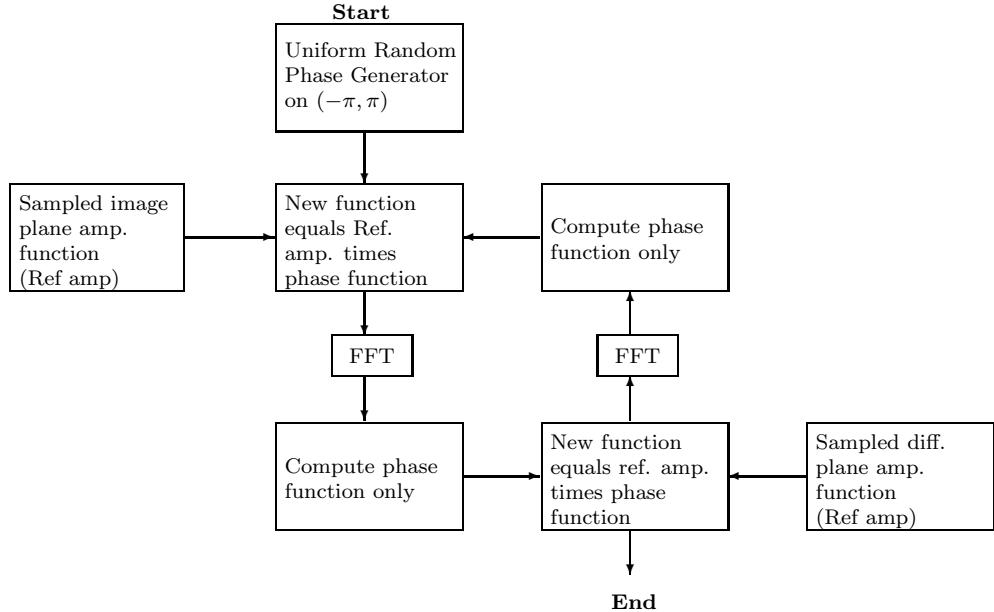


Figure 2.5: Gerchberg-Saxton Algorithm [13].

The inputs to the algorithm are the two input amplitude functions (Ref amp) from the image and diffraction planes. A uniformly random phase generator is used to give the algorithm an initial starting point. *Gerchberg* and *Saxton* offer a proof that the squared error between the results of the Fourier transforms and the input amplitude functions must decrease or remain the same on each iteration. They also point out that the solution reached is not unique.

Also, in 1972, *Richardson* introduced the use of Bayesian-based probability methods to restore noisy degraded images with a known psf. This was an improvement over the Fourier transform methods that performed well in a noiseless environment but degraded quickly with increased noise. The degraded image, H , is the convolution of the original image, W , with the point spread function, S , where all three are assumed to be discrete probability distribution functions. Two assumptions are made:

- S is normalized with respect to amplitude,
- The total energy in H is equivalent to the total energy in W .

An iterative algorithm is developed using Bayes' Theorem.

The initial estimate assumes a uniform distribution and results in the initial equation

$$W_{i,j,1} = \sum_{m=i}^e \sum_{n=j}^f \frac{H_{m,n} S_{m-i+1,n-j+1}}{\sum_{p=a}^b \sum_{q=c}^d S_{m-p+1,n-q+1}} \quad (2.11)$$

and subsequent iterations have the form

$$W_{i,j,r+1} = W_{i,j,r} \sum_{m=i}^e \sum_{n=j}^f \frac{H_{m,n} S_{m-i+1,n-j+1}}{\sum_{p=a}^b \sum_{q=c}^d W_{p,q,r} S_{m-p+1,n-q+1}}, \quad (2.12)$$

where

$$a = (1, m - K + 1)_{max}; \quad b = (m, I)_{min};$$

$$c = (1, n - L + 1)_{max}; \quad d = (n, J)_{min};$$

$$e = i + K - 1; \quad f = j + L - 1;$$

$$i = \{1, I\}; \quad j = \{1, J\}.$$

K, L are the dimensions of $S_{k,l}$.

I, J are the dimensions of $W_{i,j}$.

After the initial estimate, the W term on the right side of Equation 2.12 acts as a corrective factor to the convergence of the algorithm. The approach seems to keep S fixed throughout the execution of the algorithm. The algorithm demonstrated convergence in all cases tried by *Richardson* but no proof of convergence was developed.

In 1974, *Lucy* [25] introduced another iterative technique based on increasing the likelihood of the observed sample each iteration. It is derived from Bayes' Theorem and conserves the normalization and non-negativity constraints of astronomical images. The combination of both the Richardson algorithm and the Lucy algorithm is commonly referred to as the Richardson-Lucy (RL) algorithm.

In 1982, *Fienup* [8] compares iterative phase retrieval algorithms to steepest-descent gradient search techniques along with other algorithms. He discusses convergence rates and details some error functions for the algorithms. The first algorithm

discussed is the error-reduction algorithm which is a generalized Gerchberg-Saxton (GS) algorithm. It is applicable to the recovery of phase from two intensity measurements, like the GS algorithm, as well as one intensity measurement with a known constraint. In the area of astronomy, the known constraint is the non-negativity of the source object.

The error-reduction algorithm consists of the following four steps:

1. Fourier transform $g_k(x)$ producing $G_k(u)$
2. Make minimum changes in $G_k(u)$ which allow it to satisfy the Fourier domain constraints producing $G'_k(u)$
3. Inverse Fourier transform $G'_k(u)$ producing $g'_k(x)$
4. Make minimum changes to g'_k which allow it to satisfy the object domain constraints yielding $g_{k+1}(x)$

where $g_k(x)$ and $G'_k(u)$ are estimates of $f(x)$ and $F(u)$, respectively.

For problems in astronomy with a single intensity image, the first three steps are identical to the first three steps of the GS algorithm. The fourth step applies the non-negativity constraint such that

$$g_{k+1}(x) = \begin{cases} g'_k(x) & x \notin \gamma_k, \\ 0 & x \in \gamma_k \end{cases} \quad (2.13)$$

where γ is the set of points dependant on k , where $g'_k(x)$ violates the non-negativity constraint, i.e. where $g'_k(x) < 0$.

For the case of a single intensity measurement with constraint, Fienup's error measure is

$$E_k^2 = \sum_{x \in \gamma_k} [g'_k(x)]^2. \quad (2.14)$$

He found that the “error-reduction algorithm usually decreases the error rapidly for the first few iterations but much more slowly for later iterations.” He states that

for the single image case convergence is “painfully slow” and unsatisfactory for that application.

According to *Fienup* [8] a method proven to converge faster for both cases is the input-output (IO) algorithm. The IO algorithm differs from the error-reduction algorithm only in the object domain. The first three operations are the same for both algorithms. If those three operations are grouped together as shown in Figure 2.6 they can be viewed as a nonlinear system having input g and output g' . “The input $g(x)$ no longer must be thought of as the current best estimate of the object; instead it can be thought of as the driving function for the next output, $g'(x)$.”

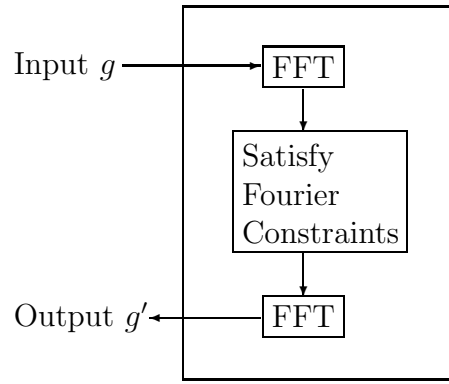


Figure 2.6: Input-Output Algorithm [8].

The basic IO algorithm uses the following step to get the next estimate

$$g_{k+1}(x) = \begin{cases} g_k(x) & x \notin \gamma_k, \\ g_k(x) - \beta g'_k(x) & x \in \gamma_k. \end{cases} \quad (2.15)$$

The output-output algorithm is a modified IO algorithm and uses the following step to get the next estimate

$$g_{k+1}(x) = \begin{cases} g'_k(x) & x \notin \gamma_k, \\ g'_k(x) - \beta g'_k(x) & x \in \gamma_k. \end{cases} \quad (2.16)$$

The hybrid IO algorithm uses the following step to get the next estimate

$$g_{k+1}(x) = \begin{cases} g'_k(x) & x \notin \gamma_k, \\ g_k(x) - \beta g'_k(x) & x \in \gamma_k. \end{cases} \quad (2.17)$$

“The hybrid input-output algorithm is an attempt to avoid a stagnation problem that tends to occur with the output-output algorithm.” The output-output algorithm can stagnate with no means to get out of this state, but the hybrid input continues to grow until the output becomes non-negative.

Fienup analyzed the performance differences between the gradient search and the various IO algorithms for the case of phase retrieval from a single intensity image. Various values of β are used in the experiments. The optimal β value varied with the input and the algorithm. The hybrid seemed to have the best overall performance but was unstable and tends to move to a worse error before decreasing to a lower error than the other algorithms.

In 1988, *Ayers* and *Dainty* [1] introduced another iterative method for the blind deconvolution of two convolved functions

$$c(x) = \int_{-\infty}^{\infty} f(x_1)g(x - x_1)dx_1. \quad (2.18)$$

It is similar to the iterative error-reduction algorithm but requires *a priori* knowledge of both functions convolved to produce the single convolved image. A flow chart of the algorithm is shown in Figure 2.7.

A priori information is required for this algorithm. The example given assumes non-negativity of both functions $f(x)$ and $g(x)$. A non-negative initial estimate $\tilde{f}_o(x)$ is generated as the starting point. This is Fourier transformed to produce $\tilde{F}(u)$ in Step 1. Then $\tilde{F}(u)$ is inverted to form an inverse filter and multiplied by $C(u)$ to produce an estimate $G(u)$. Step 3 inverse Fourier transforms $G(u)$ to produce $g(x)$. The image constraints are imposed by setting all points in $g(x)$ that are negative to zero yielding

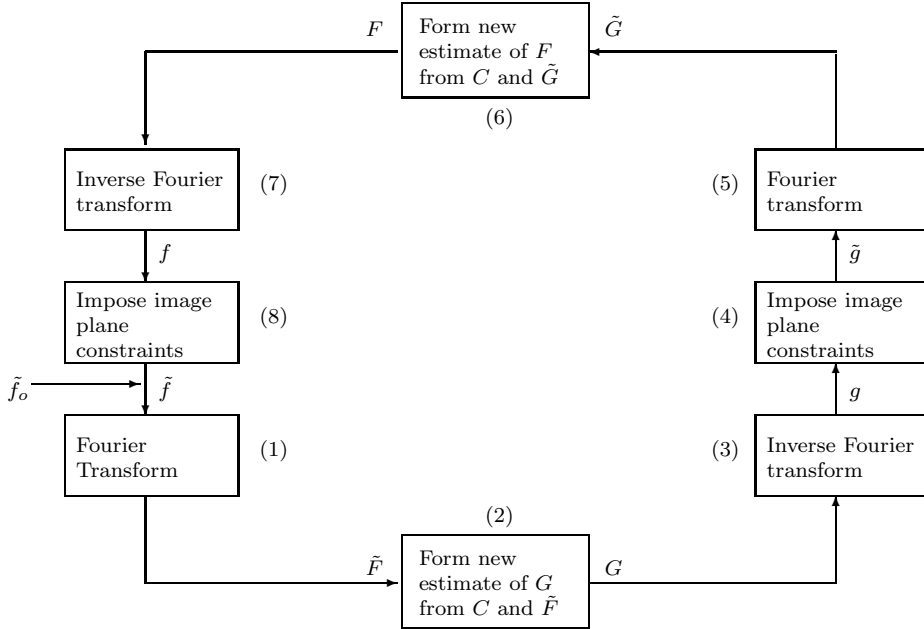


Figure 2.7: Ayers and Dainty Algorithm [1].

$\tilde{g}(x)$. In Step 5 a Fourier transforms of $\tilde{g}(x)$ produces $\tilde{G}(u)$. Step 6 inverts $\tilde{G}(u)$ to produce another inverse filter and multiplies by $C(u)$ to yield the spectrum estimate $F(u)$. Step 7 inverse Fourier transforms $F(u)$ to produce the function estimate $f(x)$ and the non-negativity constraint is applied to complete the loop.

Two major problems with this algorithm are:

1. The inverse filters in Steps 2 and 6 are problematic due to inverting regions of low values.
2. Zeros at particular spatial frequencies in either $F(u)$ or $G(u)$ result in voids at those frequencies in the convolution.

The non-negativity constraint is imposed similarly to previous algorithms with an additional energy conservation that seems to increase the rate of convergence and

is defined as:

$$\tilde{f}_i(x) = \begin{cases} f_i(x), & f_i(x) \geq 0, \\ 0, & \text{otherwise,} \end{cases} \quad (2.19)$$

$$E = \int_{-\infty}^{\infty} [f_i(x) - \tilde{f}_i(x)] dx, \quad (2.20)$$

$$\tilde{f}_i(x) = \tilde{f}_i(x) + E/N. \quad (2.21)$$

where N is the number of pixels in the image.

The Fourier domain constraint is more complicated, partly to mitigate the two significant problems pointed out previously, and are summarized as follows:

$$\text{if } |C(u)| < \text{noise level}, \text{ then } F_{i+1}(u) = \tilde{F}_i(u), \quad (2.22)$$

$$\text{if } |\tilde{G}_i(u)| \geq |C(u)|, \text{ then } F_{i+1}(u) = (1 - \beta)\tilde{F}_i(u) + \beta \frac{C(u)}{\tilde{G}_i(u)}, \quad (2.23)$$

$$\text{if } |\tilde{G}_i(u)| < |C(u)|, \text{ then } \frac{1}{F_{i+1}(u)} = \frac{(1 - \beta)}{\tilde{F}_i(u)} + \beta \frac{\tilde{G}_i(u)}{C(u)} \quad (2.24)$$

where $0 \leq \beta \leq 1$. On each iteration the two Fourier domain estimates are averaged. The averaging does not affect the convergence rate, however, the convergence rate is dependent on β , but no method of finding the optimal value of β was found.

An additional method to address extended regions of low or zero values is introduced. A weighting function is introduced that is non-zero up to some band-limit. The one used by Ayers and Dainty is the one that naturally occurs with the incoherent transfer function of a circular aperture. After a new spectrum estimate is produced by the averaging process it is multiplied by the weighting function. Then, “after subsequent imposition of the image domain constraints the updated spectrum estimate is divided by the weight function.”

Ayers and Dainty stress “that the uniqueness and convergence properties of the deconvolution algorithm are uncertain and that the effect of various amounts of noise existing in the convolution data” is unknown.

In 1990, *Seldin* and *Fienup* [39] applied the Ayers and Dainty (AD) algorithm to the specific case of phase retrieval. The algorithm is compared to the error-reduction and hybrid input-output algorithms previously discussed with various levels of additive Gaussian noise. Instead of implementing the Fourier domain constraint in Equation 2.22 outlined by Ayers and Dainty, *Seldin* and *Fienup* use a Wiener-Helstrom filter instead. The end result is an algorithm that differs from the error-reduction algorithm only in the Fourier-domain constraint. The Fourier-domain constraint for the error-reduction algorithm is

$$F_k(u) = \tilde{F}_k(u) \frac{|F(u)|}{|\tilde{F}_k(u)|} \quad (2.25)$$

and the Fourier-domain constraint for the AD algorithm is

$$F_k(u) = \tilde{F}_k(u) \frac{|F(u)|^2}{|\tilde{F}_k(u)|^2}. \quad (2.26)$$

Seldin and *Fienup* show that the error-reduction algorithm and the AD algorithm are similar both in form and in performance. The error-reduction algorithm seemed to perform better at higher noise levels than the AD algorithm but the hybrid IO algorithm clearly outperformed both of them.

In 1992, *Holmes* [18] introduced an iterative expectation-maximization (EM) approach to the blind deconvolution problem. Primary focus is on wide-field and confocal fluorescence microscopy. *Holmes* extends the maximum-likelihood (ML) estimation introduced by Shepp and Vardi [40] to incoherent imaging. Two constraints are imposed on the algorithm:

1. Symmetry Constraint - A circular symmetry based on the impulse response function is imposed but can be generalized to incorporate other constraints.
2. Band-limit Constraint - The knowledge of the band-limit of the OTF of the optical system is used to constrain the solution of the impulse response.

Their study is a “first attempt at this type of approach” with initial results showing the potential use of ML estimation for blind deconvolution. Extending the results to use MAP estimation or a penalized log-likelihood approach is recommended.

Also in 1992, *Ivanov et al.* [20] introduced gradient procedures for the Gerchberg-Saxton algorithm. Numerical simulation resulted in:

- Improved convergence;
- Wider range of reconstruction;
- Better stability in the presence of additive noise.

Their experimental data confirmed the numerical simulation. The use of Zernike polynomials was also introduced for representation of the phase function.

Fish et al [10] developed a blind-deconvolution algorithm based on the RL algorithm. The algorithm starts with an initial guess for both the psf and the object. The algorithm then switches back and forth between m iterations to estimate the next psf and m iterations to estimate the next object. Better performance is obtained when *a priori* information is used to influence the initial guess of the psf.

In 2002, *Jefferies et al.* [21] discuss the use of a constraint on blind deconvolution. The constraint, in this case, is obtained from a bispectrum-based speckle imaging algorithm. The Fourier phase of the speckle image is used to constrain the recovered phase estimated by the blind deconvolution algorithm. The reconstructed object intensity distribution is modeled as

$$f(x) = [\theta(x) \otimes \omega(x)]^2 \quad (2.27)$$

where $\theta(x)$ are the variables to be determined, $\omega(x)$ is a regularizing function that constrains the spatial frequencies of the reconstructed image, x represents individual pixels, and \otimes is the convolution operation. By estimating the individual $\theta(x)$ values, positivity of $f(x)$ is naturally enforced. The individual pixel *psf* model in the image

domain is

$$h(x) = [\varphi^2(x) \otimes \eta(x)] \{ \Sigma_x [\varphi^2(x) \otimes \eta(x)] \}^{-1} \quad (2.28)$$

where $\varphi(x)$ are the variables to be determined, $\eta(x)$ is the band-limited function

$$\eta(x) = \left| N^{-2} \Sigma_u P(u) e^{i2\pi(u \cdot x)/N} \right|^2, \quad (2.29)$$

and $P(u)$ is the pupil function. The MAP estimates of the object and psf are obtained by minimizing the error developed through the use of a conjugate gradient routine. The added constraint from the speckle imaging improves the convergence properties of the blind deconvolution algorithm by narrowing the search space.

In 2004, *Likas* and *Galatsanos* [24] introduced a “variational approximation approach for Bayesian blind image deconvolution.” This approach can be viewed as a generalization of the EM algorithm. In an improvement over an EM algorithm, this approach allows the incorporation of priors for both the image and the psf. It “was first introduced in the machine learning community to solve Bayesian inference problems with complex probabilistic models.” They demonstrate improved performance over previous methods through numerical experiments. The main shortcoming claimed of the methodology is that there is no analytical way to evaluate the tightness of the variational bound.

2.2.2 Wave-front sensing. Several other methods exist, specifically for detecting the aberrations present in an electro-optical (EO) imaging system. One method is the Hartmann wavefront sensor [29]. The Hartmann wavefront sensor, developed in the late 1960s, requires a beam splitter to divert some of the collimated light in an imaging system to a lens array. Each lens in the array produces an individual spot image. The displacement in the location of the spot image is used to calculate the tilt of its wavefront. The tilts are then integrated across the whole aperture to form the complete wavefront. A second method is the use of phase diversity imaging [28]. It is a technique for detecting aberrations using a second diversity im-

age with a known aberration. The known aberration is usually a highly calibrated focus error placed in the optical path after a beam-splitter. The resulting image is the diversity image. The difference between the conventional image and the diversity image is used to estimate the wavefront.

A more recent method introduced in 1988 is curvature sensing [31]. Curvature sensing involves the use of two imaging planes equidistant from the primary imaging plane. The difference in irradiance between the two images is used to calculate the curvature in the wavefront. The sensitivity of the curvature sensor in comparison to a Shack-Hartmann sensor is equivalent [32]. This method requires complicated optics in order to capture both imaging planes simultaneously. For near-simultaneous images, a membranous mirror can be used to change the focus between the two required planes. In separate developments, more recent research resulted in curvature sensing from a single defocused image [17] and the use of a beam splitting cube to produce the two simultaneous images on a single charge-coupled device (CCD) [3].

All of these methods require light to be diverted from the main image to the sensor. Diverting light from the main image results in a lower signal-to-noise ratio (SNR) for the primary channel. In addition, complicated or highly calibrated equipment is required. An approach used to mitigate this problem is to use multiple image frames.

2.2.3 Multi-frame. In 1993, *Schulz* [36] used ML estimation techniques in a multiframe blind deconvolution (MFBD) algorithm. He describes an approach to blind deconvolution using a sequence of short-exposure images. Short-exposure images retain more diffraction-limited information than long-exposure images. However, the trade is that the images are at reduced light levels. To overcome this, a sequence of short-exposure images is used to increase performance. The intensity image of each frame is

$$i_k(y; o, h_k) = \sum_{x \in \mathcal{X}} h_k(y|x)o(x), \quad y \in \mathcal{Y} \quad (2.30)$$

where x and y are the two-dimensional coordinates in the object and image planes, respectively. The psf, $h_k()$, is different for each frame, k , but the object is assumed to be the same for all frames. Using this relationship and the Poisson noise model, the log-likelihood developed is

$$L(o, h) = \sum_{k=1}^K \left[-\sum_{y \in \mathcal{Y}} i_k(y; o, h_k) + \sum_{y \in \mathcal{Y}} d_k(y) \ln(i_k(y; o, h_k)) \right]. \quad (2.31)$$

Schulz also implements a penalized ML technique to avoid convergence to the trivial solution of a point source as the estimated image and the estimates of the *psf* is the data.

2.2.4 Multi-channel. No articles referencing blind deconvolution using multiple channels are currently published. However, in 2004, Cain [5] discusses multichannel parameter estimation where two distinct channels have a parameter in common. The two distinct channels on the Geostationary Operational Environmental Satellite (GOES) are used to estimate the temperature of the cloud tops that both channels observe. The more accurate temperature estimate leads to achievement of a higher spatial resolution by the GOES. A similar approach could be taken to estimate the angle of the reflecting surface producing the polarization observed by a polarimeter. A more accurate estimation of the polarization might lead to a similar increase in the spatial resolution achieved by the polarimeter.

2.3 Acceleration Techniques

Iterative blind deconvolution algorithms are slow. Several techniques previously discussed were developed to accelerate the rate of convergence of the iterative algorithms. However, only a few papers were found that reflect an attempt to make use of computational techniques such as parallel implementations or use of genetic algorithms to accelerate convergence to a solution. These papers are discussed briefly.

2.3.1 Parallel Implementation. In [38] *Schulze* presents parallelization techniques for both bispectrum and blind deconvolution and compares them with their serial counterparts. The parallel blind deconvolution implemented is for multiframe blind deconvolution. The parallelization breaks up the sequence of individual frames and distributes the individual frames among additional processors. Using 16 frames of data, a single serial image recovery required 87 seconds versus 24 seconds for nine processors.

Ingleby and *McGaughey* [19] present an algorithm for parallel multiframe blind deconvolution using wavelength diversity. They use a sequence of images that are simultaneously collected at M multiple wavelengths. The assumption of common path-length errors between the channels is exploited to improve the multiframe blind deconvolution algorithm performance. The parallelization comes from the simultaneous collection of multiple imaging channels. Each individual channel is processed by the multiframe blind deconvolution algorithm.

2.3.2 Genetic Algorithms. *Schmalz* [34, 35] published the only two papers found that discuss an evolutionary algorithm (EA) approach to blind deconvolution. The first paper is an initial exploration into the feasibility of an EA approach to blind deconvolution. The second paper expands the analysis of the previous paper's genetic algorithm settings versus convergence and adds an additional constraint on the psf. The performance of the algorithm is analyzed as the number of psf side lobes expected is varied.

Both papers have a fundamental problem with the objective function used. From [2], “the evaluation process of individuals in an evolutionary algorithm begins with the user-defined *objective function*,

$$f : A_x \rightarrow \mathbb{R} \quad (2.32)$$

where A_x is the object variable space.” According to [27], the objective function is “a mathematical statement of the task to be achieved.” In the Schmalz paper, the objective function is

$$g(\underline{a}, a) \quad (2.33)$$

where \underline{a} is the estimate, and a is original image. In the real world this is not possible since one does not have the original image to compare with the estimate. If one did have access to the original image, deconvolution is no longer required.

No other work was found in this area. EA approaches were considered during the development of this research but a realistic objective function was not found to allow a realistic solution.

2.4 Cramer-R o Lower Bounds

Several papers address various aspects of CRLBs on atmospheric turbulence parameters and polarimeters related to this research.

Schulz et al. [37] discuss CRLBs for estimation of Zernike parameters of turbulence induced wavefront abberations from conventional and Hartmann sensor images. The performance limit for the estimation of the first 30 Zernike coefficients, \hat{a} , is calculated for both a conventional image and the combination of images from a Hartmann sensor array. The collected data, \mathcal{D} , for all the detector elements is the set $\mathcal{D} = \{d[p]\}$ where p is the two-dimensional coordinates of the data/image and the conditional probability mass function of the data is

$$P(\mathcal{D}; a) = \prod_p e^{(-h[p; a])} (h[p; a])^{d[p]} / d[p]!, \quad (2.34)$$

where the psf for the individual images is

$$h(p; a) = \int w_p(y) h(y; a) dy. \quad (2.35)$$

$w_p(y)$ is a “normalized weighting function that models the spatial region of interest for the p th detector.” The individual elements of the Fisher information matrix are

$$[J(a)]_{nm} = -E \left[\frac{\partial^2 \ln P(\mathcal{D}; a)}{\partial a_n \partial a_m} \right] \quad (2.36)$$

and the Cramer-Rao lower bound for any unbiased estimator of an unknown Zernike parameter vector a is

$$E[(\hat{a} - a)(\hat{a} - a)^T] \geq [J(a)]^{-1} \quad (2.37)$$

where the inequality is understood to be entry-wise. However, since a is a random parameter vector the resulting lower bound is also random. Their results are the average of 200 realizations and the bound values are normalized by the expected number of photons.

Gamiz and *Belsher* [11, 12] discuss the effects of detection noise and calibration errors on the performance of a four-channel polarimeter. Their work “provides a framework for developing polarimeter designs with minimal noise sensitivity and evaluating the noise performance of existing designs.”

This chapter presented several topics from the description of a basic polarimeter to the development of approaches to blind deconvolution using standard electro-optical imaging systems. Additionally, previous CRLB calculations related to Zernike coefficient estimation and the effects of noise and calibration errors on polarimeters were presented. The development of the spatial resolution CRLB of a basic two-channel polarimeter is presented in the next chapter.

III. Polarimeter Cramer-R  o Lower Bounds on Spatial Resolution

This research utilizes statistical models to develop Cramer-Rao lower bounds (CRLB) for the resolution of a polarimetric sensor and a non-polarization sensitive imaging system. The first of the two cases consists of a single image of two point sources and is used for comparison with the second case. The second case models two simultaneous images that would result from the incoming beam of light passing through a polarizing beam splitter. Both cases assume an ideal unaberrated image collection with no atmospheric turbulence. The Fisher information (FI) matrices are then formed from the individual elements. The CRLBs, which are the lower bounds on the variances for the parameters estimated, are then produced from the FI matrix. The CRLBs are developed in three steps. The first is the development of the spatial resolution CRLB of a standard imaging system with a single channel without turbulence. The second step is to extend the spatial resolution CRLB to a two-channel polarimeter. The final step is to introduce an atmospheric turbulence model based on a Zernike polynomial phase screen. This is followed by a comparison of the polarimeter spatial resolution CRLB to that of a standard imaging system.

3.1 Bound for Unpolarized Primary Channel

The base case for this analysis uses two point sources as the image. The parameters estimated are the amplitudes of the two point sources (o_0 and o_1) and the separation distance (Δ). The CRLBs are then produced from the FI matrix developed from the image model.

3.1.1 Image model. The following probability mass function (PMF) is used for development of the single image used in this scenario

$$PMF_{(\Delta, o_0, o_1)} = \prod_x \prod_y \frac{i(x, y)^{d(x, y)} e^{-i(x, y)}}{d(x, y)!} \quad (3.1)$$

where $d(x, y)$ is the data or image captured and $i(x, y)$ is the noiseless image defined as

$$i(x, y) = \sum_z \sum_w h(x - z, y - w) o(z, w). \quad (3.2)$$

The term $o(z, w)$ is defined as

$$o(z, w) = o_0 \delta(z, w) + o_1 \delta(z - \Delta, w), \quad (3.3)$$

where δ is the Kronecker delta function, and o_0 and o_1 are the intensities of the two point sources in the image. The value Δ is the separation between the points. Therefore,

$$i(x, y) = \sum_z \sum_w h(x - z, y - w) (o_0 \delta(z, w) + o_1 \delta(z - \Delta, w)). \quad (3.4)$$

The point spread function [15] psf chosen for this analysis is a radial symmetric Gaussian centered at the origin $(0, 0)$ with variance $\sigma^2 > 0$,

$$h(x, y) = \frac{1}{2\pi\sigma^2} \exp\left[\frac{-(x^2 + y^2)}{2\sigma^2}\right]. \quad (3.5)$$

It is chosen for ease of computation of its derivative when shifted with respect to Δ . The derivative of the shifted psf is

$$h'(x - \Delta, y) = \frac{\partial}{\partial x} h(x - \Delta, y) = \frac{-x + \Delta}{2\pi\sigma^4} \exp\left[\frac{-((x - \Delta)^2 + y^2)}{2\sigma^2}\right] \quad (3.6)$$

and is required to compute certain derivatives of the image with respect to Δ .

The log-likelihood function $\mathbf{L}(L_0, L_1, L_2)$ is the log of the *PMF*. For the three parameter case in this scenario $L_0 = \Delta$, $L_1 = o_0$, and $L_2 = o_1$.

$$\begin{aligned}\mathbf{L}(\Delta, o_0, o_1) &= \ln\left(\prod_x \prod_y \frac{i(x, y)^{d(x, y)} e^{-i(x, y)}}{d(x, y)!}\right) \\ &= \sum_x \sum_y [d(x, y) \ln(i(x, y)) - i(x, y) - \ln(d(x, y)!)] \\ &= \sum_x \sum_y [d(x, y) \ln(i(x, y)) - i(x, y)] - \sum_x \sum_y \ln(d(x, y)!).\end{aligned}\quad (3.7)$$

3.1.2 Fisher Information Matrix and CRLB. The CRLB for the individual coefficients estimated are [45]

$$\sigma_i^2 \geq J^{ii} = [J^{-1}]_{ii} \quad (3.8)$$

where J is the Fisher information matrix and is defined as follows:

$$J = \begin{bmatrix} J_{\Delta\Delta} & J_{\Delta o_0} & J_{\Delta o_1} \\ J_{o_0\Delta} & J_{o_0 o_0} & J_{o_0 o_1} \\ J_{o_1\Delta} & J_{o_1 o_0} & J_{o_1 o_1} \end{bmatrix} \quad (3.9)$$

$$J_{ij} = -E\left[\frac{\partial^2 \mathbf{L}(\Delta, o_0, o_1)}{\partial L_i \partial L_j}\right] \quad (3.10)$$

where E is the expected value and

$$\begin{aligned}\frac{\partial^2 \mathbf{L}(\Delta, o_0, o_1)}{\partial L_i \partial L_j} &= \frac{\partial}{\partial L_i} \left[\frac{\partial}{\partial L_j} \left[\sum_x \sum_y [d(x, y) \ln(i(x, y)) - i(x, y)] \right] \right] \\ &= \frac{\partial}{\partial L_i} \left[\sum_x \sum_y \left[\frac{d(x, y)}{i(x, y)} \frac{\partial i(x, y)}{\partial L_j} - \frac{\partial i(x, y)}{\partial L_j} \right] \right] \\ &= \sum_x \sum_y \left[\frac{-d(x, y)}{i^2(x, y)} \frac{\partial i(x, y)}{\partial L_i} \frac{\partial i(x, y)}{\partial L_j} + \frac{d(x, y)}{i(x, y)} \frac{\partial^2 i(x, y)}{\partial L_i \partial L_j} - \frac{\partial^2 i(x, y)}{\partial L_i \partial L_j} \right] \\ &= \sum_x \sum_y \left[\frac{-d(x, y)}{i^2(x, y)} \frac{\partial i(x, y)}{\partial L_i} \frac{\partial i(x, y)}{\partial L_j} + \left(\frac{d(x, y)}{i(x, y)} - 1 \right) \frac{\partial^2 i(x, y)}{\partial L_i \partial L_j} \right]\end{aligned}\quad (3.11)$$

$$\begin{aligned}
-E \left[\frac{\partial^2 \mathbf{L}(\Delta, o_0, o_1)}{\partial L_i \partial L_j} \right] &= -E \left[\sum_x \sum_y \left[\frac{-d(x, y)}{i^2(x, y)} \frac{\partial i(x, y)}{\partial L_i} \frac{\partial i(x, y)}{\partial L_j} \right. \right. \\
&\quad \left. \left. + \left(\frac{d(x, y)}{i(x, y)} - 1 \right) \frac{\partial^2 i(x, y)}{\partial L_i \partial L_j} \right] \right] \\
&= - \sum_x \sum_y \left[\frac{-E[d(x, y)]}{i^2(x, y)} \frac{\partial i(x, y)}{\partial L_i} \frac{\partial i(x, y)}{\partial L_j} \right. \\
&\quad \left. + \left(\frac{E[d(x, y)]}{i(x, y)} - 1 \right) \frac{\partial^2 i(x, y)}{\partial L_i \partial L_j} \right] \\
&= - \sum_x \sum_y \left[\frac{-i(x, y)}{i^2(x, y)} \frac{\partial i(x, y)}{\partial L_i} \frac{\partial i(x, y)}{\partial L_j} \right. \\
&\quad \left. + \left(\frac{i(x, y)}{i(x, y)} - 1 \right) \frac{\partial^2 i(x, y)}{\partial L_i \partial L_j} \right] \\
&= - \sum_x \sum_y \left[\frac{-1}{i(x, y)} \frac{\partial i(x, y)}{\partial L_i} \frac{\partial i(x, y)}{\partial L_j} \right] \\
&= \sum_x \sum_y \left[\frac{1}{i(x, y)} \frac{\partial i(x, y)}{\partial L_i} \frac{\partial i(x, y)}{\partial L_j} \right]. \tag{3.12}
\end{aligned}$$

Therefore

$$J_{ij} = \sum_x \sum_y \left[\frac{1}{i(x, y)} \frac{\partial i(x, y)}{\partial L_i} \frac{\partial i(x, y)}{\partial L_j} \right]. \tag{3.13}$$

3.1.3 Derivatives of the Image. In order to calculate the derivatives of the image, one additional definition [7] is required. Let f be a continuous function defined on the interval $[t_1, t_2]$. Let $t_o \in [t_1, t_2]$. Then

$$\int_{t_1}^{t_2} f(t) \delta'(t - t_o) dt = (-1) f'(t_o). \tag{3.14}$$

The Fisher information matrix is then populated using the following three image derivatives:

$$\frac{\partial i(x, y)}{\partial \Delta} = \frac{\partial}{\partial \Delta} \sum_z \sum_w h(x - z, y - w) (o_0 \delta(z, w) + o_1 \delta(z - \Delta, w))$$

$$\begin{aligned}
&= \sum_z \sum_w h(x-z, y-w) o_1 \frac{\partial}{\partial \Delta} \delta(z-\Delta, w) \\
&= o_1 \sum_z \sum_w h(x-z, y-w) \partial'(z-\Delta) \partial(w) \\
&= -o_1 \frac{d}{dx} h(x-\Delta, y)
\end{aligned} \tag{3.15}$$

$$\begin{aligned}
\frac{\partial i(x, y)}{\partial o_0} &= \frac{\partial}{\partial o_0} \sum_z \sum_w h(x-z, y-w) (o_0 \delta(z, w) + o_1 \delta(z-\Delta, w)) \\
&= \sum_z \sum_w h(x-z, y-w) \delta(z, w) \\
&= h(x, y)
\end{aligned} \tag{3.16}$$

$$\begin{aligned}
\frac{\partial i(x, y)}{\partial o_1} &= \frac{\partial}{\partial o_1} \sum_z \sum_w h(x-z, y-w) (o_0 \delta(z, w) + o_1 \delta(z-\Delta, w)) \\
&= \sum_z \sum_w h(x-z, y-w) \delta(z-\Delta, w) \\
&= h(x-\Delta, y)
\end{aligned} \tag{3.17}$$

Using the previous results and Equation 3.14 the elements of the Fisher information matrix are

$$\begin{aligned}
J_{\Delta\Delta} &= -E \left[\frac{\partial^2 \mathbf{L}(\Delta, o_0, o_1)}{\partial \Delta \partial \Delta} \right] \\
&= \sum_x \sum_y \left[\frac{1}{i(x, y)} \frac{\partial i(x, y)}{\partial \Delta} \frac{\partial i(x, y)}{\partial \Delta} \right] \\
&= \sum_x \sum_y \left[\frac{1}{i(x, y)} \left(\frac{\partial i(x, y)}{\partial \Delta} \right)^2 \right] \\
&= \sum_x \sum_y \left[\frac{1}{i(x, y)} \left(-o_1 \frac{d}{dx} h(x-\Delta, y) \right)^2 \right] \\
&= o_1^2 \sum_x \sum_y \left[\frac{1}{i(x, y)} \left(\frac{d}{dx} h(x-\Delta, y) \right)^2 \right] \\
J_{\Delta o_0} &= -E \left[\frac{\partial^2 \mathbf{L}(\Delta, o_0, o_1)}{\partial \Delta \partial o_0} \right] \\
&= \sum_x \sum_y \left[\frac{1}{i(x, y)} \frac{\partial i(x, y)}{\partial \Delta} \frac{\partial i(x, y)}{\partial o_0} \right] \\
&= \sum_x \sum_y \left[\frac{1}{i(x, y)} \left(-o_1 \frac{d}{dx} h(x-\Delta, y) \right) (h(x, y)) \right]
\end{aligned} \tag{3.18}$$

$$= -o_1 \sum_x \sum_y \left[\frac{1}{i(x,y)} \left(\frac{d}{dx} h(x-\Delta, y) \right) (h(x,y)) \right] \quad (3.19)$$

$$\begin{aligned} J_{\Delta o_1} &= -E \left[\frac{\partial^2 \mathbf{L}(\Delta, o_0, o_1)}{\partial \Delta \partial o_1} \right] \\ &= \sum_x \sum_y \left[\frac{1}{i(x,y)} \frac{\partial i(x,y)}{\partial \Delta} \frac{\partial i(x,y)}{\partial o_1} \right] \\ &= \sum_x \sum_y \left[\frac{1}{i(x,y)} \left(-o_1 \frac{d}{dx} h(x-\Delta, y) \right) (h(x-\Delta, y)) \right] \\ &= -o_1 \sum_x \sum_y \left[\frac{1}{i(x,y)} \left(\frac{d}{dx} h(x-\Delta, y) \right) (h(x-\Delta, y)) \right] \end{aligned} \quad (3.20)$$

$$J_{o_0 \Delta} = J_{\Delta o_0} \quad (3.21)$$

$$\begin{aligned} J_{o_0 o_0} &= -E \left[\frac{\partial^2 \mathbf{L}(\Delta, o_0, o_1)}{\partial o_0 \partial o_0} \right] \\ &= \sum_x \sum_y \left[\frac{1}{i(x,y)} \frac{\partial i(x,y)}{\partial o_0} \frac{\partial i(x,y)}{\partial o_0} \right] \\ &= \sum_x \sum_y \left[\frac{1}{i(x,y)} h(x,y)^2 \right] \end{aligned} \quad (3.22)$$

$$\begin{aligned} J_{o_0 o_1} &= -E \left[\frac{\partial^2 \mathbf{L}(\Delta, o_0, o_1)}{\partial o_0 \partial o_1} \right] \\ &= \sum_x \sum_y \left[\frac{1}{i(x,y)} \frac{\partial i(x,y)}{\partial o_0} \frac{\partial i(x,y)}{\partial o_1} \right] \\ &= \sum_x \sum_y \left[\frac{1}{i(x,y)} (h(x,y)) (h(x-\Delta, y)) \right] \end{aligned} \quad (3.23)$$

$$J_{o_1 \Delta} = J_{\Delta o_1} \quad (3.24)$$

$$J_{o_1 o_0} = J_{o_0 o_1} \quad (3.25)$$

$$\begin{aligned} J_{o_1 o_1} &= -E \left[\frac{\partial^2 \mathbf{L}(\Delta, o_0, o_1)}{\partial o_1 \partial o_1} \right] \\ &= \sum_x \sum_y \left[\frac{1}{i(x,y)} \frac{\partial i(x,y)}{\partial o_1} \frac{\partial i(x,y)}{\partial o_1} \right] \\ &= \sum_x \sum_y \left[\frac{1}{i(x,y)} h(x-\Delta, y)^2 \right]. \end{aligned} \quad (3.26)$$

3.1.4 Cramer-R  o Lower Bound. The CRLBs or smallest possible variances of the estimated parameters are calculated by taking the inverse of the FI matrix. The

individual bounds are located along the diagonal of the resulting matrix.

$$J^{ij} = J^{-1} = \begin{bmatrix} \sigma_{\Delta}^2 & J^{\Delta o_0} & J^{\Delta o_1} \\ J^{o_0 \Delta} & \sigma_{o_0}^2 & J^{o_0 o_1} \\ J^{o_1 \Delta} & J^{o_1 o_0} & \sigma_{o_1}^2 \end{bmatrix} \quad (3.27)$$

Alternatively, the individual bounds can be found as follows

$$\sigma_{\Delta}^2 = \det \begin{bmatrix} 1 & 0 & 0 \\ 0 & J_{o_0 o_0} & J_{o_0 o_1} \\ 0 & J_{o_1 o_0} & J_{o_1 o_1} \end{bmatrix} \cdot \frac{1}{\det[J]} \quad (3.28)$$

$$\sigma_{o_0}^2 = \det \begin{bmatrix} J_{\Delta \Delta} & 0 & J_{\Delta o_1} \\ 0 & 1 & 0 \\ J_{o_1 \Delta} & 0 & J_{o_1 o_1} \end{bmatrix} \cdot \frac{1}{\det[J]} \quad (3.29)$$

$$\sigma_{o_1}^2 = \det \begin{bmatrix} J_{\Delta \Delta} & J_{\Delta o_0} & 0 \\ J_{o_0 \Delta} & J_{o_0 o_0} & 0 \\ 0 & 0 & 1 \end{bmatrix} \cdot \frac{1}{\det[J]} \quad (3.30)$$

3.2 Polarimeter Bounds without Atmospheric Distortion

Similar to the base case, two point sources comprise the image modeled. The parameters are expanded to include intensities of the point sources to be estimated in two polarized images. The scenario assumes a perfect PBS to produce the two images. Thus the parameters estimated are the amplitudes of the two point sources (o_{0h}, o_{0v}, o_{1h} and o_{1v}) and the separation distance (Δ). The CRLBs are then produced from the FI matrix developed from the image model in a similar manner to those in the base case. Additional discussion looks at the impact of a less than perfect PBS.

3.2.1 Image Model. The following PMF is used for development of the CRLB for a scenario using a sensor that captures two simultaneous images using the

two different polarity channels produced by a PBS:

$$PMF_{(\Delta, o_{0h}, o_{0v}, o_{1h}, o_{1v})} = \prod_x \prod_y \left(\frac{i_h(x, y)^{d_h(x, y)} e^{-i_h(x, y)}}{d_h(x, y)!} \right) \cdot \left(\frac{i_v(x, y)^{d_v(x, y)} e^{-i_v(x, y)}}{d_v(x, y)!} \right) \quad (3.31)$$

The image definitions for notation purposes arbitrarily define one image as the horizontally (h) polarized image and the other as the vertically (v) polarized image. The individual images are thus defined, similarly to the base case, as

$$i_h(x, y) = \sum_z \sum_w h(x - z, y - w)(o_{0h}\delta(z, w) + o_{1h}\delta(z - \Delta, w)) \quad (3.32)$$

$$i_v(x, y) = \sum_z \sum_w h(x - z, y - w)(o_{0v}\delta(z, w) + o_{1v}\delta(z - \Delta, w)) \quad (3.33)$$

The log-likelihood function for the dual polarity case is $\mathbf{L}(\Delta, o_{0h}, o_{0v}, o_{1h}, o_{1v})$. By development similar to that used for the base case, the result is:

$$\begin{aligned} \mathbf{L}(\Delta, o_{0h}, o_{0v}, o_{1h}, o_{1v}) &= \ln(PMF) \\ &\approx \sum_x \sum_y [d_h(x, y) \ln(i_h(x, y)) - i_h(x, y) + d_v(x, y) \ln(i_v(x, y)) - i_v(x, y)] \end{aligned}$$

3.2.2 Polarimeter Fisher Information Matrix and CRLB. The Fisher information matrix is composed of the following elements

$$\begin{aligned} J_{ij} &= -E \left[\frac{\partial^2 \mathbf{L}(\Delta, o_{0h}, o_{0v}, o_{1h}, o_{1v})}{\partial L_i \partial L_j} \right] \\ &= \sum_x \sum_y \left[\frac{1}{i_h(x, y)} \frac{\partial i_h(x, y)}{\partial L_i} \frac{\partial i_h(x, y)}{\partial L_j} + \frac{1}{i_v(x, y)} \frac{\partial i_v(x, y)}{\partial L_i} \frac{\partial i_v(x, y)}{\partial L_j} \right] \quad (3.34) \end{aligned}$$

such that

$$J = \begin{bmatrix} J_{\Delta\Delta} & J_{\Delta o_{0h}} & J_{\Delta o_{0v}} & J_{\Delta o_{1h}} & J_{\Delta o_{1v}} \\ J_{o_{0h}\Delta} & J_{o_{0h}o_{0h}} & J_{o_{0h}o_{0v}} & J_{o_{0h}o_{1h}} & J_{o_{0h}o_{1v}} \\ J_{o_{0v}\Delta} & J_{o_{0v}o_{0h}} & J_{o_{0v}o_{0v}} & J_{o_{0v}o_{1h}} & J_{o_{0v}o_{1v}} \\ J_{o_{1h}\Delta} & J_{o_{1h}o_{0h}} & J_{o_{1h}o_{0v}} & J_{o_{1h}o_{1h}} & J_{o_{1h}o_{1v}} \\ J_{o_{1v}\Delta} & J_{o_{1v}o_{0h}} & J_{o_{1v}o_{0v}} & J_{o_{1v}o_{1h}} & J_{o_{1v}o_{1v}} \end{bmatrix} \quad (3.35)$$

3.2.3 Polarimeter Image Derivatives. The individual derivatives of the image with respect to the parameters estimated are

$$\begin{aligned}
\frac{\partial i_n(x, y)}{\partial \Delta} &= \frac{\partial}{\partial \Delta} \sum_z \sum_w h(x - z, y - w) (o_{0n}\delta(x, y) + o_{1n}\delta(x - \Delta, y)) \\
&= \sum_z \sum_w h(x - z, y - w) \frac{\partial}{\partial \Delta} (o_{0n}\delta(x, y) + o_{1n}\delta(x - \Delta, y)) \\
&= \sum_z \sum_w h(x - z, y - w) o_{1n} \frac{\partial}{\partial \Delta} \delta(x - \Delta, y) \\
&= -o_{1n} \frac{d}{dx} h(x - \Delta, y)
\end{aligned} \tag{3.36}$$

$$\begin{aligned}
\frac{\partial i_h(x, y)}{\partial o_{0h}} &= \sum_z \sum_w h(x - z, y - w) \frac{\partial}{\partial o_{0h}} (o_{0h}\delta(x, y) + o_{1h}\delta(x - \Delta, y)) \\
&= \sum_z \sum_w h(x - z, y - w) \delta(x, y) \\
&= h(x, y)
\end{aligned} \tag{3.37}$$

$$\frac{\partial i_h(x, y)}{\partial o_{0v}} = 0 \tag{3.38}$$

$$\frac{\partial i_h(x, y)}{\partial o_{1h}} = h(x - \Delta, y) \tag{3.39}$$

$$\frac{\partial i_h(x, y)}{\partial o_{1v}} = 0 \tag{3.40}$$

$$\frac{\partial i_v(x, y)}{\partial o_{0h}} = 0 \tag{3.41}$$

$$\frac{\partial i_v(x, y)}{\partial o_{0v}} = h(x, y) \tag{3.42}$$

$$\frac{\partial i_v(x, y)}{\partial o_{1h}} = 0 \tag{3.43}$$

$$\frac{\partial i_v(x, y)}{\partial o_{1v}} = h(x - \Delta, y). \tag{3.44}$$

3.2.4 Individual FI Elements for Polarimeter. The individual elements of the FI matrix J are calculated using the image derivatives of the previous section and

are

$$\begin{aligned}
J_{\Delta\Delta} &= \sum_x \sum_y \left[\frac{1}{i_h(x, y)} \frac{\partial i_h(x, y)}{\partial \Delta} \frac{\partial i_h(x, y)}{\partial \Delta} + \frac{1}{i_v(x, y)} \frac{\partial i_v(x, y)}{\partial \Delta} \frac{\partial i_v(x, y)}{\partial \Delta} \right] \\
&= \sum_x \sum_y \left[\frac{1}{i_h(x, y)} \left(\frac{\partial i_h(x, y)}{\partial \Delta} \right)^2 + \frac{1}{i_v(x, y)} \left(\frac{\partial i_v(x, y)}{\partial \Delta} \right)^2 \right] \\
&= \sum_x \sum_y \left[\frac{1}{i_h(x, y)} \left(-o_{1h} \frac{d}{dx} h(x - \Delta, y) \right)^2 \right. \\
&\quad \left. + \frac{1}{i_v(x, y)} \left(-o_{1v} \frac{d}{dx} h(x - \Delta, y) \right)^2 \right] \\
&= \sum_x \sum_y \left[\left(\frac{o_{1h}^2}{i_h(x, y)} + \frac{o_{1v}^2}{i_v(x, y)} \right) \left(\frac{d}{dx} h(x - \Delta, y) \right)^2 \right] \tag{3.45}
\end{aligned}$$

$$\begin{aligned}
J_{\Delta o_{0h}} &= \sum_x \sum_y \left[\frac{1}{i_h(x, y)} \frac{\partial i_h(x, y)}{\partial \Delta} \frac{\partial i_h(x, y)}{\partial o_{0h}} + \frac{1}{i_v(x, y)} \frac{\partial i_v(x, y)}{\partial \Delta} \frac{\partial i_v(x, y)}{\partial o_{0h}} \right] \\
&= \sum_x \sum_y \left[\frac{1}{i_h(x, y)} \left(-o_{1h} \frac{d}{dx} h(x - \Delta, y) \right) h(x, y) \right. \\
&\quad \left. + \frac{1}{i_v(x, y)} \left(-o_{1v} \frac{d}{dx} h(x - \Delta, y) \right) \cdot 0 \right] \\
&= \sum_x \sum_y \left[\frac{1}{i_h(x, y)} \left(-o_{1h} \frac{d}{dx} h(x - \Delta, y) \right) h(x, y) \right] \\
&= -o_{1h} \sum_x \sum_y \left[\frac{1}{i_h(x, y)} \left(\frac{d}{dx} h(x - \Delta, y) \right) h(x, y) \right] \tag{3.46}
\end{aligned}$$

$$\begin{aligned}
J_{\Delta o_{0v}} &= \sum_x \sum_y \left[\frac{1}{i_h(x, y)} \frac{\partial i_h(x, y)}{\partial \Delta} \frac{\partial i_h(x, y)}{\partial o_{0v}} + \frac{1}{i_v(x, y)} \frac{\partial i_v(x, y)}{\partial \Delta} \frac{\partial i_v(x, y)}{\partial o_{0v}} \right] \\
&= \sum_x \sum_y \left[\frac{1}{i_h(x, y)} (0) + \frac{1}{i_v(x, y)} \left(-o_{1v} \frac{d}{dx} h(x - \Delta, y) \right) (h(x, y)) \right] \\
&= -o_{1v} \sum_x \sum_y \left[\frac{1}{i_v(x, y)} \left(\frac{d}{dx} h(x - \Delta, y) \right) (h(x, y)) \right] \tag{3.47}
\end{aligned}$$

$$\begin{aligned}
J_{\Delta o_{1h}} &= \sum_x \sum_y \left[\frac{1}{i_h(x, y)} \frac{\partial i_h(x, y)}{\partial \Delta} \frac{\partial i_h(x, y)}{\partial o_{1h}} + \frac{1}{i_v(x, y)} \frac{\partial i_v(x, y)}{\partial \Delta} \frac{\partial i_v(x, y)}{\partial o_{1h}} \right] \\
&= \sum_x \sum_y \left[\frac{1}{i_h(x, y)} \left(-o_{1h} \frac{d}{dx} h(x - \Delta, y) \right) (h(x - \Delta, y)) + \frac{1}{i_v(x, y)} (0) \right] \\
&= -o_{1h} \sum_x \sum_y \left[\frac{1}{i_h(x, y)} \left(\frac{d}{dx} h(x - \Delta, y) \right) (h(x - \Delta, y)) \right] \tag{3.48}
\end{aligned}$$

$$\begin{aligned}
J_{\Delta o_{1v}} &= \sum_x \sum_y \left[\frac{1}{i_h(x, y)} \frac{\partial i_h(x, y)}{\partial \Delta} \frac{\partial i_h(x, y)}{\partial o_{1v}} + \frac{1}{i_v(x, y)} \frac{\partial i_v(x, y)}{\partial \Delta} \frac{\partial i_v(x, y)}{\partial o_{1v}} \right] \\
&= \sum_x \sum_y \left[\frac{1}{i_h(x, y)} (0) + \frac{1}{i_v(x, y)} \left(-o_{1v} \frac{d}{dx} h(x - \Delta, y) \right) (h(x - \Delta, y)) \right] \\
&= -o_{1v} \sum_x \sum_y \left[\frac{1}{i_v(x, y)} \left(\frac{d}{dx} h(x - \Delta, y) \right) (h(x - \Delta, y)) \right] \tag{3.49}
\end{aligned}$$

$$\begin{aligned}
J_{o_{0h} o_{0h}} &= \sum_x \sum_y \left[\frac{1}{i_h(x, y)} \left(\frac{\partial i_h(x, y)}{\partial o_{0h}} \right)^2 + \frac{1}{i_v(x, y)} \left(\frac{\partial i_v(x, y)}{\partial o_{0h}} \right)^2 \right] \\
&= \sum_x \sum_y \left[\frac{1}{i_h(x, y)} (h(x, y))^2 + \frac{1}{i_v(x, y)} (0)^2 \right] \\
&= \sum_x \sum_y \left[\frac{1}{i_h(x, y)} (h(x, y))^2 \right] \tag{3.50}
\end{aligned}$$

$$\begin{aligned}
J_{o_{0h} o_{0v}} &= \sum_x \sum_y \left[\frac{1}{i_h(x, y)} \frac{\partial i_h(x, y)}{\partial o_{0h}} \frac{\partial i_h(x, y)}{\partial o_{0v}} + \frac{1}{i_v(x, y)} \frac{\partial i_v(x, y)}{\partial o_{0h}} \frac{\partial i_v(x, y)}{\partial o_{0v}} \right] \\
&= \sum_x \sum_y \left[\frac{1}{i_h(x, y)} (0) + \frac{1}{i_v(x, y)} (0) \right] \\
&= 0 \tag{3.51}
\end{aligned}$$

$$\begin{aligned}
J_{o_{0h} o_{1h}} &= \sum_x \sum_y \left[\frac{1}{i_h(x, y)} \frac{\partial i_h(x, y)}{\partial o_{0h}} \frac{\partial i_h(x, y)}{\partial o_{1h}} + \frac{1}{i_v(x, y)} \frac{\partial i_v(x, y)}{\partial o_{0h}} \frac{\partial i_v(x, y)}{\partial o_{1h}} \right] \\
&= \sum_x \sum_y \left[\frac{1}{i_h(x, y)} (h(x, y)) (h(x - \Delta, y)) + \frac{1}{i_v(x, y)} (0) \right] \\
&= \sum_x \sum_y \left[\frac{1}{i_h(x, y)} (h(x, y)) (h(x - \Delta, y)) \right] \tag{3.52}
\end{aligned}$$

$$\begin{aligned}
J_{o_{0h}o_{1v}} &= \sum_x \sum_y \left[\frac{1}{i_h(x, y)} \frac{\partial i_h(x, y)}{\partial o_{0h}} \frac{\partial i_h(x, y)}{\partial o_{1v}} + \frac{1}{i_v(x, y)} \frac{\partial i_v(x, y)}{\partial o_{0h}} \frac{\partial i_v(x, y)}{\partial o_{1v}} \right] \\
&= \sum_x \sum_y \left[\frac{1}{i_h(x, y)}(0) + \frac{1}{i_v(x, y)}(0) \right] \\
&= 0
\end{aligned} \tag{3.53}$$

$$\begin{aligned}
J_{o_{0v}o_{0v}} &= \sum_x \sum_y \left[\frac{1}{i_h(x, y)} \left(\frac{\partial i_h(x, y)}{\partial o_{0v}} \right)^2 + \frac{1}{i_v(x, y)} \left(\frac{\partial i_v(x, y)}{\partial o_{0v}} \right)^2 \right] \\
&= \sum_x \sum_y \left[\frac{1}{i_h(x, y)}(0) + \frac{1}{i_v(x, y)}(h(x, y))^2 \right] \\
&= \sum_x \sum_y \left[\frac{1}{i_v(x, y)}(h(x, y))^2 \right]
\end{aligned} \tag{3.54}$$

$$\begin{aligned}
J_{o_{0v}o_{1h}} &= \sum_x \sum_y \left[\frac{1}{i_h(x, y)} \frac{\partial i_h(x, y)}{\partial o_{0v}} \frac{\partial i_h(x, y)}{\partial o_{1h}} + \frac{1}{i_v(x, y)} \frac{\partial i_v(x, y)}{\partial o_{0v}} \frac{\partial i_v(x, y)}{\partial o_{1h}} \right] \\
&= \sum_x \sum_y \left[\frac{1}{i_h(x, y)}(0) + \frac{1}{i_v(x, y)}(0) \right] \\
&= 0
\end{aligned} \tag{3.55}$$

$$\begin{aligned}
J_{o_{00}o_{1v}} &= \sum_x \sum_y \left[\frac{1}{i_h(x, y)} \frac{\partial i_h(x, y)}{\partial o_{0v}} \frac{\partial i_h(x, y)}{\partial o_{1v}} + \frac{1}{i_v(x, y)} \frac{\partial i_v(x, y)}{\partial o_{0v}} \frac{\partial i_v(x, y)}{\partial o_{1v}} \right] \\
&= \sum_x \sum_y \left[\frac{1}{i_h(x, y)}(0) + \frac{1}{i_v(x, y)}(h(x, y))(h(x - \Delta, y)) \right] \\
&= \sum_x \sum_y \left[\frac{1}{i_v(x, y)}(h(x, y))(h(x - \Delta, y)) \right]
\end{aligned} \tag{3.56}$$

$$\begin{aligned}
J_{o_{1h}o_{1h}} &= \sum_x \sum_y \left[\frac{1}{i_h(x, y)} \left(\frac{\partial i_h(x, y)}{\partial o_{1h}} \right)^2 + \frac{1}{i_v(x, y)} \left(\frac{\partial i_v(x, y)}{\partial o_{1h}} \right)^2 \right] \\
&= \sum_x \sum_y \left[\frac{1}{i_h(x, y)}(h(x - \Delta, y))^2 + \frac{1}{i_v(x, y)}(0) \right] \\
&= \sum_x \sum_y \left[\frac{1}{i_h(x, y)}(h(x - \Delta, y))^2 \right]
\end{aligned} \tag{3.57}$$

$$\begin{aligned}
J_{o_{1h}o_{1v}} &= \sum_x \sum_y \left[\frac{1}{i_h(x, y)} \frac{\partial i_h(x, y)}{\partial o_{1h}} \frac{\partial i_h(x, y)}{\partial o_{1v}} + \frac{1}{i_v(x, y)} \frac{\partial i_v(x, y)}{\partial o_{1h}} \frac{\partial i_v(x, y)}{\partial o_{1v}} \right] \\
&= \sum_x \sum_y \left[\frac{1}{i_h(x, y)}(0) + \frac{1}{i_v(x, y)}(0) \right] \\
&= 0
\end{aligned} \tag{3.58}$$

$$\begin{aligned}
J_{o_{1v}o_{1v}} &= \sum_x \sum_y \left[\frac{1}{i_h(x,y)} \left(\frac{\partial i_h(x,y)}{\partial o_{1v}} \right)^2 + \frac{1}{i_v(x,y)} \left(\frac{\partial i_v(x,y)}{\partial o_{1v}} \right)^2 \right] \\
&= \sum_x \sum_y \left[\frac{1}{i_h(x,y)}(0) + \frac{1}{i_v(x,y)}(h(x - \Delta, y))^2 \right] \\
&= \sum_x \sum_y \left[\frac{1}{i_v(x,y)}(h(x - \Delta, y))^2 \right]. \tag{3.59}
\end{aligned}$$

3.2.5 FI Matrix and Degree of Polarization. The degree of polarization P affects the four intensities used in the image model and the calculations of the CRLBs. The value of P ranges from 0 for completely unpolarized light to 1 for completely polarized light. With $P < 1$ the resulting FI matrix is

$$J = \begin{bmatrix} J_{\Delta\Delta} & J_{\Delta o_{0h}} & J_{\Delta o_{0v}} & J_{\Delta o_{1h}} & J_{\Delta o_{1v}} \\ J_{o_{0h}\Delta} & J_{o_{0h}o_{0h}} & 0 & J_{o_{0h}o_{1h}} & 0 \\ J_{o_{0v}\Delta} & 0 & J_{o_{0v}o_{0v}} & 0 & J_{o_{0v}o_{1v}} \\ J_{o_{1h}\Delta} & J_{o_{1h}o_{0h}} & 0 & J_{o_{1h}o_{1h}} & 0 \\ J_{o_{1v}\Delta} & 0 & J_{o_{1v}o_{0v}} & 0 & J_{o_{1v}o_{1v}} \end{bmatrix}. \tag{3.60}$$

For a completely polarized image, with one point source horizontally polarized and the other vertically polarized, four more terms in the FI matrix are zero. This is due to two of the four intensity terms going to zero in the limit. For instance, let $o_{0h} = o_{1v} = 1$ and $o_{0v} = o_{1h} = 0$, then the resulting FI matrix is

$$J = \begin{bmatrix} J_{\Delta\Delta} & 0 & J_{\Delta o_{0v}} & 0 & J_{\Delta o_{1v}} \\ 0 & J_{o_{0h}o_{0h}} & 0 & J_{o_{0h}o_{1h}} & 0 \\ J_{o_{0v}\Delta} & 0 & J_{o_{0v}o_{0v}} & 0 & J_{o_{0v}o_{1v}} \\ 0 & J_{o_{1h}o_{0h}} & 0 & J_{o_{1h}o_{1h}} & 0 \\ J_{o_{1v}\Delta} & 0 & J_{o_{1v}o_{0v}} & 0 & J_{o_{1v}o_{1v}} \end{bmatrix}. \tag{3.61}$$

3.2.6 Cramer-R o Lower Bound of Polarimeter. Just like the base case, the CRLBs are found by inverting J.

$$J^{ij} = J^{-1} = \begin{bmatrix} \sigma_{\Delta}^2 & J^{\Delta o_{0h}} & J^{\Delta o_{0v}} & J^{\Delta o_{1h}} & J^{\Delta o_{1v}} \\ J^{o_{0h}\Delta} & \sigma_{o_{0h}}^2 & J^{o_{0h}o_{0v}} & J^{o_{0h}o_{1h}} & J^{o_{0h}o_{1v}} \\ J^{o_{0v}\Delta} & J^{o_{0v}o_{0h}} & \sigma_{o_{0v}}^2 & J^{o_{0v}o_{1h}} & J^{o_{0v}o_{1v}} \\ J^{o_{1h}\Delta} & J^{o_{1h}o_{0h}} & J^{o_{1h}o_{0v}} & \sigma_{o_{1h}}^2 & J^{o_{1h}o_{1v}} \\ J^{o_{1v}\Delta} & J^{o_{1v}o_{0h}} & J^{o_{1v}o_{0v}} & J^{o_{1v}o_{1h}} & \sigma_{o_{1v}}^2 \end{bmatrix} \quad (3.62)$$

or alternatively,

$$\sigma_{\Delta}^2 = \det \begin{bmatrix} 1 & 0 & 0 & 0 & 0 \\ 0 & J_{o_{0h}o_{0h}} & 0 & J_{o_{0h}o_{1h}} & 0 \\ 0 & 0 & J_{o_{0v}o_{0v}} & 0 & J_{o_{0v}o_{1v}} \\ 0 & J_{o_{1h}o_{0h}} & 0 & J_{o_{1h}o_{1h}} & 0 \\ 0 & 0 & J_{o_{1v}o_{0v}} & 0 & J_{o_{1v}o_{1v}} \end{bmatrix} \cdot \frac{1}{\det[J]}. \quad (3.63)$$

3.2.7 Analysis. Due to the cumbersome mathematics involved with a direct comparison between the two cases, a Matlab® analysis is developed and the results used to evaluate any performance differences. In order to evaluate the FI matrix a generic telescope with an aperture size of one meter and no central obscuration is used to simulate viewing the two point sources. Finally, some possible extensions of this analysis are proposed. For the polarimeter images, the effect of a polarizing beam splitter is modeled. The spacing in the detector plane is $1/N$ where N is the number of pixels along the side of the square detector array. For the analysis in this paper $N = 256$. Another necessity involves the use of a pseudo-inverse technique to invert the FI matrix.

Figure 3.1 shows a graphical view of the simulation during operation with a Δ of 20 pixels separating the two point sources. The point sources have been made larger in order to be visible in the figure, but during the actual analysis they are reduced to

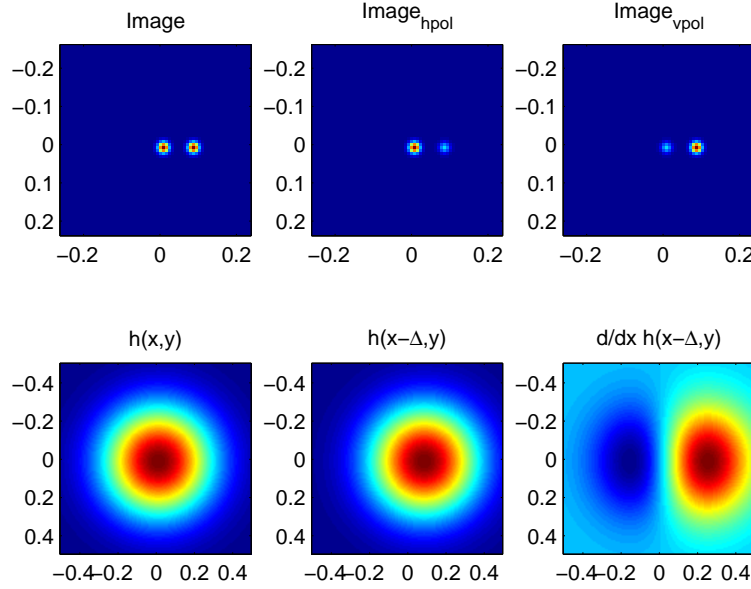


Figure 3.1: Visualization of Running Simulation.

a standard deviation for the Gaussian of approximately one pixel width to simulate the delta function. The plots of the bound calculated for Δ are shown in Figure 3.2 as the polarization is varied.

For the particular run shown, the base case value for σ_Δ is 0.07 while the results for the bound with $p = 1$ is $\sigma_\Delta = 0.035$. Therefore, under ideal conditions, the bound for two oppositely polarized sources is approximately 50% of the bound for the base case.

3.2.8 Transmission and Reflection Efficiency. A quick sampling of polarizing beam splitters showed general transmission and reflection efficiencies of better than 95 and 99%, respectively. These values are added into the modeling as efficiency parameters with the result that the bound increases slightly. Using more realistic transmission and reflection efficiencies results in an approximately 4% increase in the bound.

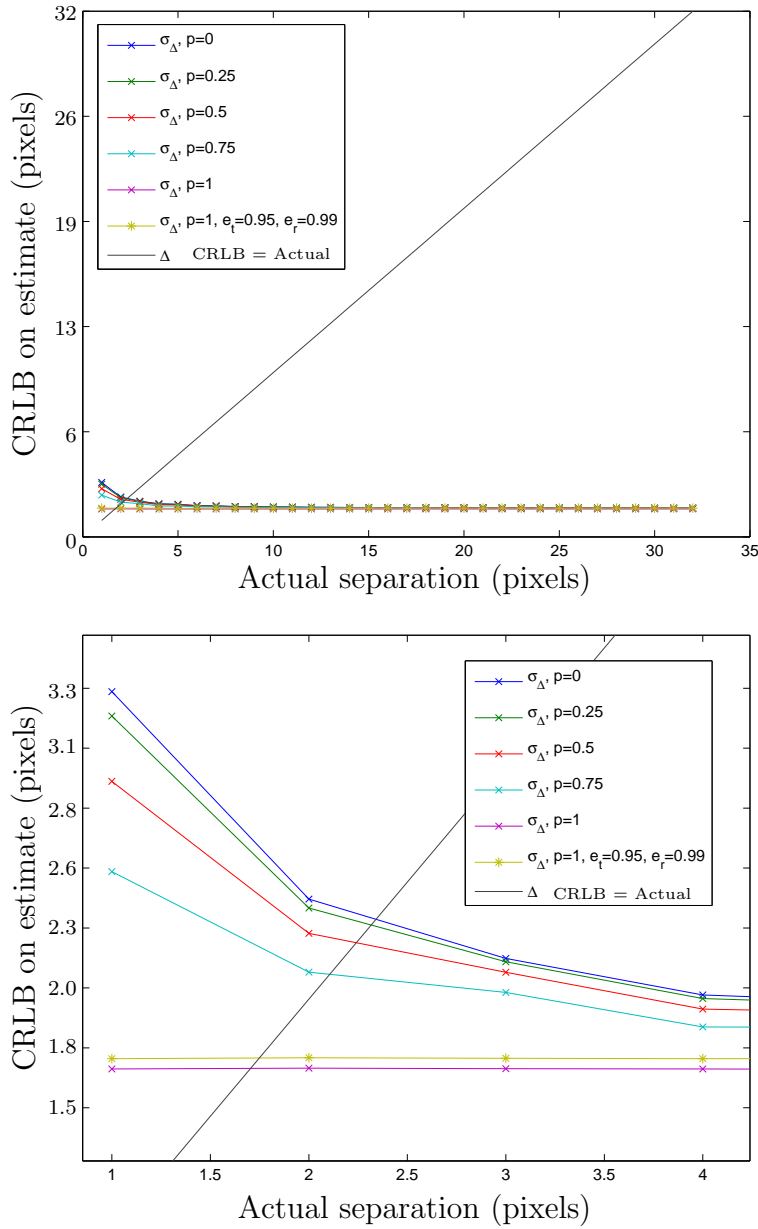


Figure 3.2: CRLB on estimation of pixel separation versus actual pixel separation.

The results of this experiment show that the resolution of two point sources is doubled when the sources are polarized 90 degrees from each other. The performance degrades as the degree of polarization decreases from 1 to 0. At $p = 0$ the images collected are completely unpolarized and the resulting bound is the same as for the base case of a single image. For realistic efficiencies for the PBS, the resulting bound

for unpolarized sources is approximately three percent lower than the base case. The decrease in the bound or increase in resolution is directly tied to the amount of polarization of the source imaged. Therefore, potential does exist to improve resolution through the development of algorithms that can make use of polarization data from captured images.

3.3 Spatial Resolution Bound with Atmospheric Turbulence

The following section extends the two channel polarimeter case to include the effects of atmospheric distortion. Similar to the previous development, two point sources comprise the image modeled. The parameters are expanded to include the individual Zernike coefficient parameters. The scenario still assumes a perfect PBS to produce the two images. Thus the parameters estimated are the amplitudes of the two point sources (o_{0h}, o_{0v}, o_{1h} and o_{1v}), the separation distance (Δ), and a set of Zernike parameters ($a_2, a_3, \dots, a_{n-1}, a_n$). The average CRLBs are then produced from the averaging of multiple instantiations of the FI matrix developed from the image model and then inverting it.

3.3.1 Image Model. The PMF used in Equation 3.31 is extended to include the atmospheric turbulence model

$$PMF_{(\Delta, o_{0h}, o_{0v}, o_{1h}, o_{1v}, a_2, a_3, \dots, a_{n-1}, a_n)} = \prod_x \prod_y \left(\frac{i_h(x, y; \alpha)^{d_h(x, y)} e^{-i_h(x, y; \alpha)}}{d_h(x, y)!} \right) \cdot \left(\frac{i_v(x, y; \alpha)^{d_v(x, y)} e^{-i_v(x, y; \alpha)}}{d_v(x, y)!} \right) \quad (3.64)$$

The image definitions for notation purposes arbitrarily define one image as the horizontally (h) polarized image and the other as the vertically (v) polarized image. The

individual images are thus defined, similarly to the base case, as

$$\begin{aligned}
& i(x, y; \alpha) \\
&= i_h(x, y; \alpha) + i_v(x, y; \alpha) \\
&= \sum_z \sum_w h(x - z, y - w; \alpha) ((o_{0h} + o_{0v}) \delta(z, w) + (o_{1h} + o_{1v}) \delta(z - \Delta, w))
\end{aligned} \tag{3.65}$$

where $h(x, y; \alpha)$ is the psf conditioned on the turbulence.

3.3.2 The Point Spread Function. To account for atmospheric turbulence and the effect of the imaging system in a closer approximation to reality a more accurate model of the psf than that presented in Section 3.1.1 is required. With the assumption of an abberation free imaging system, the only contribution to the psf is the pupil itself. When the point source illumination is sufficiently far away the field arrives at the aperture as a plane wave. Under these conditions the image of the point source is the Fourier transform of the field at the aperture masked by the pupil function and multiplied by the wave abberation function caused by the atmosphere. This yields the psf

$$\begin{aligned}
& h(x, y; \alpha) \\
&= \left| \mathcal{F} \left\{ P(f_x, f_y) \exp \left[j \sum_n a_n \phi_n(f_x, f_y) \right] \right\} \right|^2 \\
&= \left| \int \int P(f_x, f_y) \exp \left[j \sum_n a_n \phi_n(f_x, f_y) \right] \cdot \exp [-j2\pi(f_x x + f_y y)] df_x df_y \right|^2
\end{aligned} \tag{3.66}$$

and the psf for the shifted point is

$$\begin{aligned}
& h(x - \Delta, y; \alpha) \\
&= \left| \mathcal{F} \left\{ P(f_x, f_y) \exp \left[j \sum_n a_n \phi_n(f_x, f_y) \right] \right\} \right|^2 \\
&= \left| \int \int P(f_x, f_y) \exp \left[j \sum_n a_n \phi_n(f_x, f_y) \right] \cdot \exp [-j2\pi(f_x(x - \Delta) + f_y y)] df_x df_y \right|^2 \\
&= \left| \int \int P(f_x, f_y) \exp \left[j \sum_n a_n \phi_n(f_x, f_y) \right] \right. \\
&\quad \left. \cdot \exp [-j2\pi(f_x x + f_y y)] \exp[j2\pi f_x \Delta] df_x df_y \right|^2. \tag{3.67}
\end{aligned}$$

Thus $h(x - \Delta, y; \alpha)$ is equal to $h(x, y; \alpha)$ shifted by Δ using the Fourier transform shift theorem.

3.3.3 Log-likelihood Function. The log-likelihood function for the dual polarity case is found by taking the log of the PMF as shown in Eqn. 3.64. It is a function of all the parameters estimated in the model.

$$\begin{aligned}
& \mathbf{L}(\Delta, o_{0h}, o_{0v}, o_{1h}, o_{1v}, a_2, a_3, \dots, a_{n-1}, a_n) = \ln(PMF) \\
& \approx \sum_x \sum_y [d_h(x, y) \ln(i_h(x, y; \alpha)) - i_h(x, y; \alpha) \\
& \quad + d_v(x, y) \ln(i_v(x, y; \alpha)) - i_v(x, y; \alpha)] \tag{3.68}
\end{aligned}$$

3.3.4 Polarimeter Fisher Information Matrix and CRLB. The Fisher information matrix is composed of the expected values of the partial derivatives of the log-likelihood function [45]. The individual elements in the FI matrix are

$$\begin{aligned}
J_{ij} &= E \left[-E \left[\frac{\partial^2 \mathbf{L}(\Delta, o_{0h}, o_{0v}, o_{1h}, o_{1v}, a_2, a_3, \dots, a_{n-1}, a_n)}{\partial L_i \partial L_j} \right] | \alpha \right] \\
&= E \left[\sum_x \sum_y \left[\frac{1}{i_h(x, y; \alpha)} \frac{\partial i_h(x, y; \alpha)}{\partial L_i} \frac{\partial i_h(x, y; \alpha)}{\partial L_j} \right. \right. \\
&\quad \left. \left. + \frac{1}{i_v(x, y; \alpha)} \frac{\partial i_v(x, y; \alpha)}{\partial L_i} \frac{\partial i_v(x, y; \alpha)}{\partial L_j} \right] \right]. \tag{3.69}
\end{aligned}$$

The resulting FI matrix is shown in Equation 3.70.

$$J = \begin{bmatrix} J_{\Delta\Delta} & J_{\Delta\infty_k} & J_{\Delta\infty_0} & J_{\Delta\infty_1} & J_{\Delta\infty_2} & J_{\Delta\infty_{n-1}} & J_{\Delta\infty_n} \\ J_{\infty_k\Delta} & J_{\infty_k\infty_k} & J_{\infty_k\infty_0} & J_{\infty_k\infty_1} & J_{\infty_k\infty_2} & J_{\infty_k\infty_{n-1}} & J_{\infty_k\infty_n} \\ J_{\infty_0\Delta} & J_{\infty_0\infty_k} & J_{\infty_0\infty_0} & J_{\infty_0\infty_1} & J_{\infty_0\infty_2} & J_{\infty_0\infty_{n-1}} & J_{\infty_0\infty_n} \\ J_{\infty_1\Delta} & J_{\infty_1\infty_k} & J_{\infty_1\infty_0} & J_{\infty_1\infty_1} & J_{\infty_1\infty_2} & \dots & J_{\infty_1\infty_n} \\ J_{\infty_2\Delta} & J_{\infty_2\infty_k} & J_{\infty_2\infty_0} & J_{\infty_2\infty_1} & J_{\infty_2\infty_2} & J_{\infty_2\infty_{n-1}} & J_{\infty_2\infty_n} \\ J_{\infty_{n-1}\Delta} & J_{\infty_{n-1}\infty_k} & J_{\infty_{n-1}\infty_0} & J_{\infty_{n-1}\infty_1} & J_{\infty_{n-1}\infty_2} & J_{\infty_{n-1}\infty_{n-1}} & J_{\infty_{n-1}\infty_n} \\ J_{\infty_n\Delta} & J_{\infty_n\infty_k} & J_{\infty_n\infty_0} & J_{\infty_n\infty_1} & J_{\infty_n\infty_2} & J_{\infty_n\infty_{n-1}} & J_{\infty_n\infty_n} \end{bmatrix} \quad (3.70)$$

The Zernike polynomials are an orthogonal basis set, therefore the cross terms are zero and the FI matrix simplifies to Equation 3.71.

$$J = \begin{bmatrix} J_{\Delta\Delta} & J_{\Delta\alpha_0k} & J_{\Delta\alpha_0v} & J_{\Delta\alpha_1k} & J_{\Delta\alpha_1v} & J_{\Delta\alpha_2} & J_{\Delta\alpha_{n-1}} & J_{\Delta\alpha_n} \\ J_{\alpha_0k\Delta} & J_{\alpha_0k\alpha_0k} & J_{\alpha_0k\alpha_0v} & J_{\alpha_0k\alpha_1k} & J_{\alpha_0k\alpha_1v} & J_{\alpha_0k\alpha_2} & J_{\alpha_0k\alpha_{n-1}} & J_{\alpha_0k\alpha_n} \\ J_{\alpha_0v\Delta} & J_{\alpha_0v\alpha_0k} & J_{\alpha_0v\alpha_0v} & J_{\alpha_0v\alpha_1k} & J_{\alpha_0v\alpha_1v} & J_{\alpha_0v\alpha_2} & \dots & J_{\alpha_0v\alpha_{n-1}} \\ J_{\alpha_1k\Delta} & J_{\alpha_1k\alpha_0k} & J_{\alpha_1k\alpha_0v} & J_{\alpha_1k\alpha_1k} & J_{\alpha_1k\alpha_1v} & J_{\alpha_1k\alpha_2} & J_{\alpha_1k\alpha_{n-1}} & J_{\alpha_1k\alpha_n} \\ J_{\alpha_1v\Delta} & J_{\alpha_1v\alpha_0k} & J_{\alpha_1v\alpha_0v} & J_{\alpha_1v\alpha_1k} & J_{\alpha_1v\alpha_1v} & J_{\alpha_1v\alpha_2} & J_{\alpha_1v\alpha_{n-1}} & J_{\alpha_1v\alpha_n} \\ J_{\alpha_1\Delta} & J_{\alpha_1\alpha_0k} & J_{\alpha_1\alpha_0v} & J_{\alpha_1\alpha_1k} & J_{\alpha_1\alpha_1v} & J_{\alpha_1\alpha_2} & 0 & 0 \\ J_{\alpha_2\Delta} & J_{\alpha_2\alpha_0k} & J_{\alpha_2\alpha_0v} & J_{\alpha_2\alpha_1k} & J_{\alpha_2\alpha_1v} & 0 & J_{\alpha_2\alpha_2} & 0 \\ & & \vdots & & & & \ddots & \\ J_{\alpha_{n-1}\Delta} & J_{\alpha_{n-1}\alpha_0k} & J_{\alpha_{n-1}\alpha_0v} & J_{\alpha_{n-1}\alpha_1k} & J_{\alpha_{n-1}\alpha_1v} & 0 & 0 & J_{\alpha_{n-1}\alpha_{n-1}} \\ J_{\alpha_n\Delta} & J_{\alpha_n\alpha_0k} & J_{\alpha_n\alpha_0v} & J_{\alpha_n\alpha_1k} & J_{\alpha_n\alpha_1v} & 0 & 0 & 0 \end{bmatrix} \quad (3.71)$$

3.3.5 Polarimeter Image Derivatives.

image with respect to the parameters estimated are

$$\frac{\partial i_n(x, y; \alpha)}{\partial \Delta} = \frac{\partial}{\partial \Delta} \sum_z \sum_w h(x - z, y - w; \alpha) (o_{0n}\delta(x, y) + o_{1n}\delta(x - \Delta, y))$$

$$\begin{aligned}
&= \frac{\partial}{\partial \Delta} \sum_z \sum_w h(x-z, y-w; \alpha) o_{1n} \delta(x-\Delta, y) \\
&= o_{1n} \frac{\partial}{\partial \Delta} h(x-\Delta, y; \alpha)
\end{aligned} \tag{3.72}$$

$$\begin{aligned}
\frac{\partial i_h(x, y; \alpha)}{\partial o_{0h}} &= \frac{\partial}{\partial o_{0h}} \sum_z \sum_w h(x-z, y-w; \alpha) (o_{0h} \delta(x, y) + o_{1h} \delta(x-\Delta, y)) \\
&= \frac{\partial}{\partial o_{0h}} [o_{0h} h(x, y; \alpha) + o_{1h} h(x-\Delta, y; \alpha)] \\
&= h(x, y; \alpha)
\end{aligned} \tag{3.73}$$

$$\frac{\partial i_h(x, y; \alpha)}{\partial o_{0v}} = 0 \tag{3.74}$$

$$\begin{aligned}
\frac{\partial i_h(x, y; \alpha)}{\partial o_{1h}} &= \frac{\partial}{\partial o_{1h}} \sum_z \sum_w h(x-z, y-w; \alpha) (o_{0h} \delta(x, y) + o_{1h} \delta(x-\Delta, y)) \\
&= \frac{\partial}{\partial o_{1h}} [o_{0h} h(x, y; \alpha) + o_{1h} h(x-\Delta, y; \alpha)] \\
&= h(x-\Delta, y; \alpha)
\end{aligned} \tag{3.75}$$

$$\frac{\partial i_h(x, y; \alpha)}{\partial o_{1v}} = 0 \tag{3.76}$$

$$\frac{\partial i_v(x, y; \alpha)}{\partial o_{0h}} = 0 \tag{3.77}$$

$$\frac{\partial i_v(x, y; \alpha)}{\partial o_{0v}} = h(x, y; \alpha) \tag{3.78}$$

$$\frac{\partial i_v(x, y; \alpha)}{\partial o_{1h}} = 0 \tag{3.79}$$

$$\frac{\partial i_v(x, y; \alpha)}{\partial o_{1v}} = h(x-\Delta, y; \alpha) \tag{3.80}$$

$$\begin{aligned}
\frac{\partial i_h(x, y; \alpha)}{\partial a_n} &= \frac{\partial}{\partial a_n} \sum_z \sum_w h(x - z, y - w; \alpha) (o_{0h}\delta(x, y) + o_{1h}\delta(x - \Delta, y)) \\
&= \frac{\partial}{\partial a_n} [o_{0h}h(x, y; \alpha) + o_{1h}h(x - \Delta, y; \alpha)] \\
&= o_{0h} \frac{\partial}{\partial a_n} h(x, y; \alpha) + o_{1h} \frac{\partial}{\partial a_n} h(x - \Delta, y; \alpha)
\end{aligned} \tag{3.81}$$

$$\begin{aligned}
\frac{\partial i_v(x, y; \alpha)}{\partial a_n} &= \frac{\partial}{\partial a_n} \sum_z \sum_w h(x - z, y - w; \alpha) (o_{0v}\delta(x, y) + o_{1v}\delta(x - \Delta, y)) \\
&= \frac{\partial}{\partial a_n} [o_{0v}h(x, y; \alpha) + o_{1v}h(x - \Delta, y; \alpha)] \\
&= o_{0v} \frac{\partial}{\partial a_n} h(x, y; \alpha) + o_{1v} \frac{\partial}{\partial a_n} h(x - \Delta, y; \alpha)
\end{aligned} \tag{3.82}$$

3.3.6 Individual FI Elements for Polarimeter. The individual elements of the FI matrix J are calculated using the image derivatives of the previous section and are:

$$\begin{aligned}
J_{\Delta\Delta} &= \sum_x \sum_y \left[\frac{1}{i_h(x, y)} \frac{\partial i_h(x, y; \alpha)}{\partial \Delta} \frac{\partial i_h(x, y; \alpha)}{\partial \Delta} + \frac{1}{i_v(x, y; \alpha)} \frac{\partial i_v(x, y; \alpha)}{\partial \Delta} \frac{\partial i_v(x, y; \alpha)}{\partial \Delta} \right] \\
&= \sum_x \sum_y \left[\frac{1}{i_h(x, y; \alpha)} \left(\frac{\partial i_h(x, y; \alpha)}{\partial \Delta} \right)^2 + \frac{1}{i_v(x, y; \alpha)} \left(\frac{\partial i_v(x, y; \alpha)}{\partial \Delta} \right)^2 \right] \\
&= \sum_x \sum_y \left[\frac{1}{i_h(x, y; \alpha)} (o_{1h} \frac{\partial}{\partial \Delta} h(x - \Delta, y; \alpha))^2 \right. \\
&\quad \left. + \frac{1}{i_v(x, y; \alpha)} (o_{1v} \frac{\partial}{\partial \Delta} h(x - \Delta, y; \alpha))^2 \right] \\
&= \sum_x \sum_y \left[\frac{o_{1h}^2}{i_h(x, y; \alpha)} \left(\frac{\partial}{\partial \Delta} h(x - \Delta, y; \alpha) \right)^2 \right. \\
&\quad \left. + \frac{o_{1v}^2}{i_v(x, y; \alpha)} \left(\frac{\partial}{\partial \Delta} h(x - \Delta, y; \alpha) \right)^2 \right]
\end{aligned} \tag{3.83}$$

$$\begin{aligned}
J_{\Delta o_{0h}} &= \sum_x \sum_y \left[\frac{1}{i_h(x, y; \alpha)} \frac{\partial i_h(x, y; \alpha)}{\partial \Delta} \frac{\partial i_h(x, y; \alpha)}{\partial o_{0h}} + \frac{1}{i_v(x, y; \alpha)} \frac{\partial i_v(x, y; \alpha)}{\partial \Delta} \frac{\partial i_v(x, y; \alpha)}{\partial o_{0h}} \right] \\
&= \sum_x \sum_y \left[\frac{1}{i_h(x, y; \alpha)} (o_{1h} \frac{\partial}{\partial \Delta} h(x - \Delta, y; \alpha)) (h(x, y; \alpha)) \right. \\
&\quad \left. + \frac{1}{i_v(x, y; \alpha)} (o_{1v} \frac{\partial}{\partial \Delta} h(x - \Delta, y; \alpha)) (0) \right] \\
&= \sum_x \sum_y \left[\frac{o_{1h}}{i_h(x, y; \alpha)} (\frac{\partial}{\partial \Delta} h(x - \Delta, y; \alpha)) (h(x, y; \alpha)) \right]
\end{aligned} \tag{3.84}$$

$$\begin{aligned}
J_{\Delta o_{0v}} &= \sum_x \sum_y \left[\frac{1}{i_h(x, y; \alpha)} \frac{\partial i_h(x, y; \alpha)}{\partial \Delta} \frac{\partial i_h(x, y; \alpha)}{\partial o_{0v}} + \frac{1}{i_v(x, y; \alpha)} \frac{\partial i_v(x, y; \alpha)}{\partial \Delta} \frac{\partial i_v(x, y; \alpha)}{\partial o_{0v}} \right] \\
&= \sum_x \sum_y \left[\frac{1}{i_h(x, y; \alpha)} (o_{1h} \frac{\partial}{\partial \Delta} h(x - \Delta, y; \alpha)) (0) \right. \\
&\quad \left. + \frac{1}{i_v(x, y; \alpha)} (o_{1v} \frac{\partial}{\partial \Delta} h(x - \Delta, y; \alpha)) (h(x, y; \alpha)) \right] \\
&= \sum_x \sum_y \left[\frac{o_{1v}}{i_v(x, y; \alpha)} (\frac{\partial}{\partial \Delta} h(x - \Delta, y; \alpha)) (h(x, y; \alpha)) \right]
\end{aligned} \tag{3.85}$$

$$\begin{aligned}
J_{\Delta o_{1h}} &= \sum_x \sum_y \left[\frac{1}{i_h(x, y; \alpha)} \frac{\partial i_h(x, y; \alpha)}{\partial \Delta} \frac{\partial i_h(x, y; \alpha)}{\partial o_{1h}} + \frac{1}{i_v(x, y; \alpha)} \frac{\partial i_v(x, y; \alpha)}{\partial \Delta} \frac{\partial i_v(x, y; \alpha)}{\partial o_{1h}} \right] \\
&= \sum_x \sum_y \left[\frac{1}{i_h(x, y; \alpha)} (o_{1h} \frac{\partial}{\partial \Delta} h(x - \Delta, y; \alpha)) (h(x - \Delta, y; \alpha)) \right. \\
&\quad \left. + \frac{1}{i_v(x, y; \alpha)} (o_{1v} \frac{\partial}{\partial \Delta} h(x - \Delta, y; \alpha)) (0) \right] \\
&= \sum_x \sum_y \left[\frac{o_{1h}}{i_h(x, y; \alpha)} (\frac{\partial}{\partial \Delta} h(x - \Delta, y; \alpha)) (h(x - \Delta, y; \alpha)) \right]
\end{aligned} \tag{3.86}$$

$$\begin{aligned}
J_{\Delta o_{1v}} &= \sum_x \sum_y \left[\frac{1}{i_h(x, y; \alpha)} \frac{\partial i_h(x, y; \alpha)}{\partial \Delta} \frac{\partial i_h(x, y; \alpha)}{\partial o_{1v}} + \frac{1}{i_v(x, y; \alpha)} \frac{\partial i_v(x, y; \alpha)}{\partial \Delta} \frac{\partial i_v(x, y; \alpha)}{\partial o_{1v}} \right] \\
&= \sum_x \sum_y \left[\frac{1}{i_h(x, y; \alpha)} (o_{1h} \frac{\partial}{\partial \Delta} h(x - \Delta, y; \alpha)) (0) \right. \\
&\quad \left. + \frac{1}{i_v(x, y; \alpha)} (o_{1v} \frac{\partial}{\partial \Delta} h(x - \Delta, y; \alpha)) (h(x - \Delta, y; \alpha)) \right] \\
&= \sum_x \sum_y \left[\frac{o_{1v}}{i_v(x, y; \alpha)} (\frac{\partial}{\partial \Delta} h(x - \Delta, y; \alpha)) (h(x - \Delta, y; \alpha)) \right]
\end{aligned} \tag{3.87}$$

$$\begin{aligned}
J_{\Delta a_n} &= \sum_x \sum_y \left[\frac{1}{i_h(x, y; \alpha)} \frac{\partial i_h(x, y; \alpha)}{\partial \Delta} \frac{\partial i_h(x, y; \alpha)}{\partial a_n} + \frac{1}{i_v(x, y; \alpha)} \frac{\partial i_v(x, y; \alpha)}{\partial \Delta} \frac{\partial i_v(x, y; \alpha)}{\partial a_n} \right] \\
&= \sum_x \sum_y \left[\frac{1}{i_h(x, y; \alpha)} (o_{1h} \frac{\partial}{\partial \Delta} h(x - \Delta, y; \alpha)) \right. \\
&\quad \cdot (o_{0h} \frac{\partial}{\partial a_n} h(x, y; \alpha) + o_{1h} \frac{\partial}{\partial a_n} h(x - \Delta, y; \alpha)) \\
&\quad + \sum_x \sum_y \left[\frac{1}{i_v(x, y; \alpha)} (o_{1v} \frac{\partial}{\partial \Delta} h(x - \Delta, y; \alpha)) \right. \\
&\quad \cdot (o_{0v} \frac{\partial}{\partial a_n} h(x, y; \alpha) + o_{1v} \frac{\partial}{\partial a_n} h(x - \Delta, y; \alpha)) \left. \right] \tag{3.88}
\end{aligned}$$

$$\begin{aligned}
J_{o_{0h} o_{0h}} &= \sum_x \sum_y \left[\frac{1}{i_h(x, y; \alpha)} (\frac{\partial i_h(x, y; \alpha)}{\partial o_{0h}})^2 + \frac{1}{i_v(x, y; \alpha)} (\frac{\partial i_v(x, y; \alpha)}{\partial o_{0h}})^2 \right] \\
&= \sum_x \sum_y \left[\frac{1}{i_h(x, y; \alpha)} (h(x, y; \alpha))^2 + \frac{1}{i_v(x, y; \alpha)} (0)^2 \right] \\
&= \sum_x \sum_y \left[\frac{1}{i_h(x, y; \alpha)} (h(x, y; \alpha))^2 \right] \tag{3.89}
\end{aligned}$$

$$\begin{aligned}
J_{o_{0h} o_{0v}} &= \sum_x \sum_y \left[\frac{1}{i_h(x, y; \alpha)} \frac{\partial i_h(x, y; \alpha)}{\partial o_{0h}} \frac{\partial i_h(x, y; \alpha)}{\partial o_{0v}} + \frac{1}{i_v(x, y; \alpha)} \frac{\partial i_v(x, y; \alpha)}{\partial o_{0h}} \frac{\partial i_v(x, y; \alpha)}{\partial o_{0v}} \right] \\
&= \sum_x \sum_y \left[\frac{1}{i_h(x, y; \alpha)} (0) + \frac{1}{i_v(x, y; \alpha)} (0) \right] \\
&= 0 \tag{3.90}
\end{aligned}$$

$$\begin{aligned}
J_{o_{0h} o_{1h}} &= \sum_x \sum_y \left[\frac{1}{i_h(x, y; \alpha)} \frac{\partial i_h(x, y; \alpha)}{\partial o_{0h}} \frac{\partial i_h(x, y; \alpha)}{\partial o_{1h}} + \frac{1}{i_v(x, y; \alpha)} \frac{\partial i_v(x, y; \alpha)}{\partial o_{0h}} \frac{\partial i_v(x, y; \alpha)}{\partial o_{1h}} \right] \\
&= \sum_x \sum_y \left[\frac{1}{i_h(x, y; \alpha)} (h(x, y; \alpha))(h(x - \Delta, y)) + \frac{1}{i_v(x, y; \alpha)} (0) \right] \\
&= \sum_x \sum_y \left[\frac{1}{i_h(x, y; \alpha)} (h(x, y; \alpha))(h(x - \Delta, y)) \right] \tag{3.91}
\end{aligned}$$

$$\begin{aligned}
J_{o_{0h} o_{1v}} &= \sum_x \sum_y \left[\frac{1}{i_h(x, y; \alpha)} \frac{\partial i_h(x, y; \alpha)}{\partial o_{0h}} \frac{\partial i_h(x, y; \alpha)}{\partial o_{1v}} + \frac{1}{i_v(x, y; \alpha)} \frac{\partial i_v(x, y; \alpha)}{\partial o_{0h}} \frac{\partial i_v(x, y; \alpha)}{\partial o_{1v}} \right] \\
&= \sum_x \sum_y \left[\frac{1}{i_h(x, y; \alpha)} (0) + \frac{1}{i_v(x, y; \alpha)} (0) \right] \\
&= 0 \tag{3.92}
\end{aligned}$$

$$\begin{aligned}
J_{o_{0h}a_n} &= \sum_x \sum_y \left[\frac{1}{i_h(x, y; \alpha)} \frac{\partial i_h(x, y; \alpha)}{\partial o_{0h}} \frac{\partial i_h(x, y; \alpha)}{\partial a_n} + \frac{1}{i_v(x, y; \alpha)} \frac{\partial i_v(x, y; \alpha)}{\partial o_{0h}} \frac{\partial i_v(x, y; \alpha)}{\partial a_n} \right] \\
&= \sum_x \sum_y \left[\frac{1}{i_h(x, y; \alpha)} h(x, y; \alpha) (o_{0h} \frac{\partial}{\partial a_n} h(x, y; \alpha) + o_{1h} \frac{\partial}{\partial a_n} h(x - \Delta, y; \alpha)) + 0 \right] \\
&= \sum_x \sum_y \left[\frac{1}{i_h(x, y; \alpha)} h(x, y; \alpha) (o_{0h} \frac{\partial}{\partial a_n} h(x, y; \alpha) + o_{1h} \frac{\partial}{\partial a_n} h(x - \Delta, y; \alpha)) \right] \quad (3.93)
\end{aligned}$$

$$\begin{aligned}
J_{o_{0v}o_{0v}} &= \sum_x \sum_y \left[\frac{1}{i_h(x, y; \alpha)} (\frac{\partial i_h(x, y; \alpha)}{\partial o_{0v}})^2 + \frac{1}{i_v(x, y; \alpha)} (\frac{\partial i_v(x, y; \alpha)}{\partial o_{0v}})^2 \right] \\
&= \sum_x \sum_y \left[\frac{1}{i_h(x, y; \alpha)} (0) + \frac{1}{i_v(x, y; \alpha)} (h(x, y; \alpha))^2 \right] \\
&= \sum_x \sum_y \left[\frac{1}{i_v(x, y; \alpha)} (h(x, y; \alpha))^2 \right] \quad (3.94)
\end{aligned}$$

$$\begin{aligned}
J_{o_{0v}o_{1h}} &= \sum_x \sum_y \left[\frac{1}{i_h(x, y; \alpha)} \frac{\partial i_h(x, y; \alpha)}{\partial o_{0v}} \frac{\partial i_h(x, y; \alpha)}{\partial o_{1h}} + \frac{1}{i_v(x, y; \alpha)} \frac{\partial i_v(x, y; \alpha)}{\partial o_{0v}} \frac{\partial i_v(x, y; \alpha)}{\partial o_{1h}} \right] \\
&= \sum_x \sum_y \left[\frac{1}{i_h(x, y; \alpha)} (0) + \frac{1}{i_v(x, y; \alpha)} (0) \right] \\
&= 0 \quad (3.95)
\end{aligned}$$

$$\begin{aligned}
J_{o_{0v}o_{1v}} &= \sum_x \sum_y \left[\frac{1}{i_h(x, y; \alpha)} \frac{\partial i_h(x, y; \alpha)}{\partial o_{0v}} \frac{\partial i_h(x, y; \alpha)}{\partial o_{1v}} + \frac{1}{i_v(x, y; \alpha)} \frac{\partial i_v(x, y; \alpha)}{\partial o_{0v}} \frac{\partial i_v(x, y; \alpha)}{\partial o_{1v}} \right] \\
&= \sum_x \sum_y \left[\frac{1}{i_h(x, y; \alpha)} (0) + \frac{1}{i_v(x, y; \alpha)} (h(x, y; \alpha))(h(x - \Delta, y)) \right] \\
&= \sum_x \sum_y \left[\frac{1}{i_v(x, y; \alpha)} (h(x, y; \alpha))(h(x - \Delta, y)) \right] \quad (3.96)
\end{aligned}$$

$$\begin{aligned}
J_{o_{0v}a_n} &= \sum_x \sum_y \left[\frac{1}{i_h(x, y; \alpha)} \frac{\partial i_h(x, y; \alpha)}{\partial o_{0v}} \frac{\partial i_h(x, y; \alpha)}{\partial a_n} + \frac{1}{i_v(x, y; \alpha)} \frac{\partial i_v(x, y; \alpha)}{\partial o_{0v}} \frac{\partial i_v(x, y; \alpha)}{\partial a_n} \right] \\
&= \sum_x \sum_y \left[0 + \frac{1}{i_v(x, y; \alpha)} h(x, y; \alpha) (o_{0v} \frac{\partial}{\partial a_n} h(x, y; \alpha) + o_{1v} \frac{\partial}{\partial a_n} h(x - \Delta, y; \alpha)) \right] \\
&= \sum_x \sum_y \left[\frac{1}{i_v(x, y; \alpha)} h(x, y; \alpha) (o_{0v} \frac{\partial}{\partial a_n} h(x, y; \alpha) + o_{1v} \frac{\partial}{\partial a_n} h(x - \Delta, y; \alpha)) \right] \quad (3.97)
\end{aligned}$$

$$\begin{aligned}
J_{o_{1h}o_{1h}} &= \sum_x \sum_y \left[\frac{1}{i_h(x, y; \alpha)} \left(\frac{\partial i_h(x, y; \alpha)}{\partial o_{1h}} \right)^2 + \frac{1}{i_v(x, y; \alpha)} \left(\frac{\partial i_v(x, y; \alpha)}{\partial o_{1h}} \right)^2 \right] \\
&= \sum_x \sum_y \left[\frac{1}{i_h(x, y; \alpha)} (h(x - \Delta, y))^2 + \frac{1}{i_v(x, y; \alpha)} (0) \right] \\
&= \sum_x \sum_y \left[\frac{1}{i_h(x, y; \alpha)} (h(x - \Delta, y))^2 \right]
\end{aligned} \tag{3.98}$$

$$\begin{aligned}
J_{o_{1h}o_{1v}} &= \sum_x \sum_y \left[\frac{1}{i_h(x, y; \alpha)} \frac{\partial i_h(x, y; \alpha)}{\partial o_{1h}} \frac{\partial i_h(x, y; \alpha)}{\partial o_{1v}} + \frac{1}{i_v(x, y; \alpha)} \frac{\partial i_v(x, y; \alpha)}{\partial o_{1h}} \frac{\partial i_v(x, y; \alpha)}{\partial o_{1v}} \right] \\
&= \sum_x \sum_y \left[\frac{1}{i_h(x, y; \alpha)} (0) + \frac{1}{i_v(x, y; \alpha)} (0) \right] \\
&= 0
\end{aligned} \tag{3.99}$$

$$\begin{aligned}
J_{o_{1h}a_n} &= \sum_x \sum_y \left[\frac{1}{i_h(x, y; \alpha)} \frac{\partial i_h(x, y; \alpha)}{\partial o_{1h}} \frac{\partial i_h(x, y; \alpha)}{\partial a_n} + \frac{1}{i_v(x, y; \alpha)} \frac{\partial i_v(x, y; \alpha)}{\partial o_{1h}} \frac{\partial i_v(x, y; \alpha)}{\partial a_n} \right] \\
&= \sum_x \sum_y \left[\frac{1}{i_h(x, y; \alpha)} h(x - \Delta, y; \alpha) \cdot \left(o_{0h} \frac{\partial}{\partial a_n} h(x, y; \alpha) + o_{1h} \frac{\partial}{\partial a_n} h(x - \Delta, y; \alpha) \right) \right]
\end{aligned} \tag{3.100}$$

$$\begin{aligned}
J_{o_{1v}o_{1v}} &= \sum_x \sum_y \left[\frac{1}{i_h(x, y; \alpha)} \left(\frac{\partial i_h(x, y; \alpha)}{\partial o_{1v}} \right)^2 + \frac{1}{i_v(x, y; \alpha)} \left(\frac{\partial i_v(x, y; \alpha)}{\partial o_{1v}} \right)^2 \right] \\
&= \sum_x \sum_y \left[\frac{1}{i_h(x, y; \alpha)} (0) + \frac{1}{i_v(x, y; \alpha)} (h(x - \Delta, y))^2 \right] \\
&= \sum_x \sum_y \left[\frac{1}{i_v(x, y; \alpha)} (h(x - \Delta, y))^2 \right]
\end{aligned} \tag{3.101}$$

$$\begin{aligned}
J_{o_{1v}a_n} &= \sum_x \sum_y \left[\frac{1}{i_h(x, y; \alpha)} \frac{\partial i_h(x, y; \alpha)}{\partial o_{1v}} \frac{\partial i_h(x, y; \alpha)}{\partial a_n} + \frac{1}{i_v(x, y; \alpha)} \frac{\partial i_v(x, y; \alpha)}{\partial o_{1v}} \frac{\partial i_v(x, y; \alpha)}{\partial a_n} \right] \\
&= \sum_x \sum_y \left[\frac{1}{i_v(x, y; \alpha)} h(x - \Delta, y; \alpha) \cdot \left(o_{0v} \frac{\partial}{\partial a_n} h(x, y; \alpha) + o_{1v} \frac{\partial}{\partial a_n} h(x - \Delta, y; \alpha) \right) \right]
\end{aligned} \tag{3.102}$$

$$J_{a_n a_m} = \sum_x \sum_y \left[\frac{1}{i_h(x, y; \alpha)} \frac{\partial i_h(x, y; \alpha)}{\partial a_n} \frac{\partial i_h(x, y; \alpha)}{\partial a_m} + \frac{1}{i_v(x, y; \alpha)} \frac{\partial i_v(x, y; \alpha)}{\partial a_n} \frac{\partial i_v(x, y; \alpha)}{\partial a_m} \right]$$

$$= \sum_x \sum_y \left[\frac{1}{i_h(x, y; \alpha)} \left(\frac{\partial i_h(x, y; \alpha)}{\partial a_n} \right)^2 \right. \\ \left. + \frac{1}{i_v(x, y; \alpha)} \left(\frac{\partial i_v(x, y; \alpha)}{\partial a_n} \right)^2 \right], \quad \text{if } n = m \quad (3.103)$$

$$= 0, \quad \text{if } n \neq m \quad (3.104)$$

3.3.7 Partial Derivatives of the psf. The following partial derivatives of the psf are required for calculation of the individual FI elements.

Let

$$f_1 = \int \int P(f_x, f_y) \exp \left[j \sum_n a_n \phi_n(f_x, f_y) \right] \exp [-j2\pi(f_x x + f_y y)] df_x df_y \quad (3.105)$$

then using the identity $|f|^2 = f \cdot f^*$ and letting $f_2 = f_1^*$ the psf becomes

$$h(x, y; \alpha) = f_1 \cdot f_2. \quad (3.106)$$

The partial derivative with respect to Δ is

$$\frac{\partial}{\partial \Delta} h(x - \Delta, y; \alpha) = \frac{\partial}{\partial \Delta} [f_1 \cdot f_2]. \quad (3.107)$$

Using the chain rule this becomes

$$\frac{\partial}{\partial \Delta} h(x - \Delta, y; \alpha) = f_1 \cdot \left[\frac{\partial}{\partial \Delta} f_2 \right] + \left[\frac{\partial}{\partial \Delta} f_1 \right] \cdot f_2 \quad (3.108)$$

where

$$\begin{aligned} \frac{\partial}{\partial \Delta} f_1 &= \frac{\partial}{\partial \Delta} \int \int P(f_x, f_y) \exp \left[j \sum_n a_n \phi_n(f_x, f_y) \right] \exp [-j2\pi(f_x(x - \Delta) + f_y y)] df_x df_y \\ &= \int \int P(f_x, f_y) \exp \left[j \sum_n a_n \phi_n(f_x, f_y) \right] \frac{\partial}{\partial \Delta} \exp [-j2\pi(f_x(x - \Delta) + f_y y)] df_x df_y \end{aligned}$$

$$\begin{aligned}
&= \int \int P(f_x, f_y) \exp \left[j \sum_n a_n \phi_n(f_x, f_y) \right] (j2\pi f_x) \exp [-j2\pi(f_x(x - \Delta) + f_y y)] df_x df_y \\
&= j \int \int (2\pi f_x) P(f_x, f_y) \exp \left[j \sum_n a_n \phi_n(f_x, f_y) \right] \exp [-j2\pi(f_x(x - \Delta) + f_y y)] df_x df_y
\end{aligned} \tag{3.109}$$

and

$$\begin{aligned}
\frac{\partial}{\partial \Delta} f_2 &= \frac{\partial}{\partial \Delta} \int \int P(f_x, f_y) \exp \left[-j \sum_n a_n \phi_n(f_x, f_y) \right] \exp [j2\pi(f_x(x - \Delta) + f_y y)] df_x df_y \\
&= \int \int P(f_x, f_y) \exp \left[-j \sum_n a_n \phi_n(f_x, f_y) \right] \frac{\partial}{\partial \Delta} \exp [j2\pi(f_x(x - \Delta) + f_y y)] df_x df_y \\
&= \int \int P(f_x, f_y) \exp \left[-j \sum_n a_n \phi_n(f_x, f_y) \right] (-j2\pi f_x) \\
&\quad \cdot \exp [j2\pi(f_x(x - \Delta) + f_y y)] df_x df_y \\
&= -j \int \int (2\pi f_x) P(f_x, f_y) \exp \left[-j \sum_n a_n \phi_n(f_x, f_y) \right] \\
&\quad \cdot \exp [-j2\pi(f_x(x - \Delta) + f_y y)] df_x df_y
\end{aligned} \tag{3.110}$$

$$= \left[\frac{\partial}{\partial \Delta} f_1 \right]^* \tag{3.111}$$

The partial derivatives of the psf with respect to the individual Zernike coefficients are

$$\begin{aligned}
\frac{\partial}{\partial a_n} h(x, y; \alpha) &= \frac{\partial}{\partial a_n} [f_1 \cdot f_2] \\
&= f_1 \cdot \left[\frac{\partial}{\partial a_n} f_2 \right] + \left[\frac{\partial}{\partial a_n} f_1 \right] \cdot f_2
\end{aligned} \tag{3.112}$$

where

$$\begin{aligned}
\frac{\partial}{\partial a_n} f_1 &= \frac{\partial}{\partial a_n} \int \int P(f_x, f_y) \exp \left[j \sum_n a_n \phi_n(f_x, f_y) \right] \exp [-j2\pi(f_x x + f_y y)] df_x df_y \\
&= \int \int P(f_x, f_y) \frac{\partial}{\partial a_n} \left[\exp \left[j \sum_n a_n \phi_n(f_x, f_y) \right] \right] \exp [-j2\pi(f_x x + f_y y)] df_x df_y \\
&= \int \int P(f_x, f_y) \left[(j\phi_n(f_x, f_y)) \exp \left[j \sum_n a_n \phi_n(f_x, f_y) \right] \right] \\
&\quad \cdot \exp [-j2\pi(f_x x + f_y y)] df_x df_y \\
&= j \int \int P(f_x, f_y) \phi_n(f_x, f_y) \exp \left[j \sum_n a_n \phi_n(f_x, f_y) \right] \\
&\quad \cdot \exp [-j2\pi(f_x x + f_y y)] df_x df_y,
\end{aligned} \tag{3.113}$$

$$\begin{aligned}
\frac{\partial}{\partial a_n} f_2 &= \frac{\partial}{\partial a_n} \int \int P(f_x, f_y) \exp \left[-j \sum_n a_n \phi_n(f_x, f_y) \right] \exp [j2\pi(f_x x + f_y y)] df_x df_y \\
&= \int \int P(f_x, f_y) \frac{\partial}{\partial a_n} \left[\exp \left[-j \sum_n a_n \phi_n(f_x, f_y) \right] \right] \exp [j2\pi(f_x x + f_y y)] df_x df_y \\
&= \int \int P(f_x, f_y) \left[(-j\phi_n(f_x, f_y)) \exp \left[-j \sum_n a_n \phi_n(f_x, f_y) \right] \right] \\
&\quad \cdot \exp [j2\pi(f_x x + f_y y)] df_x df_y \\
&= -j \int \int P(f_x, f_y) \phi_n(f_x, f_y) \exp \left[-j \sum_n a_n \phi_n(f_x, f_y) \right] \\
&\quad \cdot \exp [j2\pi(f_x x + f_y y)] df_x df_y \\
&= \left[\frac{\partial}{\partial a_n} f_1 \right]^*,
\end{aligned} \tag{3.114}$$

and

$$\begin{aligned}
\frac{\partial}{\partial a_n} f_1(x - \Delta) &= j \int \int P(f_x, f_y) \phi_n(f_x, f_y) \exp \left[j \sum_n a_n \phi_n(f_x, f_y) \right] \\
&\quad \cdot \exp [-j2\pi(f_x(x - \Delta) + f_y y)] df_x df_y.
\end{aligned} \tag{3.115}$$

3.3.8 CRLB. Using the previous partial derivatives, the FI matrix is filled in and the inverse is calculated. The resulting diagonal elements, shown in Equation 3.116, are the CRLBs for the parameters estimated. The primary element studied

in the following sections is the first diagonal element σ_{Δ}^2 . This is the CRLB on the estimate of the pixel separation Δ .

$$J^{-1} = \begin{bmatrix} \sigma_{\Delta}^2 & J^{\Delta_{00k}} & J^{\Delta_{00v}} & J^{\Delta_{01k}} & J^{\Delta_{01v}} & J^{\Delta_{02}} & J^{\Delta_{0n-1}} & J^{\Delta_{0n}} \\ J^{\alpha_{0k}\Delta} & \sigma_{\alpha_{0k}}^2 & J^{\alpha_{0k}\alpha_{0k}} & J^{\alpha_{0k}\alpha_{0k}} & J^{\alpha_{0k}\alpha_{0k}} & J^{\alpha_{0k}\alpha_{0k}} & J^{\alpha_{0k}\alpha_{0k}} & J^{\alpha_{0k}\alpha_{0k}} \\ J^{\alpha_{0v}\Delta} & J^{\alpha_{0v}\alpha_{0k}} \\ J^{\alpha_{1k}\Delta} & J^{\alpha_{1k}\alpha_{0k}} \\ J^{\alpha_{1v}\Delta} & J^{\alpha_{1v}\alpha_{0k}} \\ J^{\alpha_1\Delta} & J^{\alpha_1\alpha_{0k}} \\ J^{\alpha_2\Delta} & J^{\alpha_2\alpha_{0k}} \\ & \vdots & & & & & \ddots & \\ J^{\alpha_{n-1}\Delta} & J^{\alpha_{n-1}\alpha_{0k}} & J^{\alpha_{n-1}\alpha_{0k}} & J^{\alpha_{n-1}\alpha_{0k}} & J^{\alpha_{n-1}\alpha_{0k}} & J^{\alpha_{n-1}\alpha_{0k}} & 0 & 0 \\ J^{\alpha_n\Delta} & J^{\alpha_n\alpha_{0k}} & J^{\alpha_n\alpha_{0k}} & J^{\alpha_n\alpha_{0k}} & J^{\alpha_n\alpha_{0k}} & J^{\alpha_n\alpha_{0k}} & 0 & 0 \end{bmatrix} \quad (3.116)$$

3.3.9 Effect of Atmospheric Turbulence on CRLB. Using the expanded FI matrices, the average lower bound on the estimate of the pixel separation and other parameters are calculated. This is accomplished by generating a new set of

Zernike coefficients for each change in parameters. Multiple iterations are then averaged together to yield the average CRLBs for the parameters estimated. In order to compute an analytical solution, some additional parameters are required. The following parameters are used for generation of most of the graphs in this analysis:

- Aperture size of 1 meter
- Fried parameter (r_o) of 1 meter
- Focal length of 10 meters
- Object intensity of 0.1mW
- Grid size of 32 by 32 pixels
- Wavelength of 800nm

3.3.10 Normal Imaging System. This section discusses the average lower bound on the estimate of the pixel separation for a normal (i.e. non-polarimetric) sensor. The number of Zernike coefficients is varied and the impact on the average lower bound is shown in Figure 3.3.

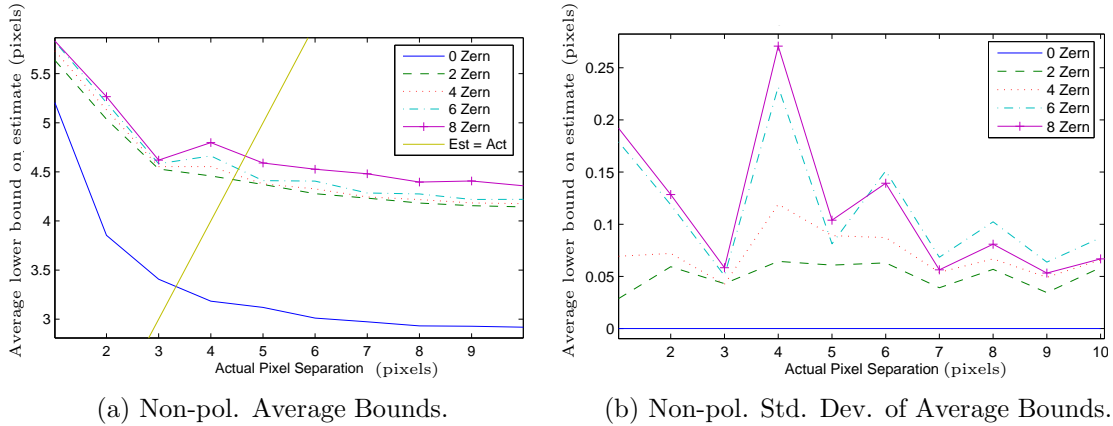


Figure 3.3: Average bound relative to pixel separation.

The primary focus of this research is on the CRLB of the estimated pixel separation of the two point sources. Figure 3.3(a) shows the average CRLB as the actual pixel separation in the model is changed. The lowest line is the basic model without

any Zernike coefficients estimated. The upper grouping of lines are for estimates when two, four, six, and eight coefficients are added to the model. Figure 3.3(b) shows the standard deviations of the data used to generate the bound plots to the left. The standard deviation for the model without any Zernike coefficients is on the bottom of the plot at values in the 10^{-14} range. Thus, introducing atmospheric turbulence into the model increases the lower bound. The bound follows a similarly shaped curve as the non-turbulent model. All plots asymptotically approach some value as the separation gets larger. The determination of that value is discussed later in this chapter.

3.3.11 Polarimeter Imaging System. Now that the behavior for the normal imaging system is known, the behavior of the polarimeter model is determined. Keeping the same parameter settings as the normal system, the polarimeter lower bound on the estimation of Δ is plotted against the actual pixel separation with the addition of various induced polarization states of the point sources.

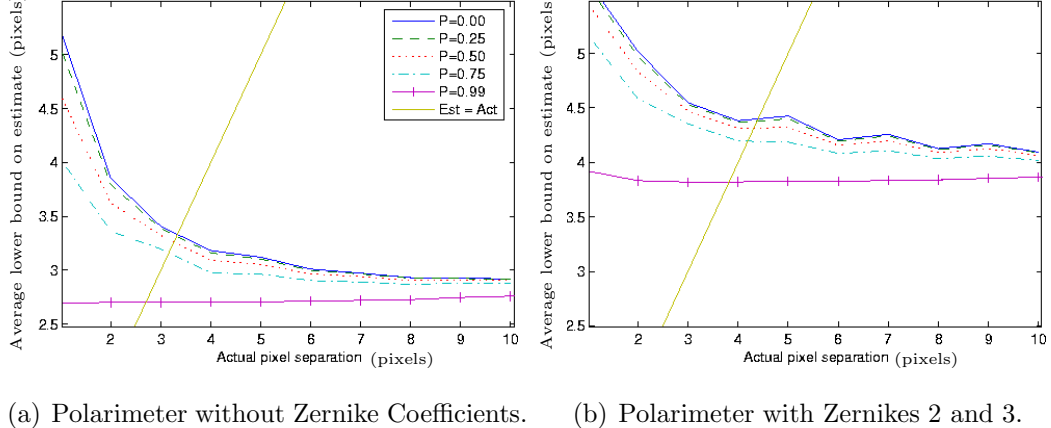


Figure 3.4: Average polarimeter bounds relative to pixel separation.

Figure 3.4(a) shows the effect of polarization on the average lower bound on the estimated pixel separation as the degree of polarization goes from 0 to close to 1. A note on the model regarding a completely polarized source is necessary here. With a degree of polarization of 1, a discontinuity is reached and data is erroneous. Therefore, a degree of polarization of 0.99 is chosen to show the average bound close

to $p = 1$. One should also note that as the degree of polarization increases, the bound flattens out until the limit on the bound is reached for estimating the location of a single point source.

In Figure 3.4(b), the estimates of the first two Zernike coefficients (piston is ignored) related to tilt are introduced. The bounds have a relative shift upward. The top line in the plot corresponds to the unpolarized source case and follows the grouping of lines seen in Figure 3.3(a) for the normal imaging system. As the degree of polarization increases, the average lower bound decreases. The limit is approached as the degree of polarization approaches 1. Based on a definition of minimum resolving power for the system located at the point where its estimate equals the actual, Figure 3.4 shows that polarization effects can improve resolving power. For this particular set of parameters, the improvement is approximately 20%.

3.3.12 Other System Parameters. The effects of other parameters on the spatial frequency lower bound and other estimates are explored in this section. First, the effect the number of Zernike coefficients estimated have on the spatial frequency bound and on source intensity estimates are explored. Next, all parameters are fixed and just the source intensities are varied to explore its effect on the bound. Finally, a very brief look is taken at the effect of the Fried parameter on the model to see how increasing the turbulence in the model affects the results. It is fixed at eight times smaller than the aperture and the impact of partial compensation by an AO system is explored.

An understanding of how the model changes as the number of Zernike coefficients estimated increases is explored. It is noted that the average lower bound on the estimate of Δ increases as the number of coefficients increases. In order to quantify the change, all the parameters are fixed. The average pixel separation bound on estimation is then calculated at an actual pixel separation of five pixels. Due to the fairly quick execution time, an arbitrarily large set of two hundred randomly generated Zernike coefficients were used to generate the plots shown. They are calculated for

both the normal imaging system and the polarimeter at each polarization setting for every additional Zernike coefficient up to 85.

Figure 3.5(a) plots the result for the normal imaging system. Figure 3.5(b) plots the results for the polarimeter for each of the polarization settings. As the degree of polarization increases the plot lines decrease but retain similar shapes. The plot for the polarization line close to 1 gets more erratic as the degree of polarization gets closer to 1. This is due to the discontinuity in the model when the degree of polarization is 1. All of the lines are similar in shape to the plot in Figure 3.5(c). This is the cumulative sum of the expected values for the covariance of the Zernike coefficients.

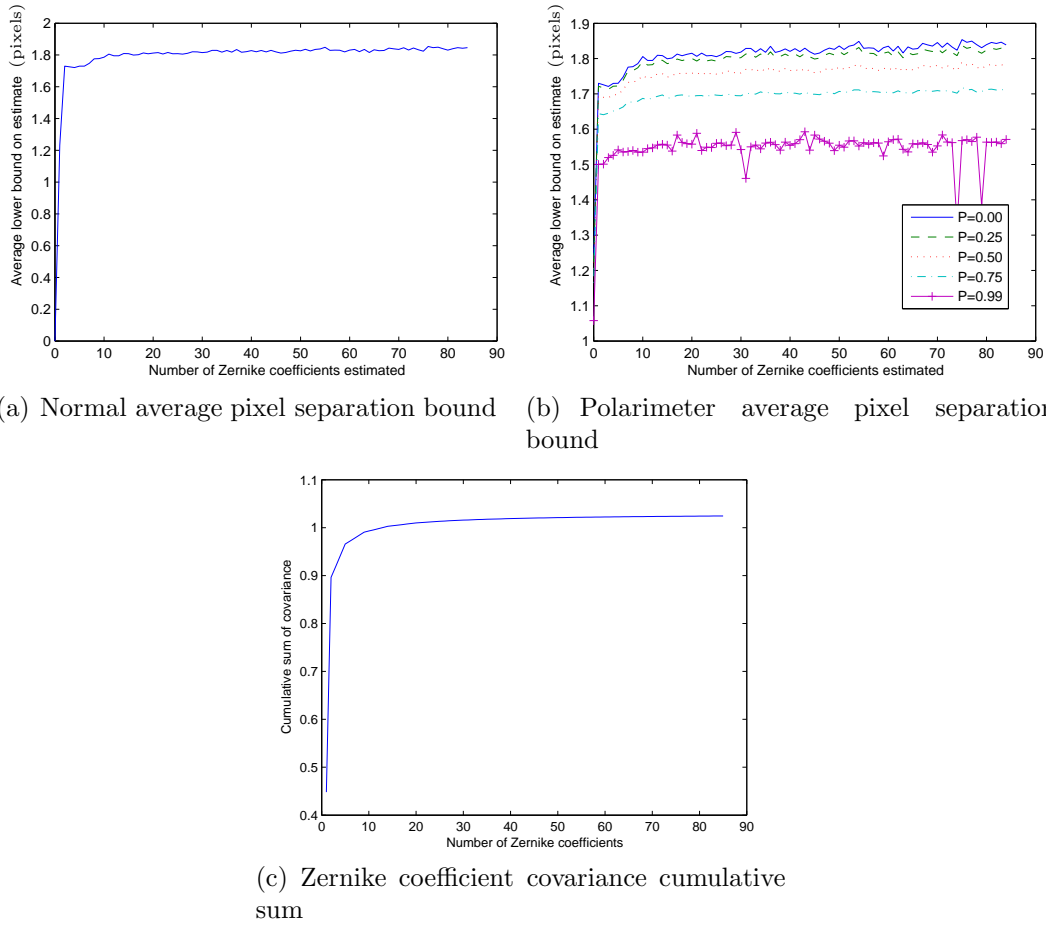


Figure 3.5: Average bound relative to number of Zernike coefficients estimated.

Although the average spatial frequency CRLB changes as the number of Zernike coefficients changes, the average CRLB of the point source intensity estimates change very little. Very slight variations of the bounds are noted in Figure 3.6, but the plots are almost flat as the number of coefficients is increased. When the model is unpolarized all estimates for the point sources have the same values. As the degree of polarization increases, the intensities of O_{oh} and O_{1v} increase in the model with a corresponding increase in the average lower bound of their estimates. The converse is true for O_{ov} and O_{1h} .

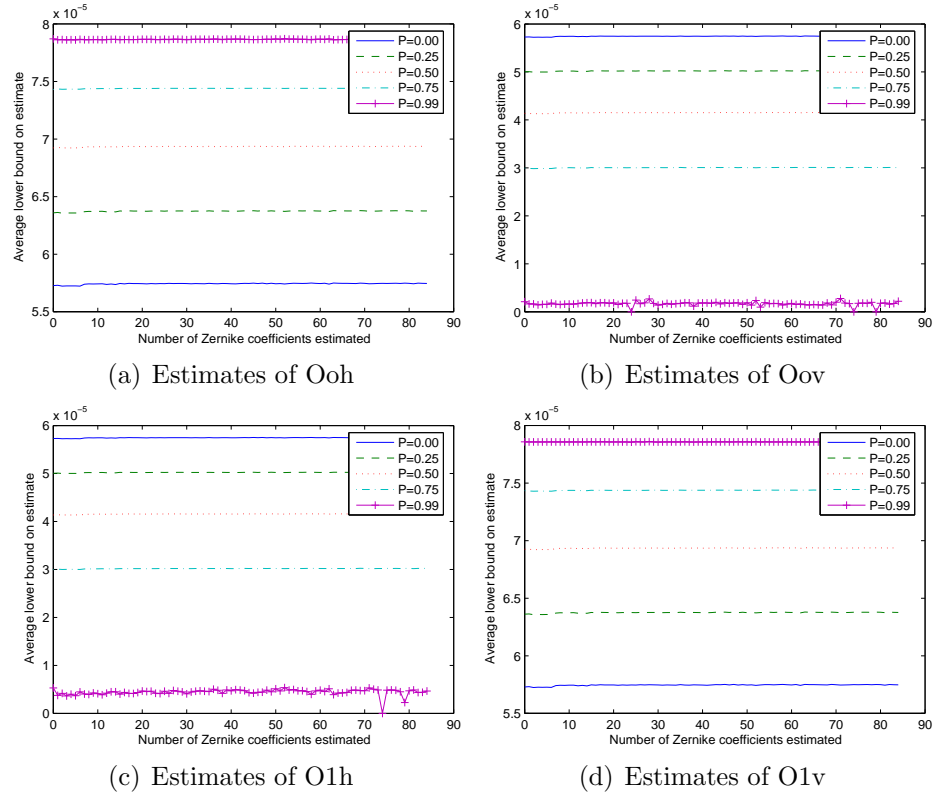


Figure 3.6: Intensity estimates vs. number of coefficients estimated.

Another parameter that affects the model's estimates is the light intensity of the point sources. For simplicity both source are fixed at the same magnitude. While all other parameters are fixed, the intensity is adjusted to produce the curve shown in Figure 3.7. As the intensity is increased, the average spatial frequency CRLB

decreases asymptotically to one pixel width. Conversely, as the intensity is decreased, the average spatial frequency CRLB increases.

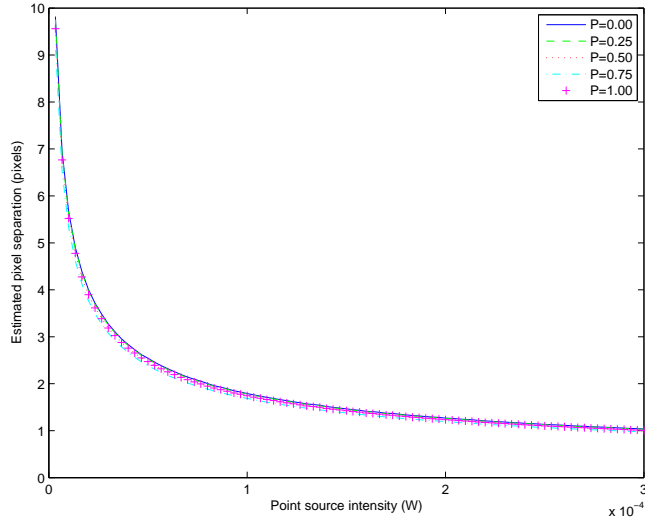


Figure 3.7: Average bound vs. point source intensity.

The preceding analysis in this paper assumes a D/r_o fraction of 1, where r_o is the Fried parameter (r_o) [33]. This section, however, discusses the effect of an r_o value less than the aperture size such that $D/r_o = 8$. The plots shown in Figure 3.8 reflect this increased “turbulence.” The left image, Figure 3.8(a), plots the average spatial frequency lower bound for each polarization case. The results are from the averaging of 200 independent iterations at each polarization setting.

The impact of an AO system is also modeled. Assuming an AO system can remove 95% of the tilt coefficients, the results shown in Figure 3.8(b) are attained. The initial part of the plots is greatly smoothed out and the overall bounds are improved significantly. For the last case, the following characteristics are assumed regarding the “AO” system’s compensation of aberrations:

- 95% tip/tilt compensated
- 80% defocus and astigmatism compensated
- 50% coma, trifocal, and spherical compensated

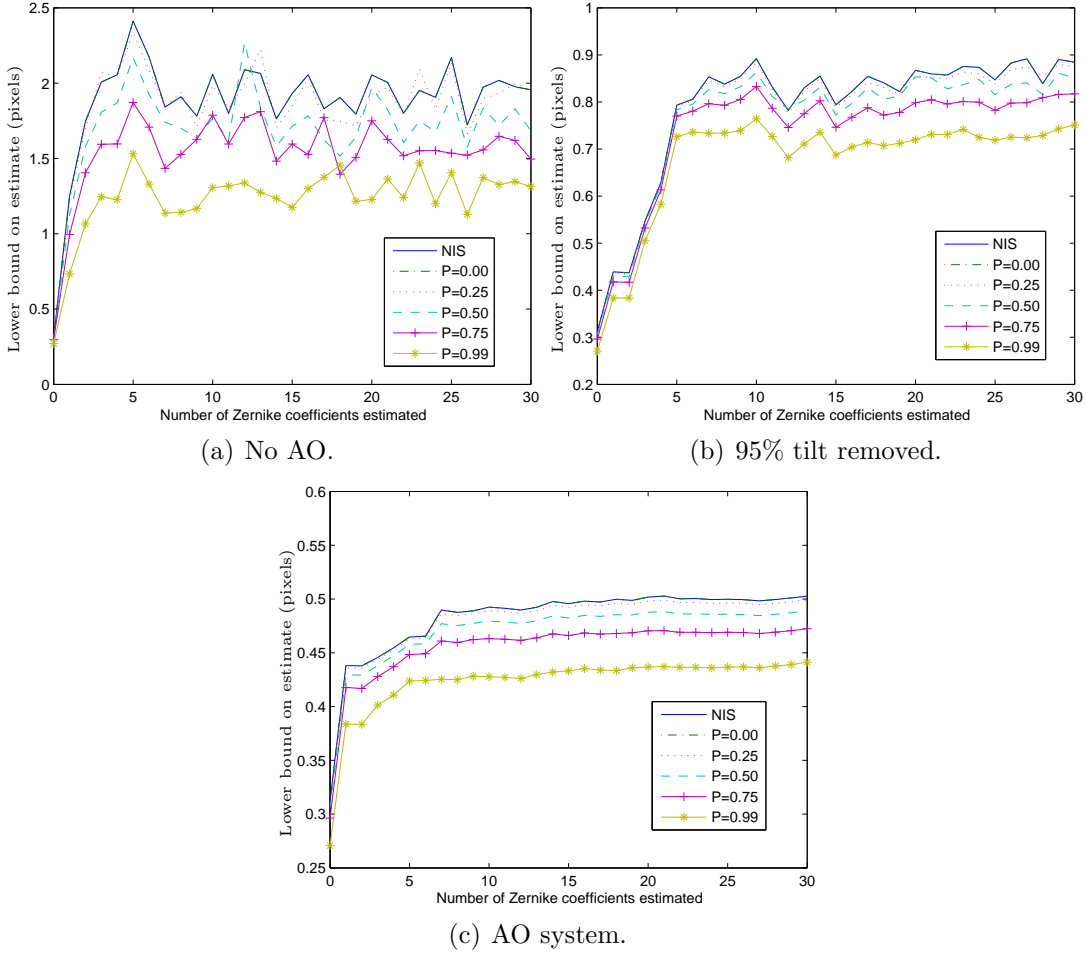


Figure 3.8: Effect of removing lower order aberrations.

The bounds are significantly smoothed out, in Figure 3.8(c), for the entire range of Zernike coefficients. The results show that the model can incorporate AO parameters for estimation of the spatial frequency CRLB under different atmospheric conditions. Thus, if one knows the performance characteristics of an AO system and the r_o value during the observation, one can use the model to predict the lower bound on spatial frequency resolution that can be attained by any algorithm.

This chapter incrementally developed the spatial resolution CRLB for a two-channel polarimeter with atmospheric turbulence. Starting with a normal imaging system. Then the PMF is extended to two channels. Finally, the psf is extended to include a Zernike polynomial based phase screen turbulence model. The CRLB on

the estimate of the pixel separation is compared as the models increase in complexity. The next chapter details the development of calibrated test data used to test any algorithms developed, along with a new approach for detecting focus aberrations in a single imaging channel.

IV. Laboratory Data Calibration

This chapter discusses the data used in development and testing of the polarimeter multi-frame blind deconvolution (PMFBD) algorithm. Since tip/tilt aberrations do not affect short-exposure image quality [33] and are fairly easy to remove through other methods they are not used for algorithm development for this research. The defocus aberration used in algorithm development is one of the next most significant aberrations caused by atmospheric turbulence. It is also a simple aberration to create in the laboratory environment by simply moving the lens. This allows testing of the developed algorithm with calibrated data in addition to simulated data.

Following the section on the focus aberration, an innovative focus aberration detection (FAD) algorithm is presented. The algorithm is used to detect the magnitude of the focus aberration present in a single imaging channel. Due to the multiple optical paths in a polarimeter, focus aberration detection is important in calibration of the separate channels. The results of the FAD algorithm are used for validation of the laboratory setup and simulation used to produce additional images for testing. The chapter concludes with a brief discussion of a potential autofocus algorithm using the FAD algorithm and possible methods of improving the FAD algorithm's wallclock execution time.

4.1 Focus Aberration

There are many factors that can contribute to an out of focus image. From geometrical optics, equations for focus are well established. Using simplifying techniques, a basic optical system can be simplified to an object, a lens, an image plane, and the distances between them. Using this very simple system, the location of the image plane is determined by the equation [16]

$$d_{image} = d_{object} \cdot f / (d_{object} - f) \quad (4.1)$$

where d_{object} is the distance between the object of interest and the lens, d_{image} is the distance between the lens and the image plane, and f is the focal length of the lens.

Regardless of the cause of the focus aberration, its characteristic shape remains the same. A Zernike polynomial representation is used to create the phase screen in the algorithm, where the phase screen is

$$\text{phase screen} = \text{pupil} \cdot \exp \left[-j\alpha \cdot \frac{\lambda}{2\pi} \cdot \text{Zernike}_4 \right]. \quad (4.2)$$

For simplicity, a circular pupil is chosen. α is the magnitude of the focus aberration in waves and Zernike_4 [33] is the Zernike polynomial for focus. By adding the factor $\lambda/2\pi$, where λ is the wavelength of light in the scenario, the analysis becomes wavelength independent [4]. The phase screen is then used to generate the OTF used in the deconvolution algorithm.

The OTFs for several focus aberrations are shown in Figures 4.1(a), 4.1(b), and 4.1(c). The aberrations are normalized for incoherent imaging such that the corners of the plots are at $f_X = 2f_o$.

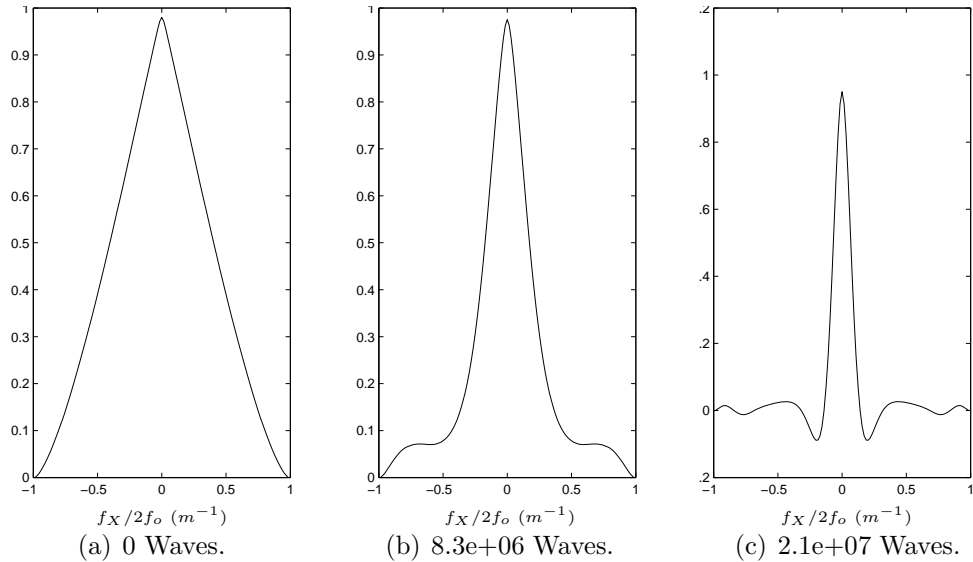


Figure 4.1: OTFs for three different focus aberrations.

The OTF equation [15] for the focus aberration in one dimension is

$$\mathcal{H}(f_X) = \Lambda\left(\frac{f_X}{2f_o}\right) \text{sinc} \left[\frac{8W_m}{\lambda} \left(\frac{f_X}{2f_o} \right) \left(1 - \frac{|f_X|}{2f_o} \right) \right]. \quad (4.3)$$

The effect of the *sinc* function on the triangle function Λ , as the path length error W_m is increased, is clearly evident in the corresponding OTF plots. f_o is the cutoff frequency and f_x is the location in the frequency domain. λ is the wavelength of the light. The next section provides more detail on the use of the OTF in detection of the phase aberration of the EO image.

4.2 Focus Aberration Detection Algorithm

Using only post-processing of a camera image, the FAD algorithm developed estimates the amount of focus error in the EO system. This is accomplished through the use of a MAP estimator [45]. The FAD algorithm detailed in this section is shown in Figure 4.2.

4.2.1 Generate phase screens. The size of the input image is used to determine the size of the aperture and the phase screen used. With the assumption that an image is N by N pixels, the aperture and phase screen are $N/2$ pixels in diameter. A Zernike polynomial representation of the focus aberration phase screen is used in the ML estimation of the deconvolved object. The Zernike polynomial needs to be generated once at the start, and then scaled by the magnitude of the aberration throughout the remainder of the iterations.

4.2.2 Input image. The FAD algorithm is initialized by reading in the camera image ($d(x, y)$) for estimation of its focus aberration. This image can be from any arbitrary scene under observation. An additional set of dark images are used to set the bias for the camera images used in the algorithm.

4.2.3 Generate log-likelihood plot. The heart of the FAD algorithm is the use of an RL style algorithm [30]. The algorithm assumes a known aberration. Starting with a known OTF, the algorithm deconvolves an object. The object is then an input to a log-likelihood equation to calculate a value for that object. The estimator uses

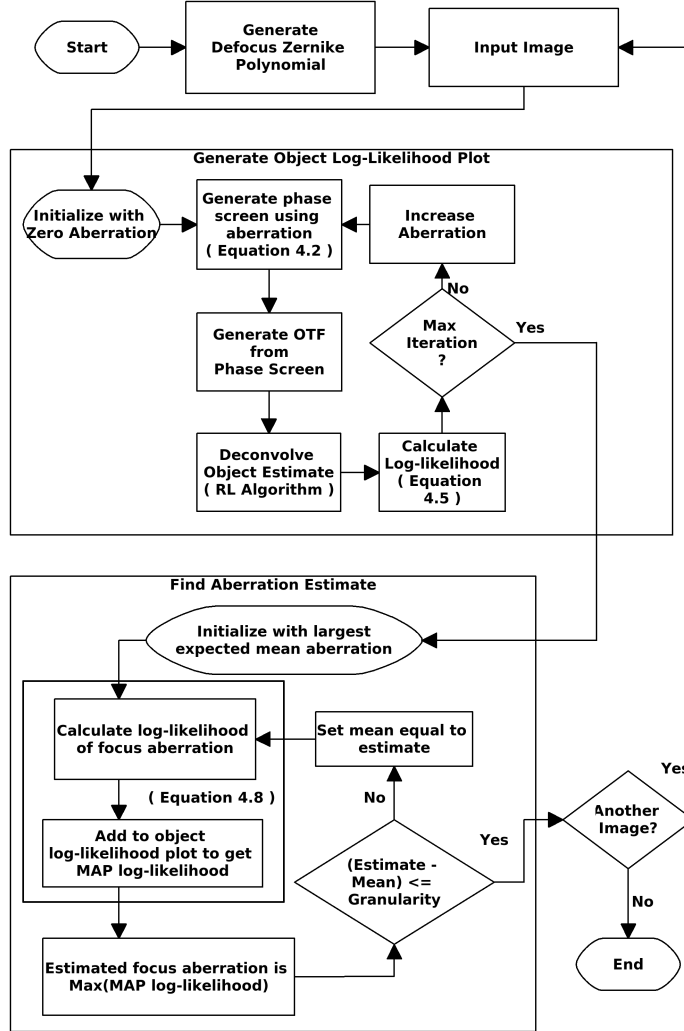


Figure 4.2: Focus Aberration Detection Algorithm.

the PMF of a Poisson dominated image

$$p_{d|z}(D|Z) = \prod_x \prod_y \left(\frac{i(x,y)^{d(x,y)} \exp^{-i(x,y)}}{d(x,y)!} \right) \quad (4.4)$$

where d is a single observation of a random variable with range D and z is a single observation of a random variable with a range Z . For this domain, d is a single image frame with a range of non-negative integers and z is the focus error over the range of possible focus errors. The Poisson PMF is used to generate the log-likelihood of the

estimate, $\mathcal{L}(o, z)$.

$$\mathcal{L}(o, z) = \sum_x \sum_y [d(x, y) \ln(i(x, y)) - i(x, y) - \ln(d(x, y)!)] \quad (4.5)$$

where $i(x, y)$ is the image generated from the RL estimated object by convolution with the known aberration. The term $\ln(d(x, y)!)$ is a constant term which does not vary as the focus aberration changes and is therefore discarded in the calculation. Due to a characteristic of the focus aberration a fairly smooth plot of the likelihood of the deconvolved object is generated as the focus aberration is varied. As the known aberration changes, the log-likelihood of the estimates remain fairly flat until the aberration is increased past the actual focus aberration present in the system. Past this point the log-likelihood decreases. The algorithm iterates in 300 increments from zero to some maximum focus aberration. The granularity of the setup used amounts to 208243 waves or 23mm in displacement for each increment. This is calculated using the right side of Equation 4.2 with α equal to the increment multiplied by the atmospheric Zernike covariance value for defocus of 0.0232. [33]. At increment 300, this amounts to 62472814 waves of focus aberration. The plots for lens positions at 0.439m, 0.388m, and 0.350m from the CCD are shown in Figure 4.3(a), 4.3(b), and 4.3(c) respectively.

4.2.4 Estimate focus aberration. Once a log-likelihood plot is generated, the probability of the defocus estimate is added to it using the MAP equation

$$p_{z|d}(Z|D) = \frac{p_{d|z}(D|Z)p_z(Z)}{P_d(D)}. \quad (4.6)$$

$P_{z|d}(Z|D)$ is the probability of the focus aberration z given the data d and $P_z(Z)$ is a standard Gaussian random variable for the focus aberration

$$p_z(Z) = \frac{1}{2\pi\sigma} \exp^{\frac{-(Z-\bar{Z})^2}{2\sigma^2}}. \quad (4.7)$$

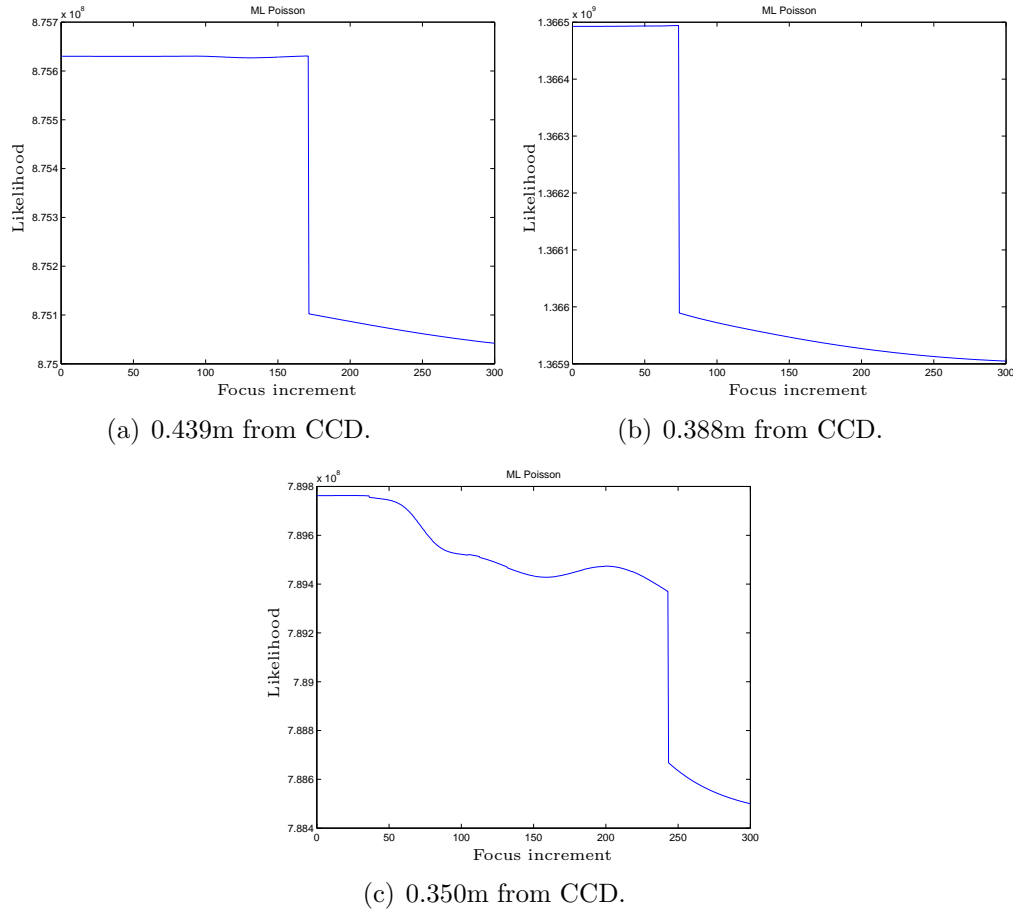


Figure 4.3: Log-likelihood plots at various lens positions.

Z is a random variable that represents the actual focus aberration with a standard deviation of σ .

The log of the MAP equation yields

$$\begin{aligned}
\ln(p_{z|d}(Z|D)) &= \ln \left(\frac{p_{d|z}(D|Z)p_z(Z)}{P_d(D)} \right) \\
&= \ln(p_{d|z}(D|Z)) + \ln(p_z(Z)) - \ln(P_d(D)) \\
&\approx \mathcal{L}(o, z) + \frac{(Z - \bar{Z})^2}{2\sigma^2}.
\end{aligned} \tag{4.8}$$

The estimate is determined by an iterative algorithm, depicted in the large block in the lower left area of Figure 4.2, since the actual value of the mean focus aberration,

\bar{Z} , is unknown and must be estimated. The maximum possible \bar{Z} is used to initialize the algorithm. The resulting value of Z that produces the maximum value of the sum is the current estimate of the magnitude of the focus aberration. When the current estimate differs from \bar{Z} by less than the granularity of the plot, the algorithm terminates. If the difference is greater than one increment, the estimate is then used to update the *a priori* estimate of \bar{Z} for the next iteration. For the granularity of the plots used, the algorithm always converged to a value in less than five iterations. This final value is the MAP estimate of the magnitude of the focus aberration for the image.

The choice of value for the focus covariance affects the performance of the estimator. If the choice is too small then poor estimates are possible as the estimator gets trapped at a local maximum and not the global maximum. The erroneous estimates are predominantly at the shorter focus aberrations and are seen in the additional structure visible in Figure 4.4. This is due to the additional and more pronounced local maximums in the log-likelihood plots as the actual focus aberration is decreased. An additional local maximum is shown in Figure 4.3(c) at an aberration estimate near increment 200. As the choice of focus covariance is increased the algorithm will pass over these local maxima to find the global maximum. The erroneous estimates are thus reduced as the focus covariance increases as shown in Figure 4.5. However, if the choice is too large, the estimator will pass over all of the values in the likelihood plot and always estimate zero focus error. For the remainder of the results, a value of $212\mu m^2$ is used for the focus covariance as this corresponds to a standard deviation of the focus error of $1.4cm$. This $1.4cm$ focus error represents the uncertainty in ones ability to focus the system manually.

4.2.5 Repeat for remaining images. After the magnitude of the focus error is determined, the sign must be determined as well in order to move the lens in the correct direction to minimize it. In order to accomplish this a second image could

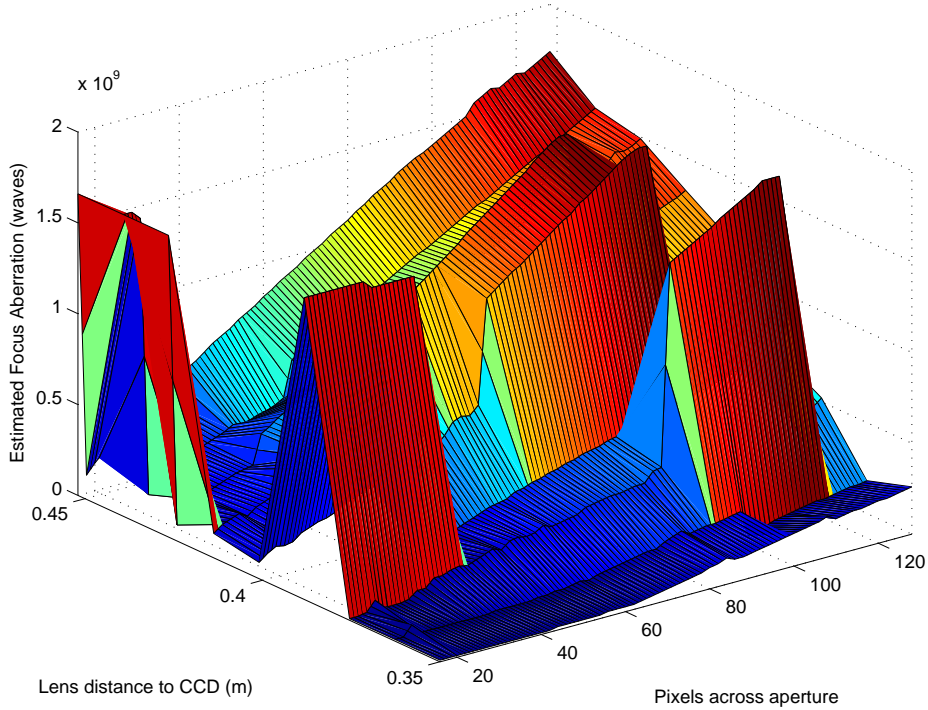


Figure 4.4: Focus Aberration Estimates versus Aperture Size, Focus Cov = $26\mu\text{m}^2$.

be gathered after the focal plane to lens relationship is altered. The resulting second focus error estimate would reveal the sign of the focus error.

4.3 Testing with Laboratory Data

The laboratory setup used in the development of the FAD algorithm uses an optics table with a CCD camera, a compound lens, and a target (see Figure 4.6.) The individual components are described in more detail.

4.3.1 Target. A set of bar targets provides an extended object for testing the algorithm. A red LED of 700nm wavelength is used to backlight the bars. An image of the target is shown in Figure 4.6(a).

4.3.2 Camera. The camera used is a Cascade 512F with a 512×512 CCD array. It is a monochromatic camera with a peak quantum efficiency approximately 88% at 700nm. The pixel size is $16\mu\text{m} \times 16\mu\text{m}$. For the images used in development

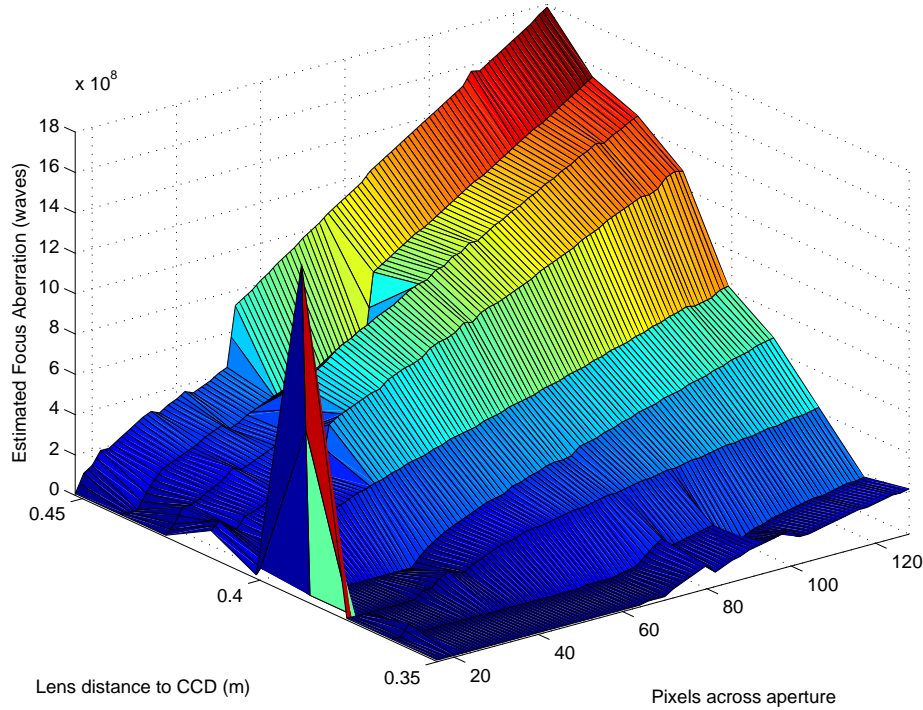


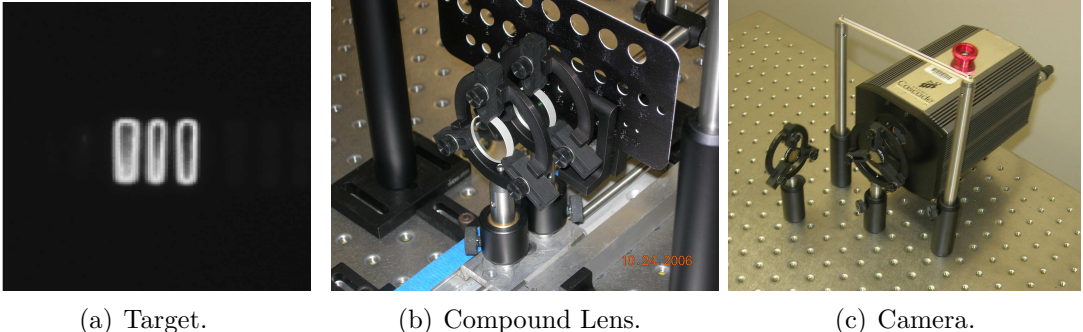
Figure 4.5: Focus Aberration Estimates versus Aperture Size, Focus Cov = $212\mu\text{m}^2$.

of the defocus detection algorithm, the integration time is set at $1\mu\text{s}$ and only the central 256X256 pixels are used. The resulting images have a signal-to-noise (SNR) ratio for the various positions shown in Figure 4.7.

4.3.3 Lens. The lens, shown in Figure 4.6(b), is composed of two convex lenses with a focal length, f , of 400mm . The lenses are mounted on a translation table as close together as possible. The separation between the two lenses, d_{lens} , is approximately 31mm . An aperture of 4mm in diameter is placed in front of the lens assembly. The compound focal length is approximately 192mm using the equation for the front focal length [16]

$$f.f.l. = \frac{f_1(d_{lens} - f_2)}{d_{lens} - (f_1 + f_2)} \quad (4.9)$$

of a compound lens. Because the focal length of both lenses is the same, $f_1 = f_2 = f$, both the front focal length and the back focal length are the same.



(a) Target.

(b) Compound Lens.

(c) Camera.

Figure 4.6: Laboratory Components.

4.3.4 Images. A series of images are collected with the compound lens adjusted in 13mm increments from an arbitrary starting location at 0.45m in front of the camera. A set of images is taken at that location and then the lens is moved towards the camera. Another set of images is then taken at the new location. This is repeated for an arbitrary number of locations. Only the compound lens is mounted to a translation table. Both the target and the camera are mounted in fixed locations.

4.4 Additional Considerations

4.4.1 Sampling effects. As with any image processing algorithm sampling has an effect on the results. To determine the minimum sampling requirements in the digital domain, both the cutoff frequency of the camera CCD array and the aperture are analyzed. First, the cutoff frequency of the camera is fixed due to the pixel pitch ($16\mu\text{m} \times 16\mu\text{m}$) of the CCD array. This fixes the sampling frequency of the camera at

$$CCD_{fs} = \frac{1}{16} \cdot 10e6 \text{ m}^{-1} = 62500\text{m}^{-1} \quad (4.10)$$

for the CCD. The images used are 256×256 pixels. Dividing by the number of pixels in the image ($N = 256$) results in the contribution to the spectrum per pixel, $S_p = 244\text{m}^{-1}$. Second, the cutoff frequency for incoherent imaging is defined as [15] $f_c = 2f_o$ where

$$f_o = \frac{D}{2\lambda \cdot z}. \quad (4.11)$$

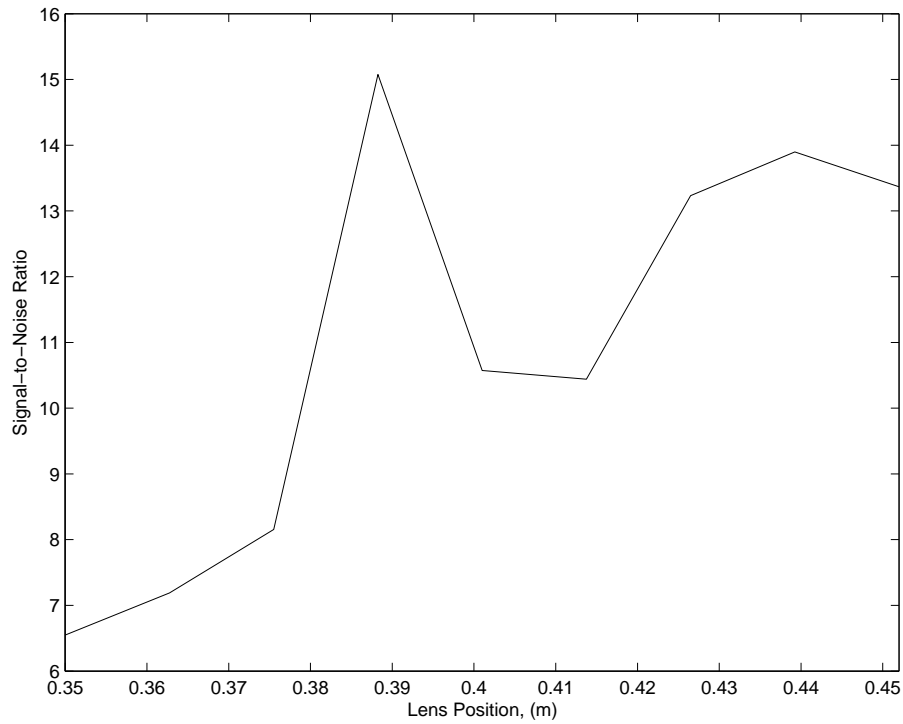


Figure 4.7: Signal-to-noise ratio versus lens position.

D is the aperture diameter and z is the distance between the CCD and the aperture. With the aperture at a distance of 0.45m from the CCD, the cutoff frequency is $12855m^{-1}$. With the aperture at a distance of 0.33m from the CCD, the cutoff frequency is $17305m^{-1}$. Thus the constraint on the cutoff frequency of the image is determined by the location of the lens array.

To meet minimum sampling requirements in the digital domain, the number of samples across the “aperture” is calculated by dividing the limiting cutoff frequency by the spectrum per pixel contribution, S_p . For the aperture at its farthest point in the laboratory setup, a minimum of 52 pixels across the digital aperture is required. At its nearest point, a minimum of 70 pixels is required. The effects of sampling on the corresponding estimates are shown in Figure 4.5. The effects of undersampling are most noticeable for positions 1 to 4 if the aperture is less than 50 pixels across.

To explore the effects of sampling the number of pixels across the digital aperture is varied from 16 to 128 pixels. An interesting effect occurs with the focus aberrations

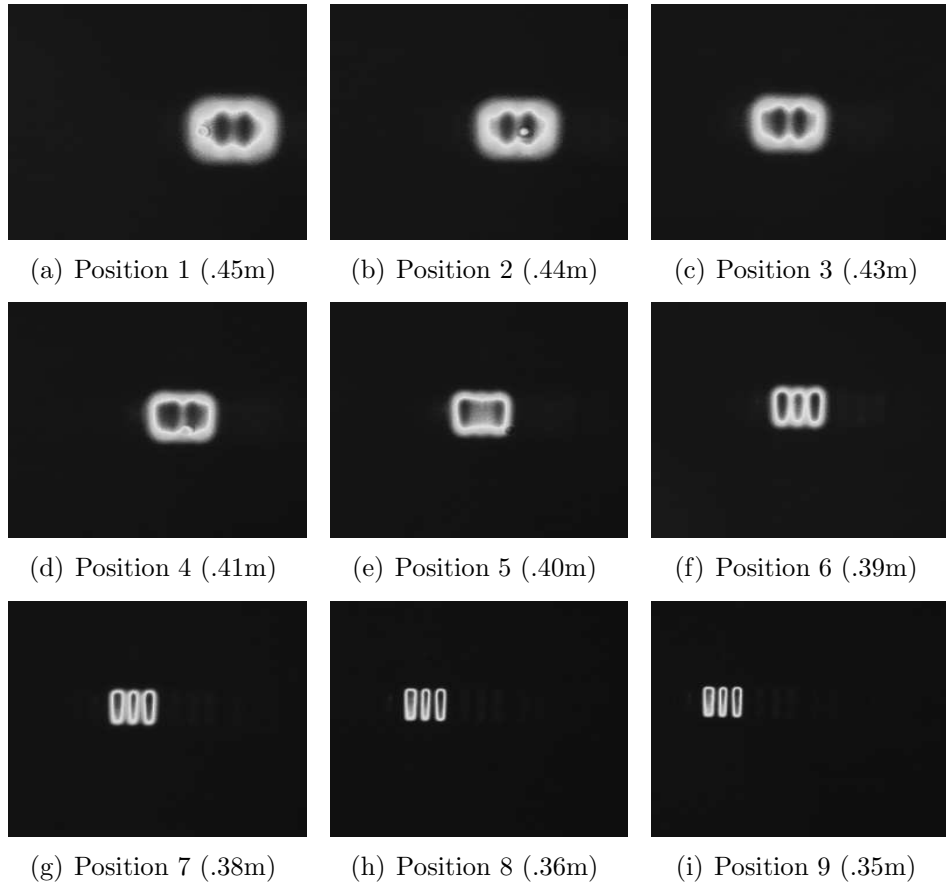


Figure 4.8: Camera images at various positions (distance to CCD.)

estimates as the number of pixels across the aperture is changed. Although the focus aberration estimates look like they are increasing as the number of aperture pixels are increased, the net effects on the deconvolved objects are negligible. Looking at Equation 4.3 again, this is explained by the change in f_X as the number of pixels is changed. As the number of pixels in the digital “aperture” is increased there is a corresponding decrease in frequency steps, f_X , in the frequency domain. Since f_o is fixed and f_X changes with the number of pixels, a corresponding change in W_m is required to maintain the same OTF as the sampling changes.

This is demonstrated by looking at the difference in deconvolved objects with an aperture width of 70 pixels versus an aperture width of 128 pixels. First, setting the width of the aperture to 70, as predicted by the previous analysis, results in the

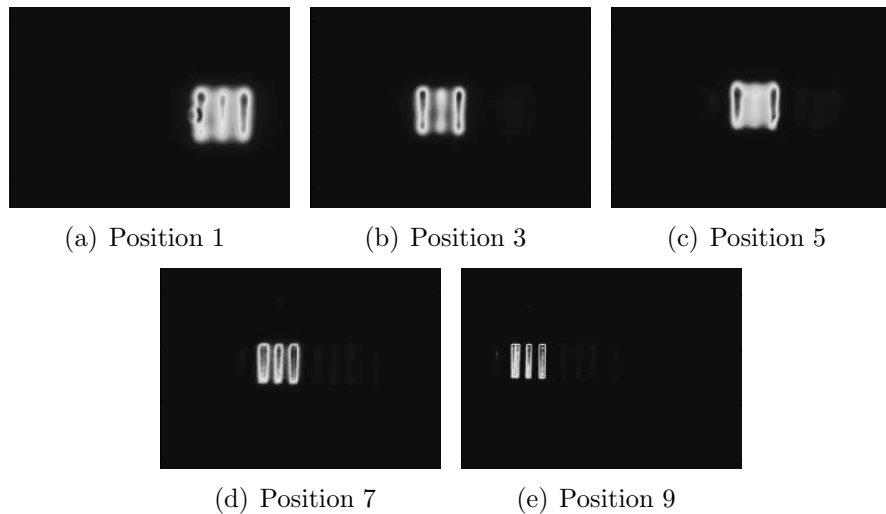


Figure 4.9: Objects using 70 pixel wide aperture.

corresponding deconvolutions shown in Figure 4.9. Changing the aperture width to 128 pixels across results in the deconvolutions shown in Figure 4.10. One can see that there is little difference between the sets of deconvolved objects. The only difference visible to the eye is between the two objects at position 5.

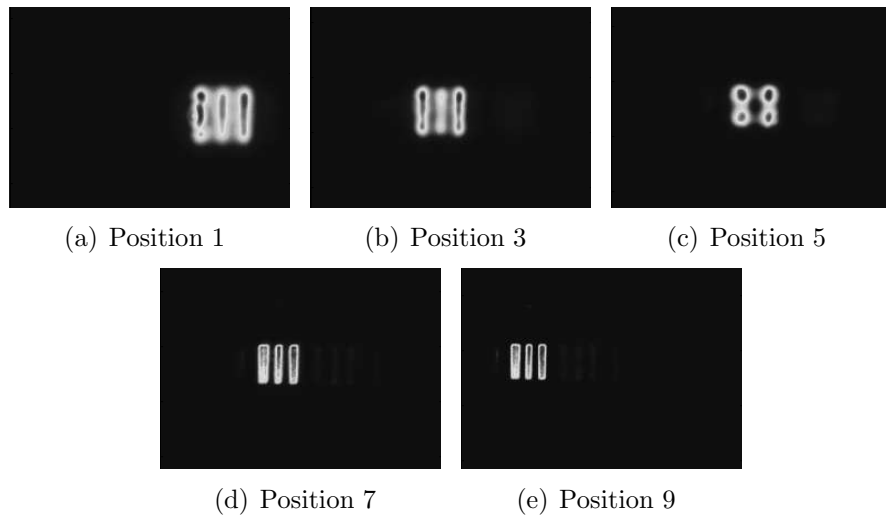


Figure 4.10: Objects using 128 pixel wide aperture.

If one takes estimates that were made at one aperture width and then uses them to deconvolve objects using an aperture with a different width, the results are visually poor. The larger the actual aberration and the greater the difference

in aperture width, the greater the error in deconvolution. This is demonstrated by taking the estimates from the FAD algorithm with an aperture width of 70 pixels and using them to deconvolve objects using an aperture width of 128 pixels. The resulting objects are shown in Figure 4.11. The most significant errors are at positions 1 and 3 which are at the greatest distance from the lens and thus have the largest actual focus aberration in the images.

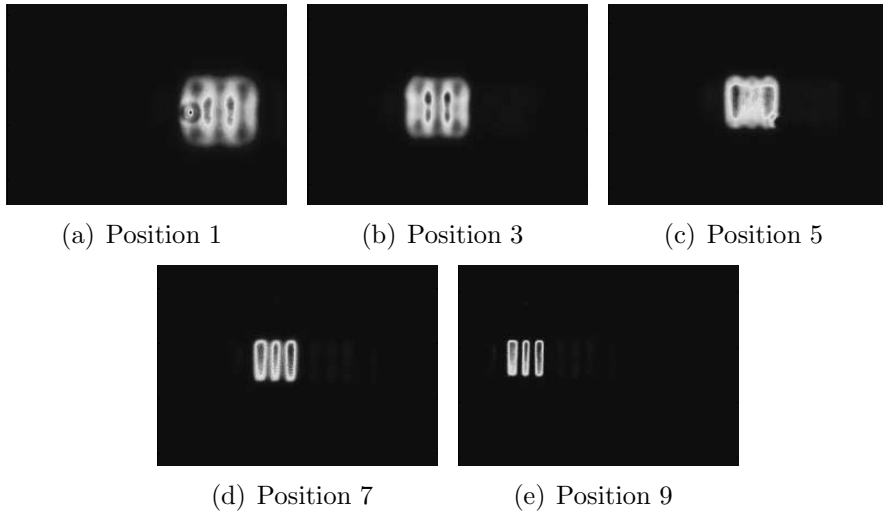


Figure 4.11: Objects using 70 pixel estimates with 128 pixel wide aperture.

The results of looking at the sampling requirements are what one expects from sampling theory. The first result is that undersampling results in poor estimates. The second result is that once sufficient sampling, i.e. the Nyquist frequency [15], is reached additional oversampling has little effect on the results.

4.4.2 Autofocus Algorithm. With at least one more image taken at a different lens location, the focus aberration estimates can be used to determine which side of the focal point the lens is on and thus the direction and relative movement of the lens required to focus the image. Using the estimated aberration for each image, the lens can then be repositioned to minimize the focus aberration.

4.4.3 Speedup. Several considerations have an effect on the wall-clock time required by the FAD algorithm. As written for this research, for each image processed,

the FAD algorithm requires approximately 75 minutes of wall-clock time running on a 64-bit processor running at 3GHz. The breakdown of the timing primarily comes from loading the images which requires 2.5 seconds, 15 seconds per iteration of the log-likelihood plot generation loop, less than a second for the rest of the algorithm. Therefore, the most significant way to speed up the algorithm is to speed up the log-likelihood plot generation loop. The number of loops required by the RL algorithm is at a minimum. Any additional reduction of the stall condition for the RL algorithm introduces additional structure in the plots that cause the FAD algorithm to produce erroneous estimations. A faster alternative would be to explore the use of an inverse Weiner filter to deconvolve the object instead of the RL algorithm.

There are several other possibilities to decrease the algorithm's wall-clock time depending on application. One simple improvement for immediate speedup comes from *a priori* knowledge of the focus aberration limit inherent in the electro-optical system. For the current setup this would result in reducing the plot generation loop from 300 to 200 points. That would immediately reduce the wall-clock time by one-third to approximately 50 minutes for the laboratory setup used. Another improvement by doubling the granularity of the plots would halve the wall-clock time. The trade space in the algorithm can be tailored to the application. One additional modification is valid regardless of application. Near linear speed up can be achieved with additional processors used to produce the ML plot. Adding one additional processor cuts the time required to produce the plot basically in half. The limit is attained when a processor is available for every point in the ML plot. This would result in a wall-clock time of approximately 18 seconds under the current setup. Additional speedup can be attained by a faster processor or specialized hardware tailored for the algorithm.

This chapter discussed the production of test data with calibrated focus errors. To detect the focus aberration present in the laboratory images, the FAD algorithm was developed. The calibrated data is available for testing of the algorithms derived in the next chapter.

V. Polarimeter Image Diversity Blind Deconvolution Algorithm Development

Using historical development of blind deconvolution, presented in Section 2.2, a blind deconvolution algorithm for a two channel polarimeter is developed. The algorithm makes use of an additional constraint between two imaging channels. The general development follows the generalized expectation maximization (GEM) algorithm development by Schulz [36] for his multiframe blind deconvolution (MFBD).

Starting with the historical basis for a single channel, the statistical model is extended to a two-channel polarimeter under the assumption of a known psf. This is followed by development of a polarimeter MFBD (PMFBD) algorithm when the assumption is removed.

5.1 Historical Basis

Standard imaging systems have a PMF for a single image such as

$$PMF_{(o)} = \prod_x \prod_y \left(\frac{i(x, y)^{d(x, y)} e^{p^{-i(x, y)}}}{d(x, y)!} \right) \quad (5.1)$$

for Poisson distributed intensity images. Where

$$i(x, y; o) = \sum_z \sum_w o(z, w) h(x - z, y - w). \quad (5.2)$$

Some terms defined for use in the GEM algorithm developed are:

- $\{\tilde{d}(x, y|z, w)\}$ is the complete data (CD) set and
- $\{d(x, y)\}$ is the incomplete data set

where there is a many-to-one mapping between the two sets as defined by $d(x, y) = \sum_z \sum_w \tilde{d}_x(x, y|z, w)$. Additionally, the expectations of the data are defined by Schulz as

$$E[\tilde{d}(x, y|z, w)] = o(z, w)h(x - z, y - w) \quad (5.3)$$

and

$$\begin{aligned}
E[d(x, y)] &= \sum_z \sum_w E[\tilde{d}(x, y|z, w)] \\
&= \sum_z \sum_w o(z, w) h(x - z, y - w) \\
&= i(x, y; o).
\end{aligned} \tag{5.4}$$

The CD log-likelihood function of the PMF is

$$\begin{aligned}
\mathbf{L}^{CD}(o) &= \sum_z \sum_w \sum_x \sum_y [\tilde{d}(x, y|z, w) \ln(o(z, w)h(x - z, y - w)) \\
&\quad - o(z, w)h(x - z, y - w) - \ln(\tilde{d}(x, y|z, w)!)].
\end{aligned} \tag{5.5}$$

The last term is a constant and is therefore dropped when maximizing the log-likelihood equation becoming

$$\mathbf{L}^{CD}(o) = \sum_z \sum_w \sum_x \sum_y [\tilde{d}(x, y|z, w) \ln(o(z, w)h(x - z, y - w)) - o(z, w)h(x - z, y - w)]. \tag{5.6}$$

A GEM algorithm for deconvolution with a known psf, requires that

$$\mathbf{L}^{CD}(o^{new}) \geq \mathbf{L}^{CD}(o^{old}) \tag{5.7}$$

and

$$Q(o^{new}|o^{old}) \geq Q(o^{old}|o^{old}) \tag{5.8}$$

where

$$Q(o|o^{old}) = E^{old} [\mathbf{L}^{CD}(o)|\{d(x, y)\}] \tag{5.9}$$

Maximizing Q with respect to the object results in

$$o^{new} = \arg \max_{o \in \mathfrak{O}} Q(o|o^{old}). \tag{5.10}$$

To satisfy the GEM requirement, one takes the partial derivative of the complete log-likelihood function with respect to the object and maximizes it. The partial

derivative is

$$\begin{aligned}
& \frac{\partial \mathbf{L}^{CD}}{\partial o(z_o, w_o)} \\
&= \frac{\partial}{\partial o(z_o, w_o)} \sum_z \sum_w \sum_x \sum_y [d(x, y|z, w) \ln(o(z, w) h(x - z, y - w)) \\
&\quad - o(z, w) h(x - z, y - w)] \\
&= \sum_x \sum_y \left[\frac{d(x, y|z, w)}{o(z_o, w_o)} \frac{\partial}{\partial o(z_o, w_o)} \sum_z \sum_w o(z, w) \right. \\
&\quad \left. - \frac{\partial}{\partial o(z_o, w_o)} \sum_z \sum_w o(z, w) h(x - z, y - w) \right] \\
&= \sum_x \sum_y \left[\frac{d(x, y|z, w)}{o(z_o, w_o)} - h(x - z_o, y - w_o) \right] \\
&= \sum_x \sum_y \left[\frac{d(x, y|z, w)}{o(z_o, w_o)} \right] - \sum_x \sum_y [h(x - z_o, y - w_o)] \\
&= \frac{\sum_x \sum_y d(x, y|z, w)}{o(z_o, w_o)} - 1
\end{aligned} \tag{5.11}$$

The result of the partial derivative is set equal to zero and solved for o :

$$o(z_o, w_o) = \sum_x \sum_y d(x, y|z, w). \tag{5.12}$$

Taking the expectation of the result is the expectation step in the EM algorithm. It is then maximized using the results of Shepp and Vardi. The expectation given the old object is

$$E^{old} [d(x, y|z, w)|d(x, y)] = \frac{h(x - z_o, y - w_o) o^{old}(x, y)}{i(x, y; o^{old})} d(x, y). \tag{5.13}$$

Substituting this into Equation 5.12 yields

$$o^{new} = o^{old} \sum_x \sum_y \frac{d(x, y)}{i(x, y; o^{old})} h(x - z_o, y - w_o). \tag{5.14}$$

which is the RL algorithm.

5.2 Algorithm Development

The first step in developing a polarimeter blind deconvolution algorithm is to develop a polarimeter deconvolution algorithm using a known *psf*. The approach taken is to modify the conventional GEM algorithm to work with two-channel polarimeter data. The PMF for the combination of a conventional image with an added polarization image is

$$PMF_{(o,p)} = \prod_z \prod_w \prod_x \prod_y \left[\frac{i_h(x, y; o, p, h)^{d_h(x, y)} \exp^{-i_h(x, y; o, p, h)}}{d_h(x, y)!} \right] \cdot \left[\frac{i(x, y; o, h)^{d(x, y)} \exp^{-i(x, y; o, h)}}{d(x, y)!} \right] \quad (5.15)$$

The image definitions for notation purposes arbitrarily define one image as the horizontally (h) polarized image and the other as the unpolarized primary image. The individual images are defined as

$$\begin{aligned} i(x, y; o) &= i_h(x, y; o, p) + i_v(x, y; o, p) \\ &= \frac{1}{2} \sum_x \sum_y o(z_o, w_o) (1 + \mathcal{P}(z_o, w_o)) h_1(x - z_o, y - w_o) \\ &\quad + \frac{1}{2} \sum_x \sum_y o(z_o, w_o) (1 - \mathcal{P}(z_o, w_o)) h_2(x - z_o, y - w_o) \end{aligned} \quad (5.16)$$

where $h(x, y)$ is the psf and $\mathcal{P}(z, w)$ is the degree of polarization [14].

5.2.1 Single polarimeter channel with known psf. The log-likelihood equation for a single polarimeter channel combined with the conventional channel is

$$\begin{aligned} \mathbf{L}^{CD}(o, p) &= \sum_z \sum_w \sum_x \sum_y [d_h(x, y|z, w) \ln(i_h(x, y)) - i_h(x, y) \\ &\quad + d(x, y|z, w) \ln(i(x, y)) - i(x, y)] \end{aligned}$$

$$\begin{aligned}
&= \sum_z \sum_w \sum_x \sum_y [d_h(x, y|z, w) \ln(o(z, w)p(z, w)h(x - z, y - w)) \\
&\quad - o(z, w)p(z, w)h(x - z, y - w) \\
&\quad + d(x, y|z, w) \ln(o(z, w)h(x - z, y - w)) \\
&\quad - o(z, w)h(x - z, y - w)]
\end{aligned} \tag{5.17}$$

where $p(z, w) = 1 + \mathcal{P}(z, w)$ to simplify the derivation. Taking the partial derivative with respect to o yields

$$\begin{aligned}
&\frac{\partial \mathbf{L}(o, p)}{\partial o(z_o, w_o)} \\
&= \frac{\partial}{\partial o(z_o, w_o)} \sum_z \sum_w \sum_x \sum_y [d_h(x, y|z, w) \ln(o(z, w)p(z, w)h(x - z, y - w)) \\
&\quad - o(z, w)p(z, w)h(x - z, y - w) \\
&\quad + d(x, y|z, w) \ln(o(z, w)h(x - z, y - w)) \\
&\quad - o(z, w)h(x - z, y - w)] \\
&= \sum_x \sum_y \left[\frac{d_h(x, y|z, w)}{o(z_o, w_o)} \cdot \left(\frac{\partial}{\partial o(z_o, w_o)} o(z, w) \right) \right. \\
&\quad \left. - \frac{\partial}{\partial o(z_o, w_o)} o(z, w)p(z, w)h(x - z, y - w) \right] \\
&\quad + \sum_x \sum_y \left[\frac{d(x, y|z, w)}{o(z_o, w_o)} \cdot \left(\frac{\partial}{\partial o(z_o, w_o)} o(z, w) \right) \right. \\
&\quad \left. - \frac{\partial}{\partial o(z_o, w_o)} o(z, w)h(x - z, y - w) \right] \\
&= \sum_x \sum_y \left[\frac{d_h(x, y|z, w)}{o(z_o, w_o)} - p(z_o, w_o)h(x - z_o, y - w_o) \right. \\
&\quad \left. + \frac{d(x, y|z, w)}{o(z_o, w_o)} - h(x - z_o, y - w_o) \right] \\
&= \frac{\sum_x \sum_y d_h(x, y|z, w) + \sum_x \sum_y d(x, y|z, w)}{o(z_o, w_o)} - p(z_o, w_o) - 1.
\end{aligned} \tag{5.18}$$

Setting this equal to zero and solving for $o(z, w)$

$$\begin{aligned} 0 &= \frac{\sum_x \sum_y d_h(x, y|z, w) + \sum_x \sum_y d(x, y|z, w)}{o(z_o, w_o)} - p(z_o, w_o) - 1 \\ 1 + p(z_o, w_o) &= \frac{\sum_x \sum_y d_h(x, y|z, w) + \sum_x \sum_y d(x, y|z, w)}{o(z_o, w_o)} \\ o(z_o, w_o) &= \frac{\sum_x \sum_y d_h(x, y|z, w) + \sum_x \sum_y d(x, y|z, w)}{1 + p(z_o, w_o)}. \end{aligned} \quad (5.19)$$

Taking the expectation given o^{old} and p^{old} yields

$$\begin{aligned} o^{new} &= \frac{o^{old} \cdot \sum_x \sum_y \frac{d_h(x, y)p^{old}(z, w)}{i_h(x, y; o^{old}, p^{old})} h(x - z, y - w)}{1 + p(z, w)} \\ &\quad + \frac{o^{old} \cdot \sum_x \sum_y \frac{d(x, y)}{i(x, y; o^{old})} h(x - z, y - w)}{1 + p(z, w)} \\ &= o^{old} \cdot \left[\frac{\sum_x \sum_y \left(\frac{p^{old}(z, w) \cdot d_h(x, y)}{i_h(x, y; o^{old}, p^{old})} + \frac{d(x, y)}{i(x, y; o^{old})} \right) h(x - z, y - w)}{1 + p(z, w)} \right]. \end{aligned} \quad (5.20)$$

In order to implement this an estimate for $p(z, w)$ in the denominator must be determined. This causes a slight deviation from a simple GEM algorithm. In this case, $p(z, w)$ is set to p^{old} with good results as shown in Section 6.1.2. The iterative algorithm becomes

$$o^{new} = o^{old} \cdot \left[\frac{\sum_x \sum_y \left(\frac{p^{old}(z, w) \cdot d_h(x, y)}{i_h(x, y; o^{old}, p^{old})} + \frac{d(x, y)}{i(x, y; o^{old})} \right) h(x - z, y - w)}{1 + p^{old}(z, w)} \right]. \quad (5.21)$$

Similarly, taking the partial derivative with respect to p yields

$$\begin{aligned}
& \frac{\partial \mathbf{L}(o, p)}{\partial p(z_o, w_o)} \\
&= \frac{\partial}{\partial p(z_o, w_o)} \sum_x \sum_y [d_h(x, y|z, w) \ln(o(z, w)p(z, w)h(x - z, y - w)) \\
&\quad - o(z, w)p(z, w)h(x - z, y - w) \\
&\quad + d(x, y|z, w)\ln(o(z, w)h(x - z, y - w)) \\
&\quad - o(z, w)h(x - z, y - w)] \\
&= \sum_x \sum_y \left[\frac{d_h(x, y|z, w)}{p(z_o, w_o)} \cdot \left(\frac{\partial}{\partial p(z_o, w_o)} p(z, w) \right) \right. \\
&\quad \left. - \frac{\partial}{\partial p(z_o, w_o)} o(z, w)p(z, w)h(x - z, y - w) \right] \\
&= \sum_x \sum_y \left[\frac{d_h(x, y|z, w)}{p(z_o, w_o)} - o(z_o, w_o)h(x - z_o, y - w_o) \right] \\
&= \frac{\sum_x \sum_y d_h(x, y|z, w)}{p(z_o, w_o)} - o(z_o, w_o). \tag{5.22}
\end{aligned}$$

Setting this equal to zero and solving for $p(z, w)$

$$p(z_o, w_o) = \frac{\sum_x \sum_y d_h(x, y|z, w)}{o(z_o, w_o)}. \tag{5.23}$$

Using the expectation of $d_h(x, y|z, w)$ given o^{old} and p^{old} yields

$$\begin{aligned}
p^{new} &= \frac{\sum_x \sum_y E^{old} [d_h(x, y|z, w)|d_h(x, y)]}{o(z_o, w_o)} \\
&= \frac{\sum_x \sum_y \frac{h(x - z_o, y - w_o)o^{old}(z_o, w_o)p^{old}(z_o, w_o)}{i_h(x, y; o^{old}, p^{old})} d_h(x, y)}{o(z_o, w_o)} \\
&= p^{old} \sum_x \sum_y \frac{o^{old}(z_o, w_o)d_h(x, y)}{o(z_o, w_o)i_h(x, y; o^{old}, p^{old})} h(x - z_o, y - w_o) \tag{5.24}
\end{aligned}$$

with an assumption similar to that used in Equation 5.21, such that $o(z_o, w_o)$ in the denominator is set to o^{old} , this simplifies to

$$p^{new} = p^{old} \sum_x \sum_y \frac{d_h(x, y)}{i_h(x, y; o^{old}, p^{old})} h(x - z_o, y - w_o). \quad (5.25)$$

Using the results of Equations 5.18 and 5.25 a new GEM algorithm is created for polarimeter deconvolution using a known psf.

5.2.2 PMFBD GEM algorithm. The polarimeter deconvolution algorithm is extended to blind deconvolution using a methodology similar to Schulz by adding multiple frames. The log-likelihood equations developed in the previous section are used to develop a multiframe GEM algorithm for blind deconvolution using polarimeter information. The desired property is that

$$\mathbf{L}(o^{new}, p^{new}, h^{new}) \geq \mathbf{L}(o^{old}, p^{old}, h^{old}) \quad (5.26)$$

and

$$Q(o, p, h | o^{old}, p^{old}, h^{old}) = Q_o(o | o^{old}, p^{old}, h^{old}) + Q_p(p | o^{old}, p^{old}, h^{old}) + Q_h(h | o^{old}, p^{old}, h^{old}) \quad (5.27)$$

where

$$Q(o, p, h | o^{old}, p^{old}, h^{old}) = E^{old}[\mathbf{L}^{CD}(o, p, h) | \{d_{pk}(x, y)\}, \{d_k(x, y)\}]. \quad (5.28)$$

where $E^{old} [\cdot | \{d_{pk}(x, y), d_k(x, y)\}]$ is the expectation, conditioned on the data from one polarization channel $d_{pk}(x, y)$ and the data from the primary channel $d_k(x, y)$, and assuming that the underlying object is o^{old} and the polarization data is p^{old} . Each

image pair, d_{pn} and d_m are assumed to have the same psf if $n = m$ and different psfs if $n \neq m$.

Any algorithm that meets these requirements such that

$$Q_o(o^{new}|o^{old}, p^{old}, h^{old}) \geq Q_o(o^{old}|o^{old}, p^{old}, h^{old}) \quad (5.29)$$

$$Q_p(p^{new}|o^{old}, p^{old}, h^{old}) \geq Q_p(p^{old}|o^{old}, p^{old}, h^{old}) \quad (5.30)$$

$$Q_h(h^{new}|o^{old}, p^{old}, h^{old}) \geq Q_h(h^{old}|o^{old}, p^{old}, h^{old}) \quad (5.31)$$

where

$$o^{new} = \arg \max_{o \in \mathfrak{O}} Q_o(o|o^{old}, p^{old}, h^{old}) \quad (5.32)$$

$$p^{new} = \arg \max_{p \in \mathfrak{P}} Q_p(p|o^{old}, p^{old}, h^{old}) \quad (5.33)$$

$$h^{new} = \arg \max_{h \in \mathfrak{H}} Q_h(h|o^{old}, p^{old}, h^{old}). \quad (5.34)$$

is a GEM algorithm.

The complete log-likelihood algorithm for one polarization channel in combination with the primary channel with multiple frames is

$$\begin{aligned} \mathbf{L}^{CD}(o, p, h_k) &= \sum_k \sum_z \sum_w \sum_x \sum_y \tilde{d}_{pk}(x, y|z, w) \ln(o(z, w)p(z, w)h_k(x - z, y - w)) \\ &\quad - \sum_k \sum_z \sum_w \sum_x \sum_y o(z, w)p(z, w)h_k(x - z, y - w) \\ &\quad + \sum_k \sum_z \sum_w \sum_x \sum_y \tilde{d}_k(x, y|z, w) \ln(o(z, w)h_k(x - z, y - w)) \\ &\quad - \sum_k \sum_z \sum_w \sum_x \sum_y o(z, w)h_k(x - z, y - w). \end{aligned} \quad (5.35)$$

The previous results for the deconvolution with a known psf still hold for calculating o^{new} and p^{new} , there are just individual loops for each frame and a method for combining the results. In this case a simple averaging is used such that

$$o^{new} = \text{mean}(o_k^{new}) \quad (5.36)$$

$$p^{new} = \text{mean}(p_k^{new}) \quad (5.37)$$

However, an iterative update is derived for the individual psfs by maximizing the complete log-likelihood equation with respect to the psfs. The partial derivative of the complete log-likelihood equation with respect to $h_k(z_o, w_o)$ is

$$\begin{aligned} \frac{\partial}{\partial h_k(x_o, y_o)} \mathbf{L}^{CD}(o, p, h_k) &= \\ \frac{\partial}{\partial h_k(x_o, y_o)} \left[\sum_k \sum_z \sum_w \sum_x \sum_y \tilde{d}_{pk}(x, y | x - z, y - w) \right. & \\ \cdot \ln(o(x - z, y - w)p(x - z, y - w)h_k(z, w)) & \\ - \sum_k \sum_z \sum_w \sum_x \sum_y o(x - z, y - w)p(x - z, y - w)h_k(z, w) & \\ + \sum_k \sum_z \sum_w \sum_x \sum_y \tilde{d}_k(x, y | x - z, y - w) \ln(o(x - z, y - w)h_k(z, w)) & \\ \left. - \sum_k \sum_z \sum_w \sum_x \sum_y o(x - z, y - w)h_k(z, w) \right] & \quad (5.38) \end{aligned}$$

$$\begin{aligned} &= \sum_z \sum_w \frac{\tilde{d}_{pk}(x, y | x - z, y - w)}{h_k(x_o, y_o)} - \sum_z \sum_w o(x_o - z, y_o - w)p(x_o - z, y_o - w) \\ &+ \sum_z \sum_w \frac{\tilde{d}_k(x, y | x - z, y - w)}{h_k(x_o, y_o)} - \sum_z \sum_w o(x_o - z, y_o - w)]. \quad (5.39) \end{aligned}$$

Setting this equal to zero yields

$$h_k(x_o, y_o) = \frac{\sum_z \sum_w \tilde{d}_{pk}(x, y | x - z, y - w) + \sum_z \sum_w \tilde{d}_k(x, y | x - z, y - w)}{\sum_z \sum_w o(x_o - z, y_o - w)(1 + p(x_o - z, y_o - w))}. \quad (5.40)$$

Taking the expectation given o^{old} , p^{old} , and h_k^{old} yields

$$h_k^{new}(x, y) = \sum_z \sum_w \left[\frac{\frac{h_k^{old}(z, w)o^{old}(x-z, y-w)p^{old}(x-z, y-w)}{i_{pk}(x, y; o^{old}, p^{old}, h^{old})} d_{pk}(x, y)}{o(z, w)(1 + p(z, w))} \right] \\ + \sum_z \sum_w \left[\frac{\frac{h_k^{old}(z, w)o^{old}(x-z, y-w)}{i_k(x, y; o^{old}, h^{old})} d_k(x, y)}{o(z, w)(1 + p(z, w))} \right]. \quad (5.41)$$

With the same assumptions on $o(z, w)$ and $p(z, w)$ as in the previous development this simplifies to

$$h_k^{new} = h_k^{old} \cdot \sum_z \sum_w \left[\frac{\frac{d_{pk}(x, y)p^{old}(x-z, y-w)o^{old}(x-z, y-w)}{i_{pk}(x, y; o^{old}, p^{old}, h^{old})} + \frac{d_k(x, y)o^{old}(x-z, y-w)}{i_k(x, y; o^{old}, h^{old})}}{o^{old}(z, w)(1 + p^{old}(z, w))} \right] \\ = h_k^{old} \cdot \sum_z \sum_w \left[\frac{\frac{d_{pk}(x, y)}{i_{pk}(x, y; o^{old}, p^{old}, h^{old})} p^{old}(x - z, y - w) o^{old}(x - z, y - w)}{o^{old}(z, w)(1 + p^{old}(z, w))} \right] \\ + h_k^{old} \cdot \sum_z \sum_w \left[\frac{\frac{d_k(x, y)}{i_k(x, y; o^{old}, h^{old})} o^{old}(x - z, y - w)}{o^{old}(z, w)(1 + p^{old}(z, w))} \right]. \quad (5.42)$$

This chapter developed two polarimeter deconvolution algorithms for a two-channel polarimeter, where one channel is unpolarized and the other is polarization sensitive with arbitrary orientation. The initial algorithm is an extension of the RL algorithm to include the additional polarimeter channel assuming a known psf. The second is based on a GEM approach and is a polarimeter multiframe blind deconvolution algorithm. The previously developed calibrated data is used to test the algorithms. The results are presented in the next chapter.

VI. Results and Analysis of Polarimeter Algorithms

The results and analysis of the algorithm development in Chapter V are presented in this chapter. Comparison of the RL algorithm with the polarimeter deconvolution algorithm using simulation is presented in the first section. This is followed by the results using actual laboratory images. The final section presents a comparison between the Polarimeter MFBD algorithm developed and an RL based MFBD.

In order to compare the two algorithms' performance a metric is required. The metric chosen is based on the fidelity metric of Kattnig *et al.* [22]. To compare the two algorithms it is implemented as

$$fidelity(object, object_{deconvolved}) = \frac{\|object - object_{deconvolved}\|_{L_2}^2}{\|object\|_{L_2}^2}. \quad (6.1)$$

A perfectly reconstructed object would result in a value of zero for the metric. Therefore when comparing the results of both algorithms, a lower value is a better deconvolution. This applies only to the simulation results since the true object is unknown when using the laboratory images. Using simulated images that only have diffraction present, the average of 100 images results in the diffraction limited fidelity scores shown in Figure 6.1 for digital aperture sizes of 32, 48, and 64 pixels across the simulated aperture. The images used are 128×128 pixels in size. The results show that as the aperture size is decreased the resulting image is diffracted more thus resulting in a lower fidelity score.

6.1 Known psf with simulation data

A Matlab® simulation is used to compare the new polarization sensitive algorithm with the traditional RL algorithm. The simulated target is a bar target with a variable separation between the two bars. The bars are of variable widths in pixels and a fixed 17 pixels in height. The fidelity mapping algorithm starts at a minimum separation of one pixel and increments up to a 16-pixel separation. The algorithm

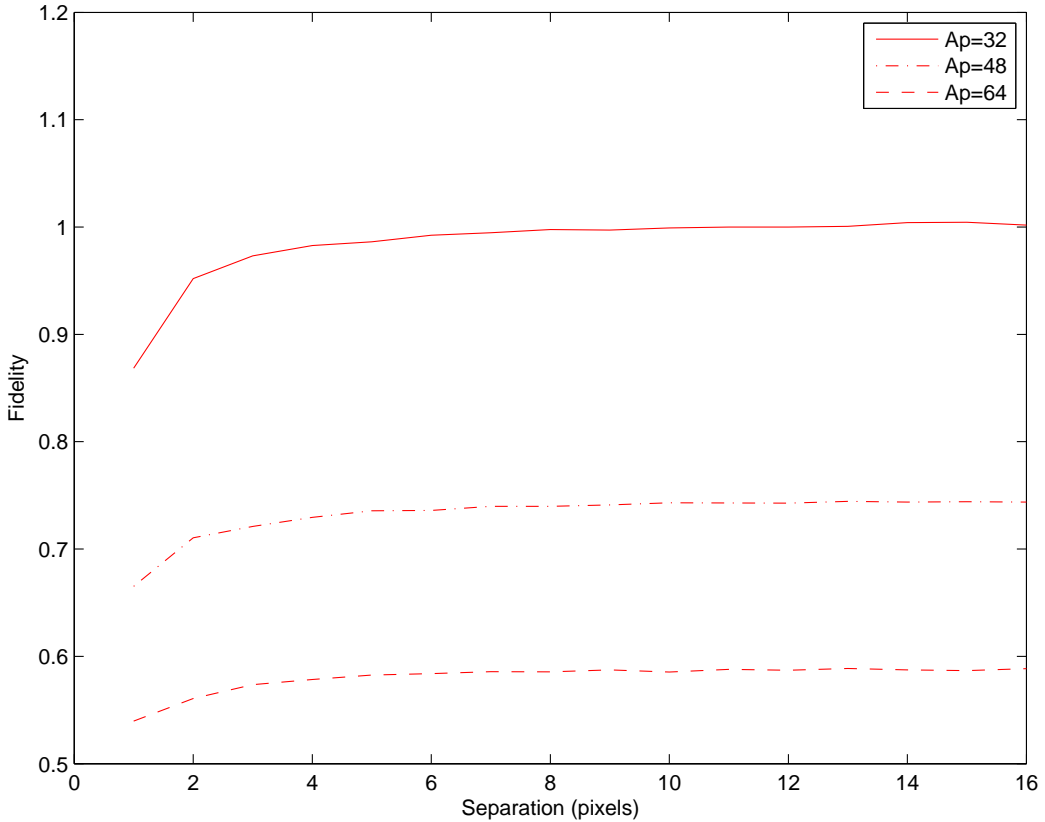


Figure 6.1: Fidelity metric for diffraction limited images for various digital aperture sizes, using target with bar width of 3 pixels, target irradiance of 1000 photons per pixel, and image size of 128.

also increments through 200 steps of increasing focus aberration. This is repeated for various noise levels. The SNR [9] for the test images is calculated using the equation

$$\begin{aligned}
 SNR &= \frac{\text{mean(signal)}}{\text{standard deviation(noise)}} \\
 &= \frac{2 * \text{bar width} * \text{bar height} * \text{number of photons per pixel}}{\text{standard deviation(noise)} * N^2}. \quad (6.2)
 \end{aligned}$$

The standard deviation of the noise for the Matlab® simulations is fixed at 0.6. Figure 6.2 shows the results for a bar width of three pixels, an irradiance of 1000 photons per pixel, and an image size of 128 pixels. The SNR of the test images is approximately 10. In the simulations, the SNR is calculated from the RL image, the other two images have half the value. This simulates the use of a 50/50 beam splitter cube in the optical

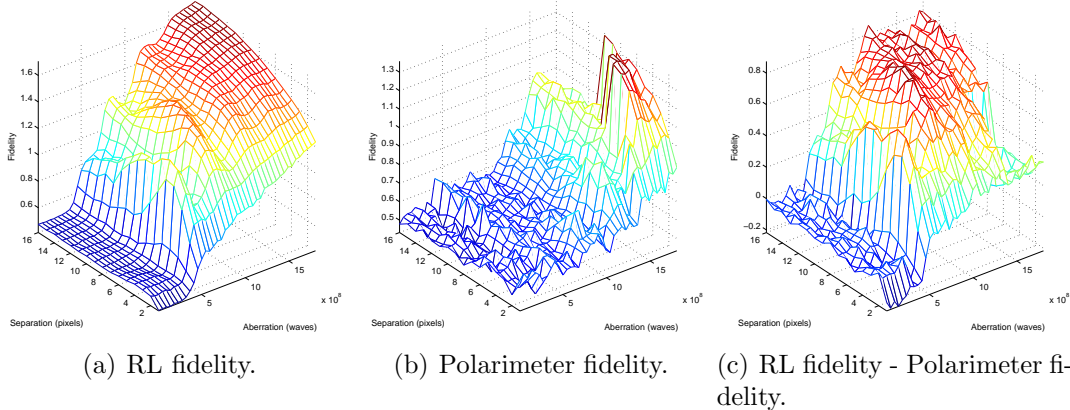


Figure 6.2: Map of fidelity metric for both the RL algorithm, the polarimeter algorithm, and their difference at an SNR of approximately 10.

path. With the configuration used this results in the sum of the polarimeter images having 3/4 of the photons of the RL algorithm.

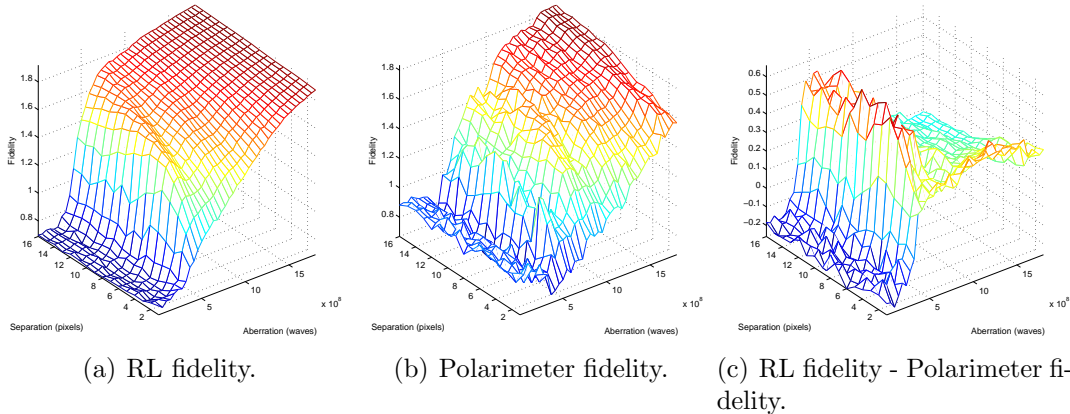


Figure 6.3: Map of fidelity metric for both the RL algorithm, the polarimeter algorithm, and their difference at an SNR of approximately 1.

Changing the signal or the irradiance of the target causes a corresponding change in the effectiveness of both algorithms. Reducing the signal to a target irradiance of 100 photons per pixel reduces the SNR of the images to approximately 1. The changes in the fidelity metric are shown in Figure 6.3. As the aberration is increased there is a corresponding decrease in performance of both algorithms. The greater the aberration, the more spread out the photons are in the resulting image and thus harder to reconstruct the original object due to a lower image SNR. If the assumption

of a beamsplitter is removed and one is considering the difference between the two algorithms on the same image, the results are shown in Figure 6.4. Note that in Figure 6.4(a) the RL algorithm now has half of the photons of the previous results shown in Figure 6.3(a). This results in the failure of the RL algorithm at much lower aberrations than the polarimeter algorithm. Also, instead of the RL algorithm having better performance in the low aberration region due to more light, the polarimeter algorithm now performs better than the RL algorithm in this region. It is clear that the polarimeter algorithm performs better than the RL algorithm when working with the same image from the primary channel.

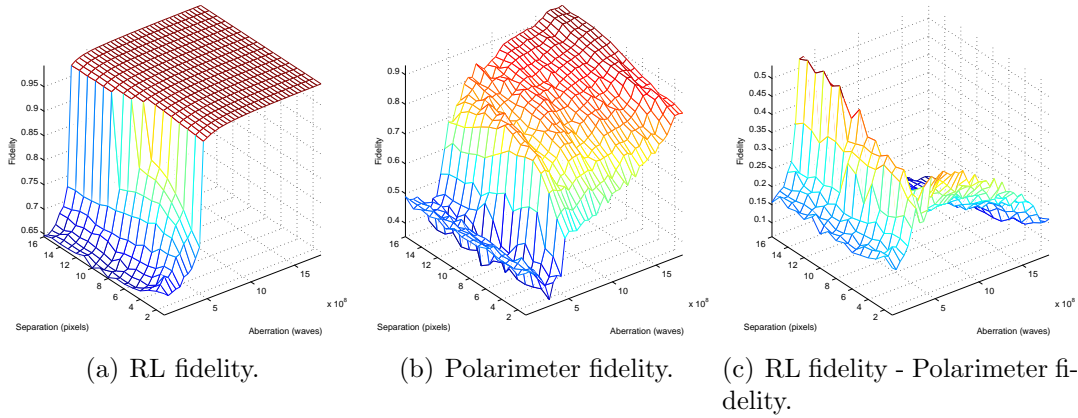


Figure 6.4: Map of fidelity metric for both algorithms without beamsplitter assumption at an SNR of approximately 1.

As the light levels are reduced, the polarimeter algorithm continues to maintain a better fidelity than the RL algorithm. Reducing the number of photons per pixel of the target to only 10 photons per pixel results in an SNR of approximately 0.1. The cross sectional views of the deconvolved objects by both algorithms, in Figure 6.5 shows an interesting difference between the two algorithms. For this comparison polarimeter algorithm has the beamsplitter assumption applied and even with only 3/4 of the photons that the RL algorithm has, the cross sections clearly show a much greater contrast for the polarimeter algorithm.

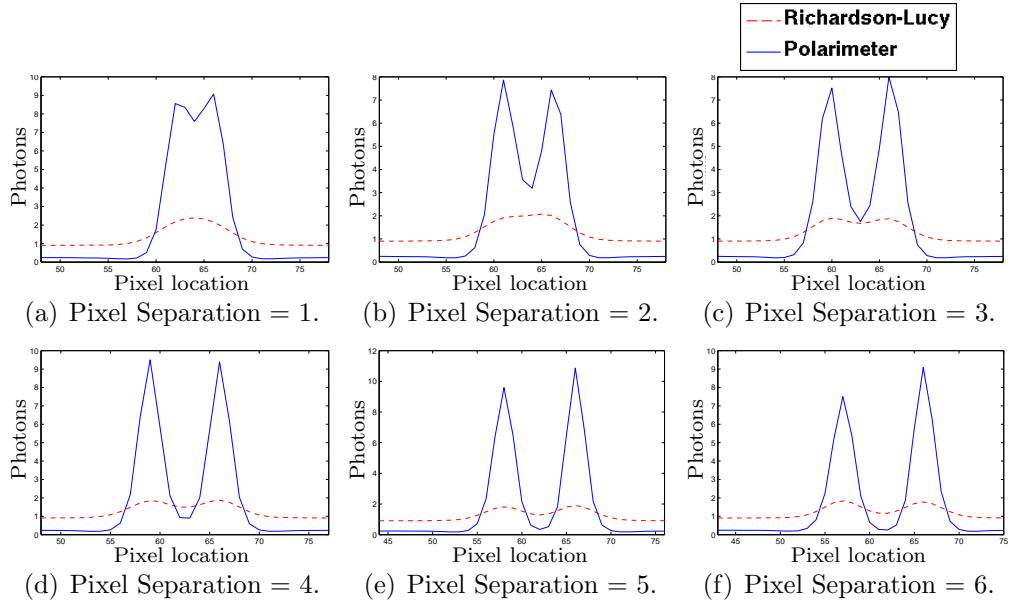


Figure 6.5: Cross-sectional views of deconvolved object with a barwidth of 3 pixels and a target irradiance of 10 photons per pixel.

6.1.1 Comparison of results with CRLB predictions. The bounds calculated in Section 3.3.11 show the ability of the polarimeter algorithm to produce a better estimate than conventional imaging under certain conditions. Generating images under these conditions allows a comparison between the two algorithms. The results shown are for images that are 512×512 pixels; used in order to increase the resolution of the results. In Figure 6.6, at a separation of 2 pixels, the polarimeter deconvolution algorithm has resolved the two bars using the Sparrow [16] criteria of a flat top between the two bars. The RL algorithm is able to resolve the two bars at a minimum pixel separation of 4 pixels. Thus under these lighting conditions the polarimeter algorithm achieves twice the resolution when compared to the RL algorithm.

Reducing the photons used for the cross sections in Figure 6.6 by 10% results in a corresponding reduction in SNR by 10% and results in the set of cross sections shown in Figure 6.7. When the light in the scenario is reduced, both algorithms require a larger pixel separation in order to resolve the bar target. In this case, the RL algorithm is unable to resolve the bars until the bars, that are only three pixels

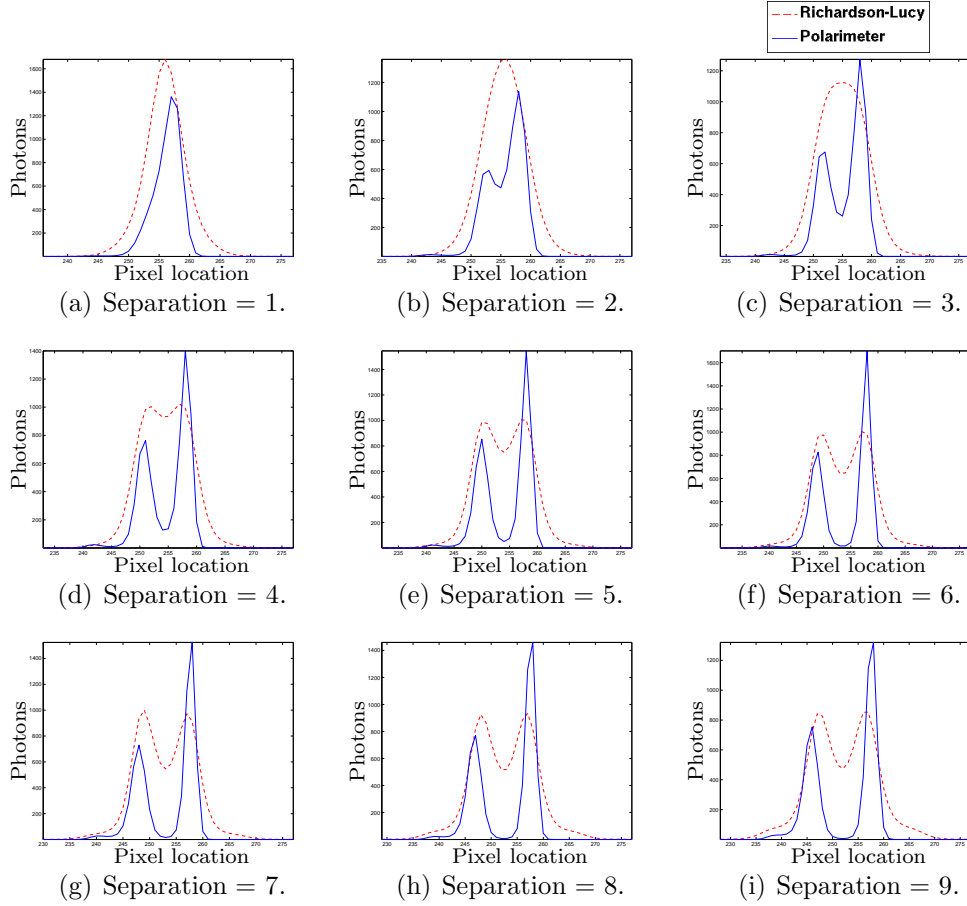


Figure 6.6: Cross-sectional views of deconvolved objects at an SNR of 0.71.

in width, are separated by 8 pixels. The polarimeter algorithm is able to resolve the bars at a bar separation of only 4 pixels.

As the CRLB results indicate, when lighting is sufficiently high and/or as the pixel separation is increased, the ability to resolve the two bars becomes similar. Adjusting the light to achieve a SNR of 6 results in the cross sectional views shown in Figure 6.8. Both algorithms can resolve the bars at a minimum separation of 1 pixel. The polarimeter algorithm still has a better fidelity score at the smaller separations due to the deeper valley between the peaks. The scores become nearly the same when the bars reach a separation of 5 pixels. However, the polarimeter fidelity score is better than the RL algorithm due to the flatter trough between the two bars and the greater flaring that occurs at the bottom of the RL bars.

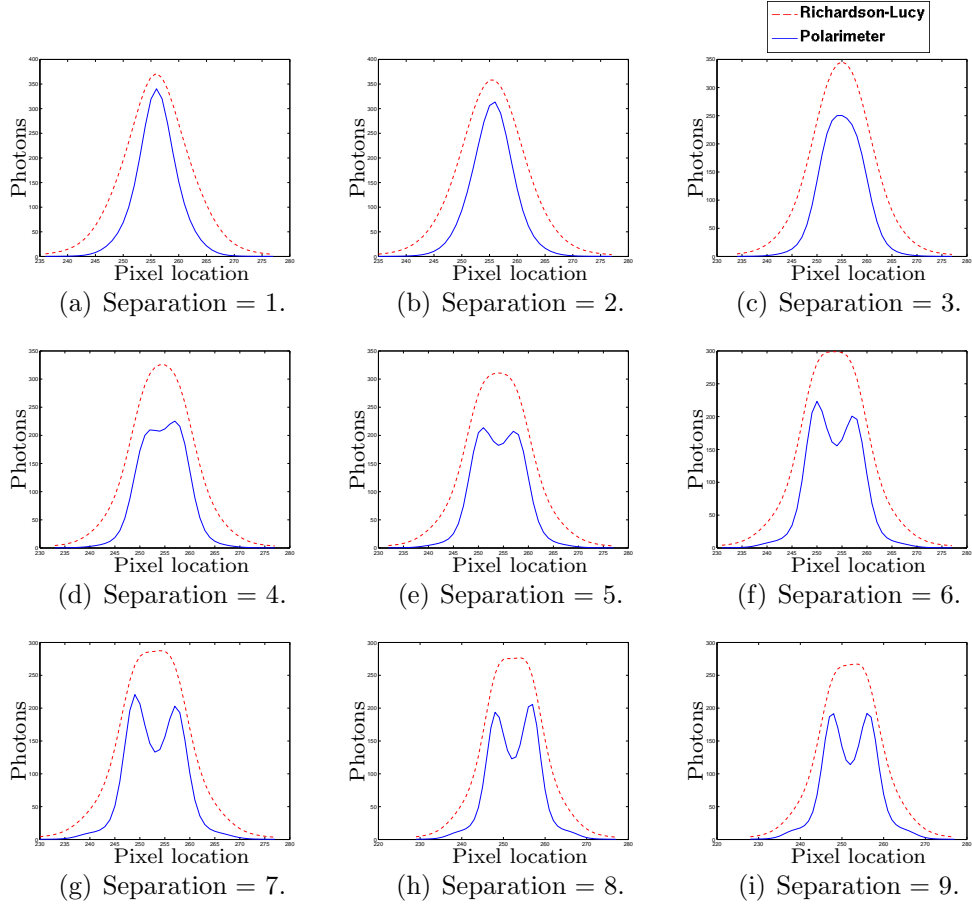


Figure 6.7: Cross-sectional views of deconvolved objects at an SNR of 0.65.

6.1.2 Known psf with laboratory data. Using laboratory images produced from the setup described in Section 4.3, both algorithms are allowed to iterate until the termination criteria is reached. The termination criteria is determined by the amount of noise in the images. Once the mean square error between iterations reaches the noise level present in the images the algorithm terminates. Both algorithms are able to deconvolve the object of interest when provided the estimate of the defocus aberration. The estimates of the actual defocus aberration used to produce the results are generated by the FAD algorithm of Section 4.2. Based on the results and the previous discussion of the bounds in the previous section this indicates that the lighting is sufficient for both algorithms to have similar performance at the lower aberrations. As the defocus aberration is increased, the polarimeter performance increases corre-

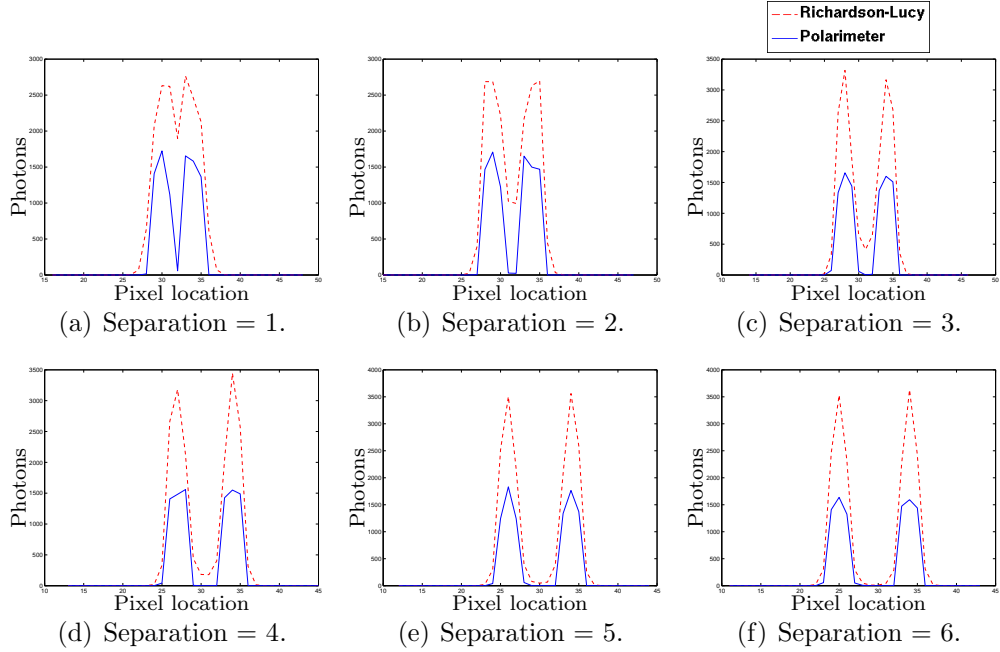


Figure 6.8: Cross-sectional views of deconvolved objects at an SNR of 6.

spondingly over the RL algorithm. For the laboratory images, the difference between the two algorithms is seen in the differences between the peaks and valleys of the object estimates.

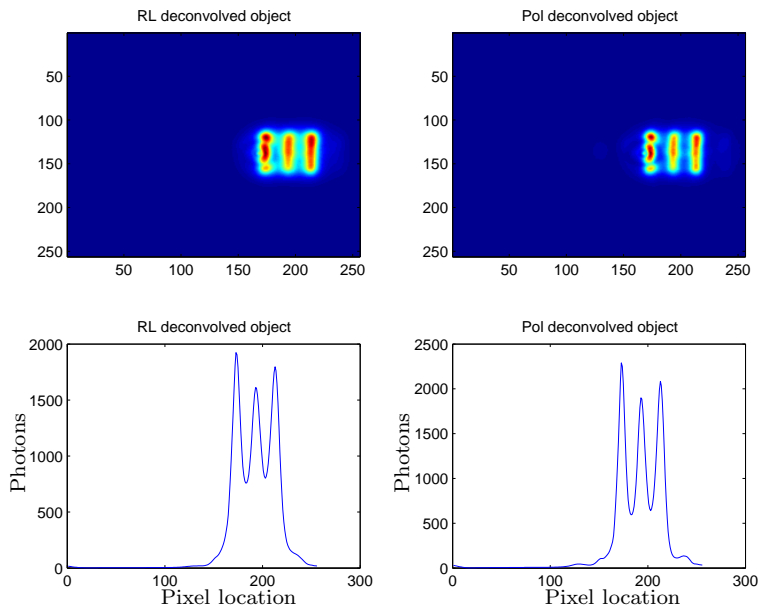


Figure 6.9: Deconvolution - Position 1.

In Figure 6.9 the RL algorithm's first valley is 39% of the first peak and the resulting area between the bars in the deconvolved object is brighter. The bars are less distinguishable. The polarimeter algorithm's first valley is 24% of the first peak and results in a much darker area between the bars making them easier to distinguish their extent.

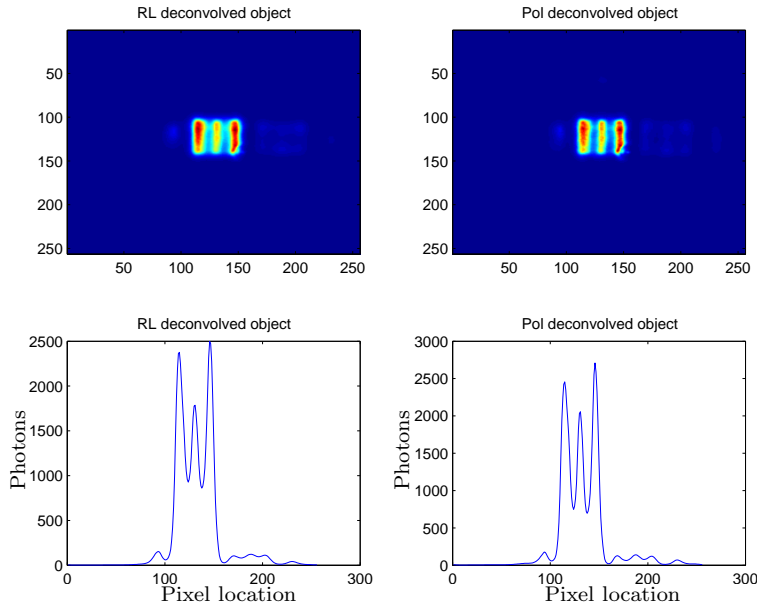


Figure 6.10: Deconvolution - Position 5.

In Figure 6.10 the RL algorithm's first valley is 38% of the first peak and the polarimeter algorithm's first valley is 30% of the first peak.

The target is nearly in focus in Figure 6.11 at Position 7 and both algorithms have very similar performance. This is consistent with the lower aberration and ample lighting. The laboratory results confirm the fidelity predictions of the simulation results of Section 6.1. The lower defocus aberration results of both algorithms would be scored nearly the same but the polarimeter algorithm would receive a better score as the defocus aberration is increased. The difference between the two algorithms is more significant when considering the results of their use in the multiframe algorithms in the following sections.

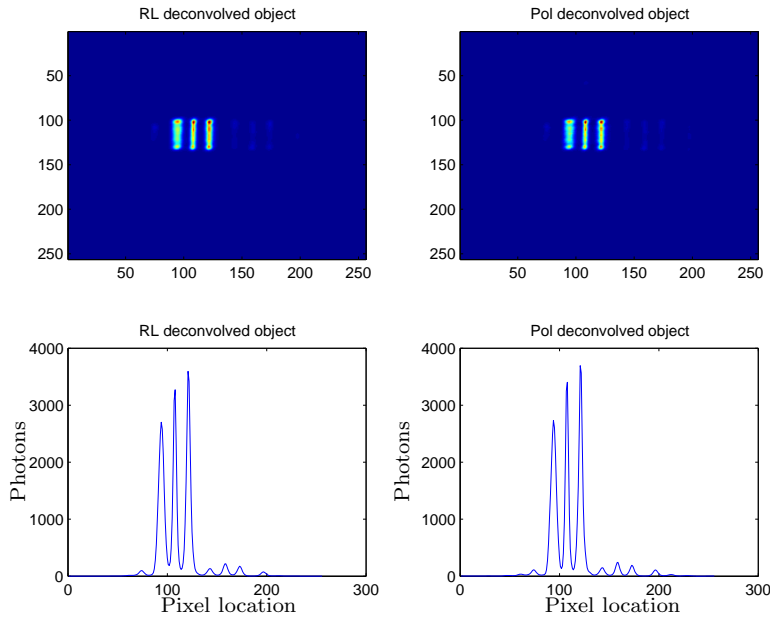
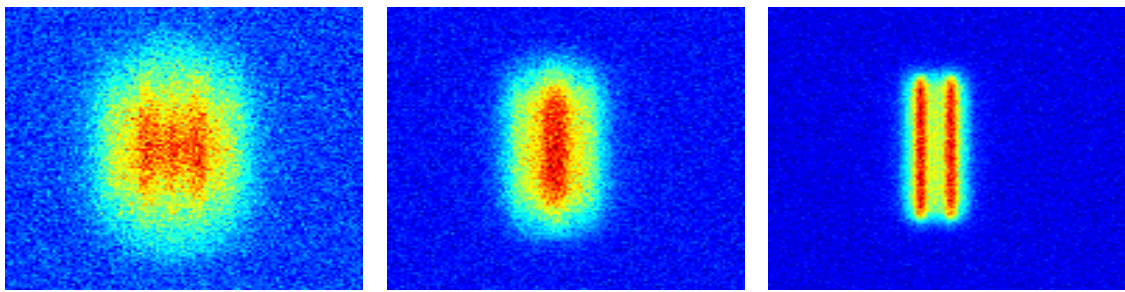


Figure 6.11: Deconvolution - Position 7.

6.2 Polarimeter Multiframe Blind Deconvolution

This section presents the results of the extension of both the RL algorithm to the MFBD algorithm and the polarimeter algorithm to the PMFBD algorithm. The simulation uses three separate primary channel images, Figure 6.12, for testing the MFBD algorithm. The six corresponding polarimeter images, 3 primary channels and 3 polarization sensitive, are shown in Figure 6.13.



(a) Image 1.

(b) Image 2.

(c) Image 3.

Figure 6.12: Images used for MFBD algorithm testing.

The three channels vary by different amounts of defocus aberration. Since the images are simulated there is no need to register the independent images resulting

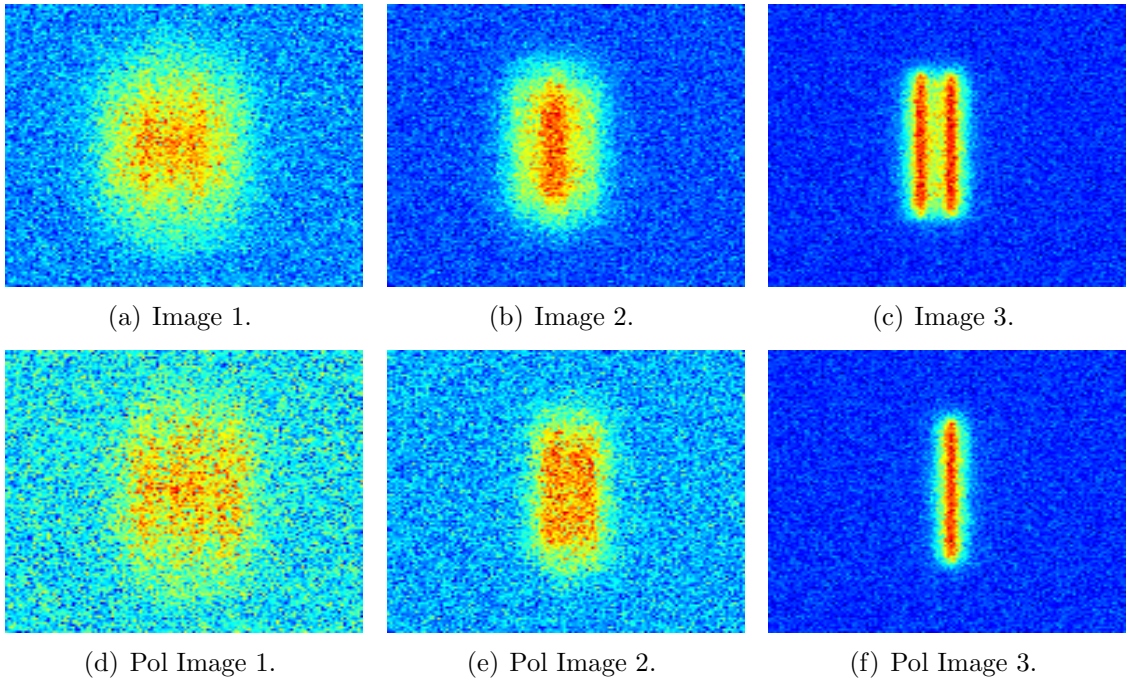


Figure 6.13: Images used for PMFBD algorithm testing.

in zero registration error. Image 1 has an aberration of 150 times the atmospheric defocus covariance with a $D/R_o = 1$. Image 2 has an aberration of 90 times the atmospheric defocus covariance with a $D/R_o = 1$. Image 3 has an aberration of 40 times the atmospheric defocus covariance with a $D/R_o = 1$. The MFBD images have twice the SNR as the primary images for the PMFBD simulation to account for the theoretical beamsplitter. This is visible in the different amounts of noise visible in the images.

The initial guess for both algorithms is a diffraction limited OTF for all three objects. Both algorithms then follow a similar breakdown in the internal iteration. First they estimate the new objects from the old objects using the old estimates of the psfs. Then they update the three psfs estimates using the old object estimates.

In order to compare performance all internal loops are limited to a fixed number of iterations. For instance, each object estimate update is limited to 20 iterations. The psf updates are limited to 5 iterations each. The outside loop is allowed to converge to a fixed mean square error between executions of the outside loop. This

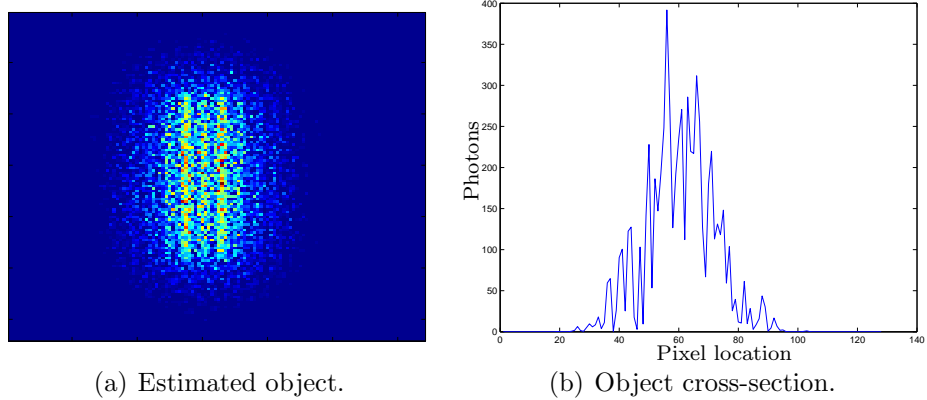


Figure 6.14: MFBD estimated object.

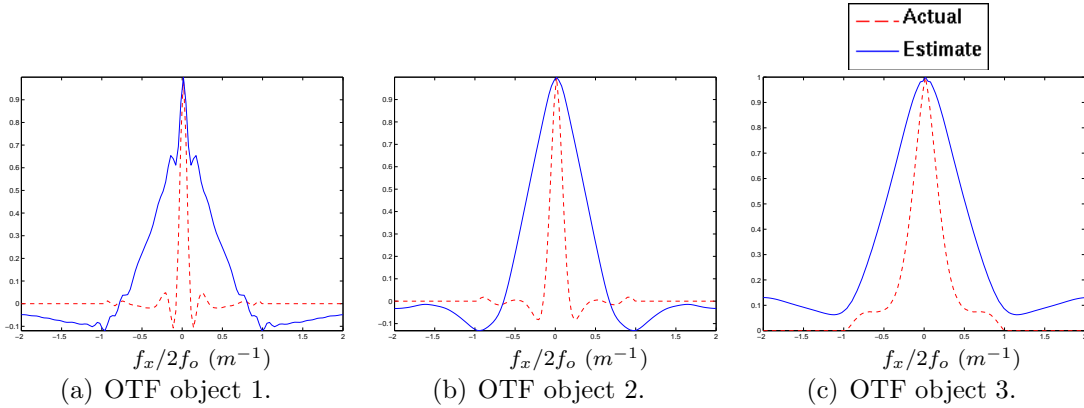


Figure 6.15: MFBD estimated OTFs.

predetermined value is based on the noise level of the images. For the simulations, the standard deviation of the noise is approximately 0.6. Using this value, the mean square error (MSE) between outside loops is allowed to converge to a value of 0.7. The overall effect is that the MFBD and PMFBD algorithms progress in lock step based on number of object and psf updates. The MFBD algorithm usually requires a significantly higher number of outer-loop iterations to converge to the same MSE error between outer loops.

The MFBD results are shown in Figures 6.14 and 6.15. Even with a target bar separation of 8 pixels the MFBD algorithm has a hard time deconvolving the two bars. There is a visible valley between the two sides of the object. The three psf estimates are Fourier transformed into their OTFs in order to visually compare them

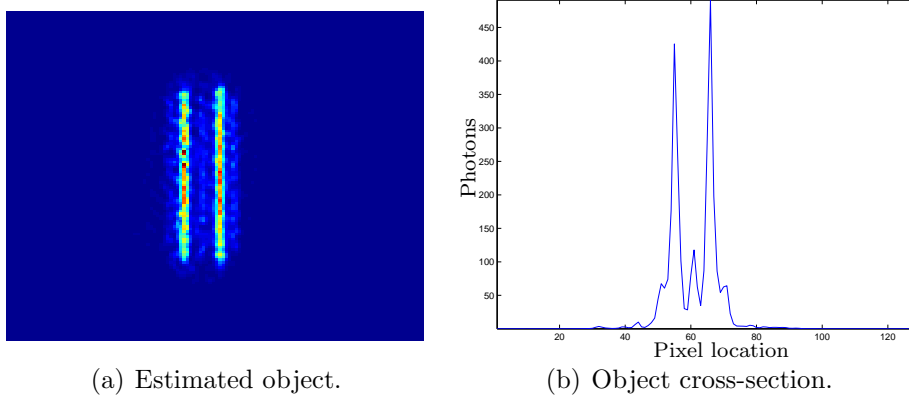


Figure 6.16: PMFBD estimated object.

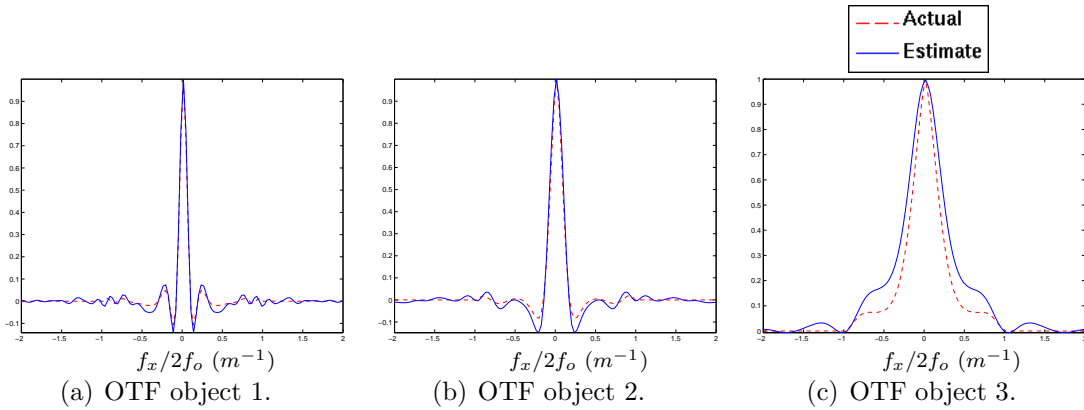


Figure 6.17: PMFBD estimated OTFs.

to the actual OTFs used to create the images. The results seen in Figure 6.15 show that the MFBD algorithm is able to estimate OTFs that are closer to the actual OTFs than the original guess at the start of the algorithm. However, the error between the estimates and the actual OTFs is still significant when the algorithm reaches the MSE termination criteria.

The results of the PMFBD are shown in Figures 6.16 and 6.17. The simulated bar target is clearly visible in Figure 6.16(a). The cross section visible in Figure 6.16(b) shows a clear separation in the bars. These results are a clear improvement over the MFBD algorithm with the same input images even with the lower light levels present the polarimeter images. The significant improvement is due to the much better estimation of the psfs. Looking at the estimated OTFs in Figure 6.17, there is a very

close match between the estimated OTF and the actual OTF. The polarization data allows a much better estimate of the psf to be made.

6.2.1 Convergence Rates. With both algorithms allowed a fixed number of internal iterations per outer loop, the convergence to the same MSE termination condition is presented. The results for the previous section's same three images are presented in Figure 6.18. The algorithms are run consecutively for bar separations from 1 to 8 pixels. The same bar width of 3 pixels is used. The PMFBD algorithm converges to a much better solution based on the fidelity metric within half the outer loop iterations of the MFBD algorithm. The MFBD algorithm fails to make significant improvements in object estimation by the time the termination criteria is reached.

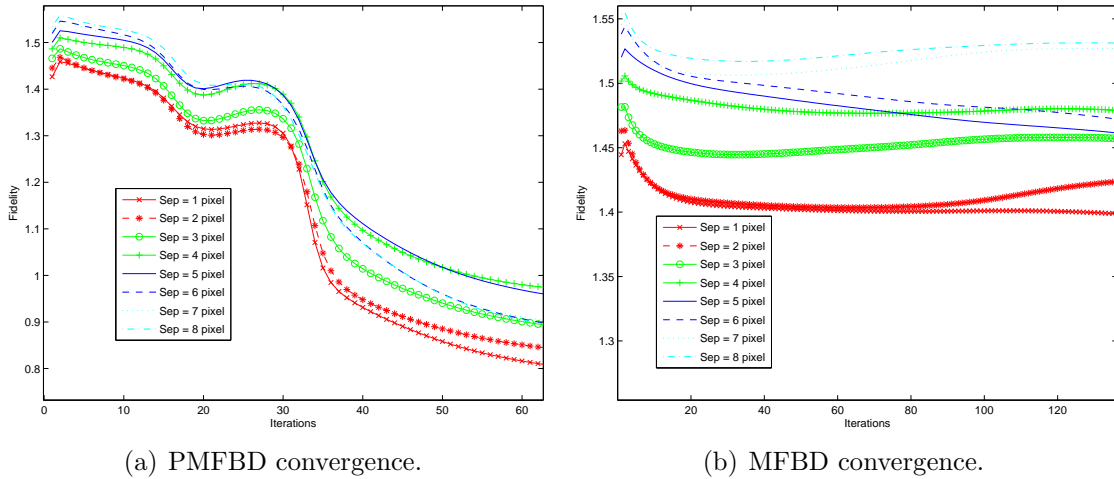


Figure 6.18: Algorithm fidelity versus iterations.

6.2.2 Laboratory Results. The three laboratory images at Position 3, Position 4, and Position 5 are given to both the MFBD and the PMFBD algorithms. The resulting estimate of the object is shown in Figure 6.19. The significant difference in object estimation between the two algorithms is in the peaks and valleys of the object estimated. The MFBD object valleys are approximately 30% of the peak values. The PMFBD valleys almost go to zero given the same images. The valleys are approximately 1/13th of the peak values. The actual peak values are very similar.

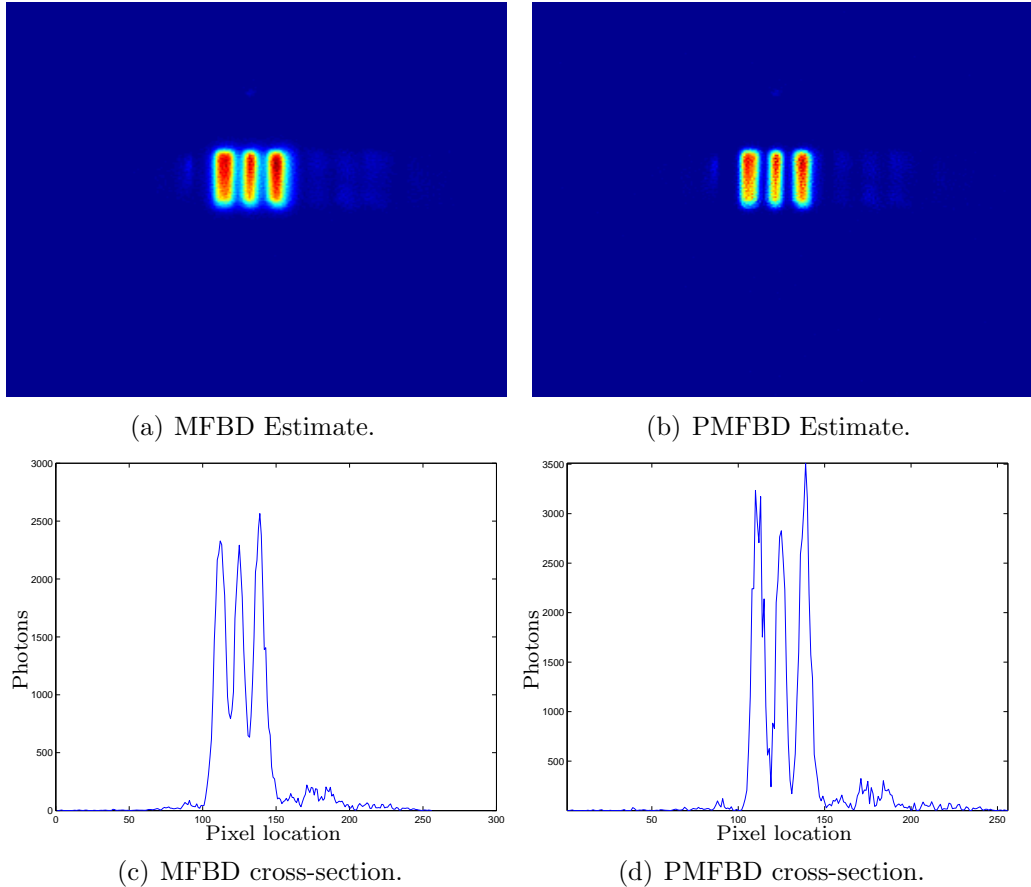


Figure 6.19: Laboratory multiframe estimated objects and cross-sections.

The most significant difference between the two algorithms is in the ability to estimate the actual OTFs. The results of the OTF estimates are shown in Figure 6.20. The top set of estimates is produced by the MFBD algorithm and the bottom set is produced by the PMFBD algorithm. The actual OTF used for comparison is the OTF estimated by the FAD algorithm for the laboratory images. With similar results to simulation, the MFBD algorithm fails to significantly improve the estimates of the OTFs for the three objects. The PMFBD algorithm clearly improves the estimation of the OTFs for the three objects.

The results in this chapter show that polarization data, when available, improves the ability to deconvolve objects using the algorithms developed for polarimeter deconvolution and polarimeter blind deconvolution.

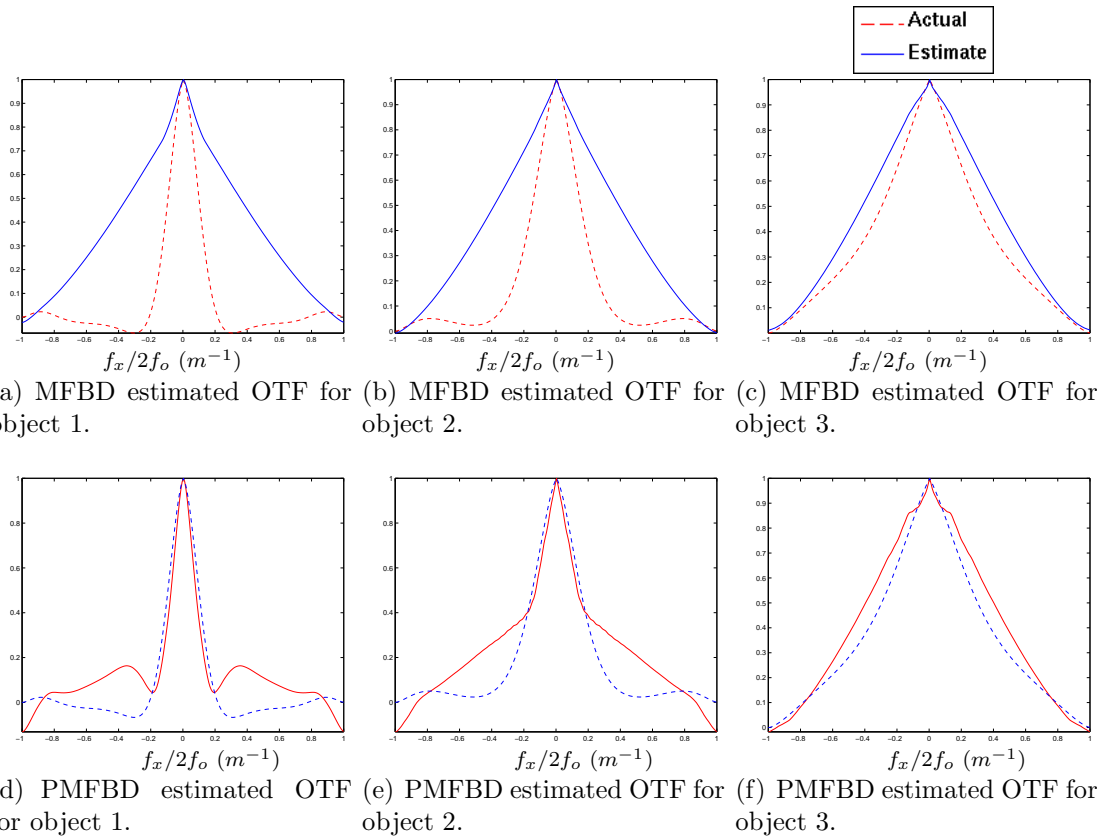


Figure 6.20: Laboratory multiframe estimated OTFs.

VII. Conclusions

The previous chapters detail the objectives of this research and their successful achievement. The first objective achieved is detailed in Chapter III which shows the development of the spatial resolution CRLB for a two-channel polarimeter incorporating atmospheric effects. The second objective is achieved with the production of calibrated data detailed in Chapter IV. The calibrated data is used for testing of the algorithms developed in Chapter V for the third objective.

The spatial resolution CRLB for a two-channel polarimeter show improved spatial resolution under certain lighting conditions. With sufficient light both systems have the same performance. However, below a certain point as the light levels decrease, the polarimeter's spatial resolution improves over standard imaging as the degree of polarization of the object increases. The limit in spatial resolution achieved by either imaging system is determined by the light level. The conditions in which the polarimeter outperforms standard imaging is shown in the comparison of the CRLBs for both systems. Thus the first objective is achieved.

The second objective is achieved by producing a set of calibrated data for testing purposes. An optics bench is set up to provide an initial set of real images with controlled focus errors. The FAD algorithm, presented in Section 4.2, is a new approach for detection of focus error using a single image. This is an improvement over historical methods that require complicated calibrations or the diversion of light from the primary imaging channel. The ability to detect algorithmically the actual focus error in an image allows for more accurate test images from the laboratory setup. This reduces the error in location of the actual focal point of the laboratory setup that would otherwise result from the use of real (non-thin) lenses, a compound lens, and locations of other components. The laboratory images were used to develop Matlab[®] images with similar statistics but with a broader range of lighting conditions. Both the laboratory images and the simulated images were useful in testing the algorithms developed.

The third objective is achieved with the successful development of the algorithms in Chapter V that make use of the polarization information. Initially, an algorithm is developed for polarimeter deconvolution with a known aberration. The incorporation of the polarization information yields an improvement in deconvolution. One can see from the cross-sectional views of Figure 6.6 and 6.7 that the improved resolution based on the bound calculations of Chapter III is realized. At a SNR of 0.71, Figure 6.6 shows that the polarimeter can resolve the two bars at a minimum separation of two pixels while the standard imaging system resolves the bars with a minimum of four pixels. Thus the polarimeter achieves half the spatial resolution compared to the standard imaging system. Figure 6.7 shows that a further reduction in the number of photons results in the failure of the RL algorithm to resolve the bars but the polarimeter algorithm resolves the bars at a separation of four pixels. As the pixel separation and/or lighting increases, the ability to resolve the two bars becomes nearly identical. These results conform to the CRLB comparisons between the two systems.

An additional benefit of the polarimeter deconvolution is seen in the fidelity metric results shown in Figures 6.2, 6.3, and 6.4. The polarimeter deconvolution consistently has a higher deconvolved object fidelity than the RL algorithm when they are operating on the same images. The reason for this is the polarimeter deconvolution's ability to estimate bars with steeper sides and lower valleys when compared to the RL algorithm results.

The polarization deconvolution algorithm is then extended under the assumption of an unknown aberration. Leveraging the results of Schulz' MFBD algorithm results in the PMFBD algorithm. The PMFBD algorithm is a GEM algorithm that alternates between estimation of the object and estimation of the *psf*. The PMFBD algorithm achieves significant improvement in the rate of convergence over the RL based MFBD algorithm, Section 6.2.1. The most significant improvement over the MFBD algorithm is in the estimation of the OTFs. The OTFs estimated by the PMFBD algorithm, Figure 6.17, are very close to the OTFs used to create the test

images. However, the OTFs estimated by the MFBD algorithm are significantly different, as in Figure 6.15. The addition of the polarization information in the PMFBD algorithm produces superior results.

All of these results put together show that the use of polarization data in electro-optical imaging systems improves the ability to deconvolve objects of interest. This research goal is clearly achieved.

Recommended Research

Recommended follow-ons to this research are:

- To extend the polarimeter deconvolution algorithms with additional channels.
With only two channels currently used, one cannot distinguish between unpolarized light and light polarized at 45 degrees with respect to the polarized channel. Additional polarimeter channels would allow estimation of the degree of polarization present in the scene.
- To implement the FAD algorithm using a Weiner filter to deconvolve the object instead of the RL algorithm, as discussed in Section 4.4.3.

Bibliography

1. Ayers, G. R. and J. C. Dainty. “Iterative blind deconvolution method and its applications”. *Optics Letters*, 13(7):547–549, July 1988.
2. Bäck, Thomas, David B. Fogel, and Zbigniew Michalewicz. *Evolutionary Computation 1, Basic Algorithms and Operators*. Institute of Physics Publishing, The Public Ledger Building, Suite 1035, 150 South Independence Mall West, Philadelphia, PA 19106, 2000.
3. Bharmal, Nazim A. “Static optical designs for Wavefront Curvature Sensing”. *Journal of Instrumentation*, 1(06):P06003, 2006. URL <http://stacks.iop.org/1748-0221/1/P06003>.
4. ten Brummelaar, T. A. “Modeling atmospheric wave aberrations and astronomical instrumentation using the polynomials of Zernike”. *Optics Communication*, 132:329–342, 1996.
5. Cain, Stephen. “Bayesian-Based Subpixel Brightness Temperature Estimation From Multichannel Infrared GOES Radiometer Data”. *IEEE Trans. on Geoscience and Remote Sensing*, 42(1):188–201, January 2004.
6. Combettes, P. “Generalized convex set theoretic image recovery”, 1996. URL citeseer.csail.mit.edu/combettes96generalized.html.
7. Cooper, George R. and Clare D. McGillem. *Continuous & Discrete Signal & Systems Analysis*. Saunders College Publishing, third edition, 1991.
8. Fienup, J. R. “Phase Retrieval Algorithms: A Comparison”. *Applied Optics*, 21(15):2758–2769, 1982.
9. Fiete, Robert D. and Theodore Tantalo. “Comparison of SNR image quality metrics for remote sensing systems”. *Optical Engineering*, 40(4):574–585, April 2001.
10. Fish, D. A., A. M. Brinicombe, and E. R. Pike. “Blind deconvolution by means of the Richardson-Lucy algorithm”. *Journal of the Optical Society of America A*, 12(1):58–65, January 1995.
11. Gamiz, Victor L. and John F. Belsher. “Performance limitations of a four-channel polarimeter in the presence of detection noise”. Dennis H. Goldstein and David B. Chenault (editors), *Polarization: Measurement, Analysis, and Remote Sensing II*, volume 3754, 204–216. SPIE, 1999.
12. Gamiz, Victor L. and John F. Belsher. “Performance limitations of a four-channel polarimeter in the presence of detection noise”. *Optical Engineering*, 41(5):973–980, May 2002.

13. Gerchberg, R. W. and W. O. Saxton. “A Practical Algorithm for the Determination of Phase from Image and Diffraction Plane Pictures”. *OPTIK*, 35(2):237–246, 1972.
14. Goodman, Joseph W. *Statistical Optics*. A Wiley Interscience Publication. John Wiley & Sons, Inc., 605 Third Avenue, New York, NY 10158-0012, 2000.
15. Goodman, Joseph W. *Introduction to Fourier Optics*. Roberts & Company Publishers, 4950 S. Yosemite Street, F2 #197, Greenwood Village, CO 80111, 2005.
16. Hecht, Eugene. *Optics*. Addison Wesley, 1301 Sansome St., San Francisco, CA 94111, fourth edition, 2002.
17. Hickson, Paul. “Wave-front curvature sensing from a single defocused image”. *Journal of the Optical Society of America A*, 11(5):1667–1673, May 1994.
18. Holmes, Timothy J. “Blind deconvolution of quantum-limited incoherent imagery: maximum-likelihood approach”. *Journal of the Optical Society of America A*, 9(7):1052–1061, July 1992.
19. Ingleby, H. R. and D. R. McGaughey. “Parallel Multiframe Blind Deconvolution Using Wavelength Diversity”. *Image Reconstruction from Incomplete Data III*, volume 5562, 58–64. SPIE, October 2004.
20. Ivanov, V. Yu., V. P. Sivokon, and M. A. Vorontsov. “Phase retrieval from a set of intensity measurements: theory and experiment”. *Journal of the Optical Society of America A*, 9(9):1515–1524, September 1992.
21. Jefferies, Stuart M., Kathy J. Schulze, and Charles L. Matson. “Blind Deconvolution with the use of a Phase Constraint”. *Proceedings of the 2002 AMOS Conference*. September 2002.
22. Kattnig, Alain Philippe, Ouamar Ferhani, and Jérôme Primot. “Mission-driven evaluation of imaging system quality”. *Journal of the Optical Society of America A*, 18(12):3007–3017, December 2001.
23. Klotz, Frank G. “Space as an Essential Tier in National Security”. Speech given to Fisher Brothers Institute for Air and Space, Strategic Studies, Tel Aviv, Israel, 2006.
24. Likas, Aristidis C. and Nikolas P. Galatsanos. “A Variational Approach for Bayesian Blind Image Deconvolution”. *IEEE Trans. on Signal Processing*, 52(8):2222–2233, August 2004.
25. Lucy, L. B. “An iterative technique for the rectification of observed distributions”. *The Astronomical Journal*, 79(6):745–754, June 1974.
26. Mandel, Leonard and Emil Wolf. *Optical Coherence and Quantum Optics*. Cambridge University Press, 40 West 20th Street, New York, NY 10011-4211, 1995.
27. Michalewicz, Zbigniew and David B. Fogel. *How to Solve it: Modern Heuristics*. Springer-Verlag, Berlin, Heidelberg, 2000.

28. Paxman, Richard G., Timothy J. Schulz, and James R. Fienup. “Joint estimation of object and aberrations by using phase diversity”. *Journal of the Optical Society of America A*, 9(7):1072–1085, July 1992.
29. Platt, Ben C. and Roland Shack. “History and Principles of Shack-Hartmann Wavefront Sensing”. *Journal of Refractive Surgery*, 17:S573–S577, September/October 2001.
30. Richardson, William H. “Bayesian-Based Iterative Method of Image Restoration”. *Journal of the Optical Society of America*, 62(1):55–59, January 1972.
31. Roddier, F. “Curvature Sensing: a new concept in adaptive optics”. *Applied Optics*, 27:1223–1225, 1988.
32. Roddier, Francois, Claude Roddier, and Nicolas Roddier. “Curvature sensing: a new wavefront sensing method”. *Statistical Optics*, volume 976 of *Proceedings*, 203–209. SPIE, August 1988.
33. Roggemann, M. C. and B. M. Welsh. *Imaging Through Turbulence*. CRC Press, Boca Raton, FL, 1996.
34. Schmalz, Mark S. “Genetic Algorithms for Single- and Multi-frame Blind Deconvolution”. *Proceedings of the 2004 AMOS Conference*. September 2005.
35. Schmalz, Mark S. “Genetic Algorithms for Single- and Multi-frame Blind Deconvolution”. *Proceedings of the 2005 AMOS Conference*. September 2005.
36. Schulz, Timothy J. “Multiframe Blind Deconvolution of Astronomical Images”. *Journal of the Optical Society of America*, 10(5):1064–1073, May 1993.
37. Schulz, Timothy J., Wei Sun, and Michael C. Roggemann. “Cramer-Rao bounds for estimation of turbulence-induced wavefront aberrations”. Michael C. Roggemann and Luc R. Bissonette (editors), *Propagation and Imaging through the Atmosphere III*, volume 3763, 23–28. SPIE, 1999.
38. Schulze, Kathy J. “A Comparison of Parallelization Techniques for Bispectrum and Blind Deconvolution”. *Proceedings of the 2002 AMOS Conference*. September 2003.
39. Seldin, J. H. and J. R. Fienup. “Iterative Blind Deconvolution Algorithm Applied to Phase Retrieval”. *Journal of the Optical Society of America A*, 7(3):428–433, March 1990.
40. Shepp, L. A. and Y. Vardi. “Maximum likelihood reconstruction for image tomography”. *IEEE Trans. Med. Imaging*, 1(2):113–122, 1982.
41. Sokolov, A. V. *Optical Properties of Metals*. American Elsevier Publishing Company, Inc., 52 Vanderbilt Avenue, New York, NY 10017, english edition, 1967.
42. Strong, David. “Atmospheric Effects on Spatial Frequency Bounds on Polarimeter Imaging”. *2006 AMOS Conference Proceedings*. September 2006.

43. Strong, David and Stephen Cain. "Spatial Frequency Bounds of a Polarimetric Sensor". *Proceedings of the 2005 AMOS Technical Conference*. September 2005.
44. Tirpak, John A. "Space and Counterspace". *Air Force Magazine*, 89(6), June 2006.
45. VanTrees, Harry L. *Detection, Estimation, and Modulation Theory: Part I*. A Wiley Interscience Publication. John Wiley & Sons, Inc., 605 Third Avenue, New York, NY 10158-0012, 2001.

REPORT DOCUMENTATION PAGE

*Form Approved
OMB No. 0704-0188*

The public reporting burden for this collection of information is estimated to average 1 hour per response, including the time for reviewing instructions, searching existing data sources, gathering and maintaining the data needed, and completing and reviewing the collection of information. Send comments regarding this burden estimate or any other aspect of this collection of information, including suggestions for reducing this burden to Department of Defense, Washington Headquarters Services, Directorate for Information Operations and Reports (0704-0188), 1215 Jefferson Davis Highway, Suite 1204, Arlington, VA 22202-4302. Respondents should be aware that notwithstanding any other provision of law, no person shall be subject to any penalty for failing to comply with a collection of information if it does not display a currently valid OMB control number. PLEASE DO NOT RETURN YOUR FORM TO THE ABOVE ADDRESS.ZZZZZZZZZZ

| | | |
|---|------------------|------------------------------|
| 1. REPORT DATE (DD-MM-YYYY) | 2. REPORT TYPE | 3. DATES COVERED (From — To) |
| 13-09-2007 | PhD Dissertation | Sept 2004 — Sept 2007 |
| 4. TITLE AND SUBTITLE | | 5a. CONTRACT NUMBER |
| Polarimeter Blind Deconvolution Using Image Diversity | | 5b. GRANT NUMBER |
| | | 5c. PROGRAM ELEMENT NUMBER |
| | | 5d. PROJECT NUMBER |
| | | 5e. TASK NUMBER |
| | | 5f. WORK UNIT NUMBER |
| 7. PERFORMING ORGANIZATION NAME(S) AND ADDRESS(ES) | | |
| Air Force Institute of Technology Graduate School of Engineering and Management (AFIT/EN) 2950 Hobson Way WPAFB OH 45433-7765 | | |
| 8. PERFORMING ORGANIZATION REPORT NUMBER | | |
| AFIT/GE/ENG/07-20 | | |
| 9. SPONSORING / MONITORING AGENCY NAME(S) AND ADDRESS(ES) | | |
| AFRL-DESA Attn: Dr Victor Gamiz 3550 Aberdeen Ave SE, Bldg 422 Kirtland Air Force Base, NM 87117-5776 DSN: 246-4846 e-mail: Victor.Gamiz@kirtland.af.mil | | |
| 10. SPONSOR/MONITOR'S ACRONYM(S) | | |
| 11. SPONSOR/MONITOR'S REPORT NUMBER(S) | | |
| 12. DISTRIBUTION / AVAILABILITY STATEMENT | | |
| Approval for public release; distribution is unlimited. | | |
| 13. SUPPLEMENTARY NOTES | | |
| 14. ABSTRACT | | |
| This research presents an algorithm that improves the ability to view objects using an electro-optical imaging system with at least one polarization sensitive channel in addition to the primary channel. An innovative algorithm for detection and estimation of the defocus aberration present in an image is also developed. Using a known defocus aberration, an iterative polarimeter deconvolution algorithm is developed using a generalized expectation-maximization (GEM) model. The polarimeter deconvolution algorithm is extended to an iterative polarimeter multiframe blind deconvolution (PMFBD) algorithm with an unknown aberration. Using both simulated and laboratory images, the results of the new PMFBD algorithm clearly outperforms an RL-based MFBD algorithm. The convergence rate is significantly faster with better fidelity of reproduction of the targets. Clearly, leveraging polarization data in electro-optical imaging systems has the potential to significantly improve the ability to resolve objects and, thus, improve Space Situation Awareness. | | |
| 15. SUBJECT TERMS | | |
| polarimeter, blind deconvolution, focus aberration detection, metrology | | |
| 16. SECURITY CLASSIFICATION OF: | | 17. LIMITATION OF ABSTRACT |
| a. REPORT | b. ABSTRACT | c. THIS PAGE |
| U | U | U |
| UU | UU | 135 |
| 18. NUMBER OF PAGES | | |
| 19a. NAME OF RESPONSIBLE PERSON Dr Stephen Cain | | |
| 19b. TELEPHONE NUMBER (include area code) (937) 255-3636, ext 4716 Stephen.Cain@afit.edu | | |